Attitude Estimation and Control of a Magnetically Actuated Earth-Observing Cubesat

Corey Miles

Department of Mechanical Engineering

McGill University, Montreal

August, 2021

A thesis submitted to McGill University in partial fulfillment of the requirements of the degree of

Master of Engineering

©Corey Miles, 2021

Abstract

The Meteorix mission is a nanosatellite demonstration mission dedicated to the observation and characterization of meteors and space debris entering into the Earth's atmosphere. The scientific objectives of this mission require a high performance attitude determination and control system (ADCS). This thesis entails the development of attitude estimation and control algorithms for the Meteorix 3U cubesat. Attitude estimation and control requirements are outlined, given the mission's scientific objectives and the power needs of the satellite. A magnetometer-only multiplicative extended Kalman filter (MEKF) is formulated to estimate the satellite's attitude and angular velocity. It is compared to a conventional gyro-based MEKF and uses the derivative of the magnetic field and the attitude dynamics model, in place of gyroscope measurements to update the angular velocity estimate. Results from Monte Carlo simulations show that the magnetometer-only MEKF outperforms a gyro-based MEKF in low angular velocity scenarios. A sliding mode controller is developed for attitude control using three magnetic actuators, while a single flywheel oriented in a momentum bias configuration provides gyroscopic stability. Using the attitude and angular velocity feedback from the magnetometer-only MEKF, the sliding mode control law offers better pointing accuracy than a standard proportional derivative (PD) magnetic feedback controller; it is also shown to be more robust to uncertainties and disturbances in a sensitivity study. The magnetometer-only MEKF suffers in the presence of model uncertainties such as flywheel misalignment and residual magnetic moment, and methods to improve the overall ADCS performance are discussed.

Abrégé

La mission Meteorix est une mission de démonstration de nanosatellites dédiée à l'observation et à la caractérisation des météores et des débris spatiaux entrant dans l'atmosphère terrestre. Les objectifs scientifiques de cette mission nécessitent un système de détermination d'attitude et de contrôle (ADCS) de haute performance. Cette thèse porte sur le développement d'algorithmes d'estimation et de contrôle d'attitude pour le cubesat Meteorix 3U. Les exigences en matière d'estimation et de contrôle de l'attitude sont décrites, compte tenu des objectifs scientifiques de la mission et des besoins en énergie du satellite. Un filtre de Kalman étendu multiplicatif (MEKF) est formulé pour estimer l'attitude et la vitesse angulaire du satellite. Il est comparé à un MEKF conventionnel basé sur un gyroscope et utilise la dérivée du champ magnétique et le modèle de dynamique d'attitude, à la place des mesures du gyroscope pour mettre à jour l'estimation de la vitesse angulaire. Les résultats des simulations de Monte Carlo montrent que le MEKF à magnétomètre seul surpasse le MEKF à gyroscope dans les scénarios à faible vitesse angulaire. Un contrôleur à mode glissant est développé pour le contrôle d'attitude à l'aide de trois actionneurs magnétiques, tandis qu'un seul volant d'inertie orienté dans une configuration de biais de momentum assure la stabilité gyroscopique. En utilisant le retour d'information sur l'attitude et la vitesse angulaire du MEKF à magnétomètre seul, la loi de contrôle en mode glissant offre une meilleure précision de pointage qu'un contrôleur standard à retour d'information magnétique proportionnel et dérivé (PD) ; il est également démontré qu'il est plus robuste aux incertitudes et aux perturbations dans une étude de sensibilité. Le MEKF à magnétomètre seul souffre de la présence d'incertitudes de modèle telles que

le désalignement du volant d'inertie et le moment magnétique résiduel, et des méthodes pour améliorer la performance globale de l'ADCS sont discutées.

Acknowledgements

First, I would like to thank my supervisor Professor Inna Sharf for her support and guidance throughout my Master's degree. She always provided valuable feedback and kept me motivated throughout the process. I am especially thankful to her for funding my degree and for her patience and optimism in all of our meetings, given that the majority of my Master's degree was spent in lockdown due to the pandemic. I would also like to thank everyone in the Aerospace Mechatronics Lab for their help on certain topics such as Kalman filtering and quaternions, and for the occasional trips to Tim Hortons. I am deeply thankful to my family for their love and support throughout both of my degrees at McGill. I definitely couldn't have done it without them. Lastly, I would like to thank Lauren Manoukian for her unwavering support and for always making me laugh at the end of a long day of research.

Contents

	Abs	ract	i
	Abr	égé	ii
	Ack	nowledgements	iv
	List	of Figures	Х
	List	of Tables	xi
1	Intr	oduction	1
	1.1	Related Work	3
		1.1.1 Attitude Estimation	3
		1.1.2 Magnetic Attitude Control	6
	1.2	Thesis Objectives	9
	1.3	Thesis Outline	9
2	Met	eorix Mission	11
	2.1	The Mission	11
		2.1.1 Satellite Design	12
		2.1.2 Modes of Operation	13
	2.2	Power and Energy Analysis	14
	2.3	Attitude Control and Estimation Requirements	17
		2.3.1 Detumbling Mode	17
		2.3.2 Alignment Mode	18
		2.3.3 Nominal Mode	19

Contents vi

3	Met	eteorix Simulation Model	22
	3.1	Simulation Environment	 22
	3.2	Equations of Motion	 23
		3.2.1 Orbit Dynamics	 23
		3.2.2 Attitude Dynamics and Kinematics	 23
	3.3	Magnetic Field Model	 26
	3.4	Perturbations	 27
		3.4.1 Standard LEO perturbations	 27
		3.4.2 Residual Magnetic Moment	 29
4	Atti	titude Estimation	31
	4.1	Extended Kalman Filter	 31
	4.2	Multiplicative Extended Kalman Filter	 34
	4.3	Magnetometer-only MEKF	 40
	4.4	Implementation	 44
	4.5	Simulation Results	 46
		4.5.1 Tumbling Scenario	 49
		4.5.2 Earth-Pointing Scenario	 53
5	Atti	titude Control	55
	5.1	Setting the Desired Attitude	 56
	5.2	Proportional-Derivative Control	 57
	5.3	Sliding Mode Control	 59
	5.4	Simulations of Attitude Control	 63
		5.4.1 Detumbling Mode	 64
		5.4.2 Alignment Mode	 67
		5.4.3 Nominal Mode	 68
	5.5	Sensitivity Study	 74
		5.5.1 Large Initial Estimate Errors	 74

Contents

		5.5.2	Inertia Uncertainty	75
		5.5.3	Flywheel Axis Misalignment	78
		5.5.4	Residual Magnetic Moment	80
		5.5.5	All Uncertainties Combined	84
6	Con	clusior	ıs	88
	6.1	Summ	nary of Research	88
	6.2	Recon	nmendations for Future Work	90

List of Figures

2.1	Meteorix preliminary design	13
2.2	Desired orientation in alignment mode	19
2.3	Desired orientations in nominal mode	20
3.1	Tesselated surface geometry model of Meteorix in the body-fixed frame	28
4.1	Gyro-based MEKF estimation errors in tumbling scenario from $t=0$ to	
	t=30 minutes. (a) Total angular error, (b) Angular velocity error	51
4.2	Magnetometer-only MEKF estimation errors in tumbling scenario from $t=$	
	0 to $t=30$ minutes. (a) Total angular error, (b) Angular velocity error $. . . $.	52
4.3	Magnetometer-only MEKF estimation errors in Earth-pointing scenario from	
	$t=0\ { m to}\ t=30\ { m minutes}.$ (a) Total angular error, (b) Angular velocity error	54
5.1	Detumbling scenario 1 results. (a) Angular velocity, (b) Magnetic control	
	input	65
5.2	Detumbling scenario 2 results. (a) Angular velocity, (b) Magnetic control	
	input	66
5.3	Detumbling scenario 2 with $\Delta t = 0.1$ s. (a) Angular velocity, (b) Magnetic	
	control input	66
5.4	Angular velocity response after detumbling, $\Delta t = 0.1 \ \mathrm{s.} \ \ldots \ \ldots$	67
5.5	Alignment mode pointing angles. (a) y_b - n_o angle, (b) z_b - z_d angle	68
5.6	Alignment mode results. (a) Angular velocity, (b) Magnetic control input.	68

List of Figures ix

5.7	Nominal mode pointing angles. (a) \mathbf{z}_b - \mathbf{z}_d angle (b) \mathbf{y}_b - \mathbf{n}_o angle	69
5.8	Nominal mode results. (a) Angular velocity, (b) Magnetic control input	70
5.9	Ideal scenario pointing angles. (a) \mathbf{z}_b - \mathbf{z}_d angle (b) \mathbf{y}_b - \mathbf{n}_o angle	72
5.10	Ideal scenario ngular velocity and control inputs, from $t=1\ \mathrm{t}$ to $t=5$	
	orbits. (a) Angular velocity, (b) Magnetic control input	72
5.11	Estimate errors in ideal scenario. (a) Total angular error, (b) Angular veloc-	
	ity errors	73
5.12	Estimate errors in ideal scenario from $t=1\ {\rm to}\ t=5$ orbits. (a) Total angular	
	error, (b) Angular velocity errors	73
5.13	Pointing angles with inertia uncertainty. (a) \mathbf{z}_b - \mathbf{z}_d angle (b) \mathbf{y}_b - \mathbf{n}_o angle	76
5.14	Angular velocity and control inputs with inertia uncertainty, from $t=1\ {\rm t}$	
	to $t=5$ orbits. (a) Angular velocity, (b) magnetic control inputs $\dots \dots$	76
5.15	Estimate errors with inertia uncertainty, from $t=1$ to $t=5$ orbits. (a) Total	
	angular error, (b) Angular velocity error	77
5.16	Pointing angles with flywheel misalignment. (a) \mathbf{z}_b - \mathbf{z}_d angle (b) \mathbf{y}_b - \mathbf{n}_o angle	79
5.17	Angular velocity and control inputs with flywheel misalignment, from $t=% \frac{d^{2}}{dt^{2}}$	
	1t to $t=5$ orbits. (a) Angular velocity, (b) magnetic control inputs	80
5.18	Estimate errors with flywheel misalignment, from $t=1\ {\rm to}\ t=5$ orbits. (a)	
	Total angular error, (b) Angular velocity error	80
5.19	Pointing angles with residual magnetic moment. (a) \mathbf{z}_b - \mathbf{z}_d angle (b) \mathbf{y}_b - \mathbf{n}_o	
	angle	82
5.20	Angular velocity and control inputs with residual magnetic moment, from	
	t=1t to $t=5$ orbits. (a) Angular velocity, (b) magnetic control inputs $$	83
5.21	Estimate errors with residual magnetic moment, from $t=1\ {\rm t}$ to $t=5\ {\rm orbits}.$	
	(a) Total angular error, (b) Angular velocity errors	83
5.22	Pointing angles with PD control, ideal vs worst case scenario. (a) \mathbf{z}_b - \mathbf{z}_d	
	angle (b) \mathbf{y}_b - \mathbf{n}_o angle	86

List of Figures x

5.23	Estimate errors with PD control, ideal vs worst case scenario. (a) Total	
	angular error, (b) Angular velocity errors	86
5.24	Pointing angles with sliding mode control, ideal vs worst case scenario. (a)	
	\mathbf{z}_b - \mathbf{z}_d angle (b) \mathbf{y}_b - \mathbf{n}_o angle	87
5.25	Estimate errors with sliding mode control, ideal vs worst case scenario. (a)	
	Total angular error, (b) Angular velocity errors	87

List of Tables

2.1	Power consumption of Meteorix subsystems during Earth-pointing and	
	Sun-pointing	15
2.2	Attitude control and estimation requirements of the Meteorix mission	21
3.1	Perturbation models	29
4.1	The EKF algorithm	34
4.2	Estimator summary	45
4.3	Sensor noise parameters	46
4.4	Estimator parameters	47
4.5	Initial angular velocity scenarios	48
4.6	Attitude estimate errors in the tumbling scenario	50
4.7	Angular velocity estimate errors in the tumbling scenario	50
4.8	Gyroscope bias error of the gyro-based MEKF in the tumbling scenario	51
4.9	Attitude and angular velocity estimate errors of the magnetometer-only	
	MEKF in the Earth-pointing scenario	53
5.1	Attitude control parameters	64
5.2	Initial conditions for detumbling	65
5.3	Initial conditions for sensitivity study	74
5.4	Sources of error in worst case senario	85
5.5	Averaged ADCS performance results of 1 day simulations	85

Chapter 1

Introduction

Nanosatellites, weighing between 1 and 10 kg, have become increasingly popular in recent years due to the development of the standardized cubesat format [1]. Meteorix is a cubesat mission in development by the Centre Spatial Universitaire, CurieSat, at Sorbonne University [2]. It is designed for the detection of meteors and space debris entering Earth's atmosphere and its primary scientific objective is to estimate the flux density of these objects autonomously, using a camera and an on-board image processing chain.

Estimating the flux density of extraterrestrial material arriving at Earth is a widely studied problem [3]. Two recent projects have been developed with the purpose to detect meteors from space: the S-CUBE cubesat mission and the METEOR experiment aboard the International Space Station (ISS) [4], [5]. The METEOR experiment focused on determining the chemical composition of meteors and demonstrated the feasibility to observe meteors from space. There are also many ground-based facilities dedicated to detecting meteors from Earth, such as large camera networks in Canada, Australia, and Europe, and in particular the French Fireball Recovery and InterPlanetary Observation Network (FRIPON) [6]. The ability to make observations from space offers advantages over these ground-based systems such as no weather constraints, long recording time, and wide coverage [2]. Moreover, observations from Earth and space can be combined for stereo-

scopic measurements of meteors [7]. In fact, one of the main objectives of the Meteorix mission is to combine the data from Meteorix and FRIPON to form accurate stereoscopic measurements of meteor and space debris trajectories [7].

The success of the Meteorix mission depends on the reliability of the satellite's attitude determination and control system (ADCS). The aim of this thesis is to develop an ADCS for the Meteorix satellite that can enable the fulfillment of the scientific objectives of the mission. Specifically, accurate meteor localization and tracking from a satellite require accurate estimates of the satellite's attitude [7]. Active attitude control is needed to detumble the satellite after departure from the launch vehicle, align the satellite in a desired pointing direction, and perform re-orientation maneuvers throughout the mission. As such, three distinct mission modes are defined: detumbling mode, alignment mode, and nominal mode. Each mode has specific attitude control and estimation requirements that must be met. The camera and detection chain require high power consumption and place a heavy computational burden on the satellite's on-board computer [2]. For this reason, the Meteorix ADCS needs to use minimal sensors and actuators and be computationally efficient. The sensor and actuator configuration of the Meteorix cubesat is based upon the French EyeSat nanosatellite which was launched in 2019 [8]. EyeSat used a combination of star-trackers and magnetometers for attitude estimation, and magnetic actuators and reaction wheels for attitude control. However, due to the power consumption and computational constraints of the Meteorix mission, it was recommended that a single three-axis magnetometer should be used for attitude estimation, while attitude control should be done with three magnetic actuators. In addition, one flywheel oriented in a momentum bias configuration should provide gyroscopic stability. The Meteorix ADCS resarched in this thesis is therefore based on this unique sensor and actuator configuration.

1.1 Related Work

1.1.1 Attitude Estimation

Satellite attitude estimation can be done in many ways and has been studied since the 1960s. One of the earliest methods is an algebraic approach that calculates the attitude from a set of two vector observations, as for example, magnetometer measurements of Earth's magnetic field vector. This is a deterministic method known as the TRIAD algorithm [9]. In 1965, Wahba proposed the famous attitude determination problem which involves finding the optimal rotation matrix between two coordinate frames using a weighted set of any number of vector observations [10]. There are two notable early solutions to Wahba's problem. Davenport's q-method, reported in [11] solves for the unit quaternion parameterization of the attitude instead of the 9-element rotation matrix. However, this required performing an eigenvalue decomposition of a 4x4 matrix and was too computationally complex for the computers at the time [10]. The first algorithm suited to onboard computer processors was Shuster's Quaternion Estimator, known as the QUEST method [9]. QUEST was first applied in the MAGSAT mission in 1979 and is still widely used today [10]. These deterministic formulations do not explicitly account for the stochastic nature associated with random measurement noise and model uncertainty. As algorithm robustness and accuracy demands increased and computer processors became more capable, more complex algorithms emerged.

The extended Kalman filter (EKF) became the go-to method for satellite attitude estimation in the early 1980s [12]. In this work, we parameterize Meteorix's attitude with the unit quaternion. The quaternion is a four-parameter, singularity-free attitude representation and is subject to a unit norm constraint. This unit norm constraint presents some problems in the standard EKF implementation [12]. As a result, several variations of the EKF have been proposed to better handle quaternions. One of the most popular variations is known as the multiplicative EKF (MEKF) [13]. Instead of estimating the full quaternion,

the MEKF estimates a three parameter attitude error and then updates the full estimate with quaternion multiplication. The attitude kinematics must be propagated to predict the estimate at each time step. This propagation requires an estimate of the satellite's angular velocity which can be obtained in one of two ways. The first and most common way is to measure the angular velocity directly with a gyroscope and estimate the gyroscope bias to correct the measurement. The second is to estimate the angular velocity directly with the filter, in which case the attitude dynamics model is used to propagate the estimate. The traditional MEKF, referred to herein as the gyro-based MEKF, uses the former method and estimates the satellite attitude error and gyroscope bias error [14].

Most satellite attitude estimation techniques use vector measurements from any number of sensors including star trackers, Sun sensors, and magnetometers. However, we are more interested in single sensor attitude estimation methods as Meteorix is limited to one magnetometer. Luckily, the use of minimal sensors that provide sufficiently accurate attitude estimates has become a widely studied problem, particularly for small satellites [15]. One reason for this is that the noise characteristics of MEMS (micro-electromechanical systems) gyroscopes used in CubeSat applications are 10 - 100 times worse than modern fiber-optic gyroscopes used in larger satellites, and they are more sensitive to changes in temperature [16]. Precision pointing cubesats tend to use star trackers for both attitude and angular velocity estimation when high attitude control accuracy is required [16]. A comparison of gyroless and gyro-based attitude estimation using star tracker measurements is presented in [17]. It is shown that an MEKF using only star tracker measurements and the satellite attitude dynamics model performs as well or better than the gyro-based MEKF. A similar gyroless MEKF using only Sun vector measurements was developed for application to the O/OREOS 3U cubesat [18].

The magnetometer is a reliable sensor in the context of single sensor attitude estimation. A magnetometer measures the Earth's magnetic field as experienced by the satellite.

Unlike star trackers that must point in a specific direction to take measurements, or Sun sensors that can only take a measurement when the satellite is not in Earth's shadow, magnetometers provide measurements at all times throughout a satellite's orbit. Furthermore, modern magnetometers measure Earth's magnetic field with a high degree of precision. Magnetometer-only attitude estimation requires the use of highly accurate models of the Earth's magnetic field, such as the International Geomagnetic Reference Field (IGRF) [19].

There are several magnetometer-only attitude estimation techniques found in the literature. One of the earliest methods is DARDMOD, or deterministic attitude and rate determination using magnetometer-only data [20]. This method uses a batch of sequential magnetometer measurements as well as control law data, such as reaction wheel momentum or magnetic dipole moments. While the solution can be accurate to 10°, it requires solving an 8th order polynomial and is therefore inefficient [21]. Furthermore, it assumes no external disturbances act on the satellite and does not account for uncertainty in the measurements or the model. Kalman filtering can be used to improve the accuracy of magnetometer-only attitude estimation [22].

Psiaki et. al proposed a magnetometer-only EKF to estimate the attitude, angular rates, and disturbance torques for a gravity gradient stabilized spacecraft [22]. More recently, Ma et al. used an unscented Kalman filter (UKF) with magnetometer measurements to estimate the satellite attitude and calibrate the magnetometers [23]. An interesting EKF formulation using magnetometer measurements combined with readings from the satellite's solar cells to estimate attitude is presented in [24]. Another magnetometer-only EKF is presented in [25] to estimate a satellite's attitude and angular velocity and a second-order model is used to propagate the states. A two-step EKF was implemented in [15]. In the first step, the magnetometer measurement is filtered to provide the magnetic field derivative vector. This is combined with the magnetic field vector in the second step to fully resolve the satellite attitude and angular velocity. It was shown that the EKF com-

bined with an already calibrated filter provides computational efficiency over a UKF and has comparable accuracy [15].

Two interesting EKF variations using only magnetometer data formulated for simultatenous orbit and attitude estimation are presented in [26]. The first variation is an augmented dynamics EKF (ADEKF) in which the attitude dynamics and kinematics models are augmented with the orbit dynamics and kinematics to build up a single process
model. Two interlaced EKFs (IEKF) working simultaneously are introduced to reduce
the computational burden of dual attitude and orbit estimation. In both filters, the time
derivative of the magnetic field is used to estimate the satellite angular velocity and is obtained by differentiating a cubic polynomial fit of the magnetometer measurements [26].

1.1.2 Magnetic Attitude Control

The use of magnetorquers for attitude control is attractive for small satellite missions due to their low-cost, simplicity, and power efficiency [27]. The major drawback of using magnetorquers for attitude control purposes is that the torques generated are constrained to lie in the plane perpendicular to the magnetic field. For this reason the satellite is uncontrollable in the direction of the magnetic field. Full three axis controllability can be achieved only if there is enough variation in the magnetic field direction throughout the satellite's orbit [28]. Luckily, the Earth's magnetic field seen by a satellite on a near-polar orbit is approximately periodic, exhibiting enough variation on average for three axis controllability over time [29].

Magnetic actuation is commonly used to detumble a satellite after separation from the launch vehicle, as this can cause excessive initial angular momentum. The classical B-dot control law can be applied in this scenario [30]. The B-dot control law relates the commanded magnetic dipole moment to the measured rate of change of the magnetic field. Its simplicity and reliability make it the standard method for initial detumbling

of magnetically actuated satellites [31]. Magnetic attitude control is also often used for spin stabilization, in which the satellite is controlled to rotate at a high rate abot its major principal axis. In this case, magnetic actuation can be used to control the direction of the satellite's angular momentum. The bang-bang control law proposed in [32] is a popular scheme still used today, with extensive numerical simulations presented in [33]. The spin stabilization concept was used in the EyeSat mission for attitude control in safe mode, in which the satellite must use as few sensors and actuators as possible to limit failures while the batteries are recharged by the solar panels. To achieve this, a spin control law using only magnetic feedback was implemented to point EyeSat's solar panels toward the sun while maintatining a desired spin rate about its principal axis [34].

Of particular relevance to the Meteorix mission are magnetic attitude control algorithms used in momentum bias satellites. A momentum bias satellite incorporates a flywheel spinning at a constant rate to provide gyroscopic stability. Magnetic actuation can be used to provide any necessary rotation about the flywheel's spin axis. In many cases the flywheel's spin axis is aligned with the orbit normal and in this way the satellite is gravitationally stabilized in the orbital plane [31]. This is exactly the configuration of the Meteorix cubesat. A simple PD control law using the desired magnetic field and its derivative was developed for the momentum bias Gurwin-Techsat satellite and was shown to maintain three-axis stabilization [35]. A similar PD control law was implemented in the EyeSat mission to correct residual pointing errors about the guidance profile [36]. This is the same PD control law that was used in previous unpublished work on the Meteorix attitude control system in [37].

Given that the observation of meteors requires accurate attitude estimates, using these estimates as feedback to more sophisticated attitude control laws can provide better control performance. Optimal control is a popular approach used in this regard [31]. Lagrasta et al. developed an optimal state feedback control law with integral action to reduce

the effect of external torque disturbances on a LEO satellite with a pitch-axis momentum wheel [38]. A review of linear and nonlinear control using only magnetic actuation with an emphasis on optimal periodic control is presented in [39]. Linear Quadratic Regulation (LQR) is a popular theory applied to magnetic attitude control and is often implemented in a time-varying fashion by making use of the periodic nature of the Earth's magnetic field [29], [40]. Nonlinear control using magnetic actuation has also been studied extensively, particular sliding mode control. Sliding mode control is an attractive choice for magnetic attitude control as it can be shown to be asymptotically stable, and its nonlinearity makes it advantageous over other methods, such as PD control, in the presence of external disturbances [31]. Classic sliding mode control was first proposed for magnetic attitude control of the Orsted satellite in [41]. Several improvements to this control law can be found in [42], [43], and [44]. In [42] an additional term was introduced to the sliding mode control law for partial disturbance rejection and in [43] an integral sliding mode controller was formulated. This was expanded upon in [44] with a adaptive sliding manifold design including two time-integral terms. Other adaptive sliding mode control methods are presented in [45] and [46]. Zhou et al. formulated a modified sliding mode controller for a satellite with uncertain parameters, the BUAA-SAT microsatellite [45]. The control law deals with uncertainty in the principal moment of inertia and achieves an Earth-pointing attitude with high accuracy and stability. Li et al. proposed an adaptive fuzzy-logic sliding mode controller for a cubesat with three magnetic actuators and one pitch-axis reaction wheel and it is shown to have much better tracking performance than a classic PID controller [46].

Few papers were found that studied magnetometer-only attitude estimation and magnetic attitude control in combination. One noteable example is a modified state-dependent Ricatti equation (MDSRE) control law combined with a magnetometer-only EKF investigated in [47] and applied to EgyptSat-1 as a real test case to evaluate the ADCS performance. In [48], a similar magnetometer-only EKF for attitude and rate estimation

is combined with a PD feedback controller for a nadir-pointing magnetically actuated spacecraft.

1.2 Thesis Objectives

The aim of this thesis is to develop attitude estimation and control algorithms for the Meteorix cubesat to satisfy requirements imposed by the scientific objectives of the mission, given its unique sensor and actuator configuration. Before developing the ADCS, specific attitude estimation and control requirements must be outlined based on the scientific objectives, as well as the power needs of the satellite. The ADCS is formulated based on these requirements and the constraints on the system. For attitude estimation, the goal is to show that the MEKF using only magnetometer measurements can provide accurate and reliable estimates of the satellite's attitude and angular velocity. A comparison of the magnetometer-only MEKF with the traditional gyro-based MEKF is carried out to evaluate the estimator performance. The main requirement of the attitude controller is to reach and maintain the necessary pointing accuracy in each mission mode. A nonlinear sliding mode controller based on the literature is formulated for attitude control of Meteorix. The objective is to demonstrate that the sliding mode controller using state feedback from the magnetometer-only MEKF can reliably and sufficiently accurately control the satellite's attitude in each mission mode. To further evaluate its performance, it is compared to the simple PD magnetic feedback controller applied to Meteorix in previous work [37]. It is also shown that the sliding mode controller offers better performance than the PD controller in the presence of uncertainties in the satellite model.

1.3 Thesis Outline

Chapter 1 introduces the Meteorix project and motivation of this thesis and discusses relevant work in the topics of satellite attitude estimation and control. In Chapter 2, the

Meteorix mission design and objectives are presented with emphasis on the attitude estimation and control requirements. Chapter 3 details the satellite dynamics and kinematics models and various aspects of the simulation environment employed to evaluate the ADCS as developed in subsequent chapters. In Chapter 4, the magnetometer-only MEKF for attitude and angular velocity estimation is formulated and compared to the traditional gyro-based MEKF. The perfromance of both estimators is analyzed and compared with data from Monte Carlo simulations. Chapter 5 details the formulation of the sliding mode attitude controller and the simple PD magnetic feedback controller. The two control laws are compared in simulations of each mission mode. Chapter 5 also includes a sensitivity study to evaluate the ADCS performance in the presence of uncertainties and disturbances. Finally, Chapter 6 concludes the thesis with recommendations for future work on the Meteorix ADCS.

Chapter 2

Meteorix Mission

2.1 The Mission

The main objective of the Meteorix mission is to demonstrate that a low-cost nanosatellite equipped with a camera and an on-board detection chain can autonomously and accurately estimate the flux density of meteors and space debris entering the Earth's atmosphere. The ability to estimate the flow of meteors and space debris entering Earth's atmosphere is useful for many reasons. This data can be used to constrain existing meteor models such as the Interplanetery Meteoroids Environment for Exploration (IMEX) [49], and provide a first classification of the nature of the meteoroids, whether they are of asteroidal or cometary origin [2]. Furthermore, the space debris environment in LEO is becoming increasingly hazardous. It is estimated that there are hundreds of thousands of space debris 1 to 10 centimeters in size which are undetectable with current observation facilities on the ground. Objects of this size pose a threat to satellite's in LEO and can cause catastrophic damage; thus, it is essential to be able to monitor them. Measurements from Meteorix will provide information that can improve spatial distribution models of space debris.

Observations of meteors and space debris entering Earth's atmosphere can only be made

while Meteorix is in Earth's shadow. With this in mind, careful consideration was taken when selecting the satellite's orbit in [2]. It must be in Earth's shadow long enough to collect a sufficient amount of data; on the other hand, the satellite must be Sun-lit for long enough to charge the batteries and power the system. Therefore, the orbit chosen for the Meteorix mission is quasi-polar and Sun-synchronous at an altitude of 500 km, with an inclination of 97.4°, an ascending node fixed at 10:30 local mean solar time (LST), and a period of 94.7 minutes [2]. In such an orbit, the satellite is eclipsed by the Earth for approximately 35 minutes and Sun-lit for around 60 minutes.

2.1.1 Satellite Design

Meteorix is a 3U cubesat measuring 30x10x10 cm³ and its preliminary design and bodyfixed reference frame are shown in Figure 2.1. The body-fixed frame, \mathcal{F}_b , is fixed at the satellite's center of mass. The primary payload is a 3D Plus 3DCM681 micro-camera integrated with an optical lense that provides a 40° field of view. The camera is positioned at the bottom of the satellite along the z_b axis and must point toward the nadir to make observations. Four deployable solar panels will provide power to the satellite and charge its batteries while pointing toward the Sun. The attitude control system consists of an ISIS Magnetorquer Board (iMTQ) which has 3 perpendicular magnetic actuators, one for each of the satellite's principal axes and each capable of producing a maximum dipole moment of 0.2 Am² [50]. In addition, the satellite is equipped with one Hyperion Technologies RW210 momentum wheel oriented in a momentum bias configuration along the satellite's y_b -axis to provide gyroscopic stability. Attitude estimation must be realized with a single three-axis magnetometer which measures the ambient magnetic field experienced by the satellite, and a GPS receiver combined with communication between ground stations will provide position and velocity estimates. The cubesat has an estimated mass of 3.784 kg and its principal moments of inertia are estimated to be $J_{xx}=0.0586~{\rm kgm^2}$, $J_{yy}=0.0589$ kgm², $J_{zz} = 0.0482$ kgm². This preliminary design was proposed in the Meteorix mission feasibility review and details of the mission analysis are described in [2].

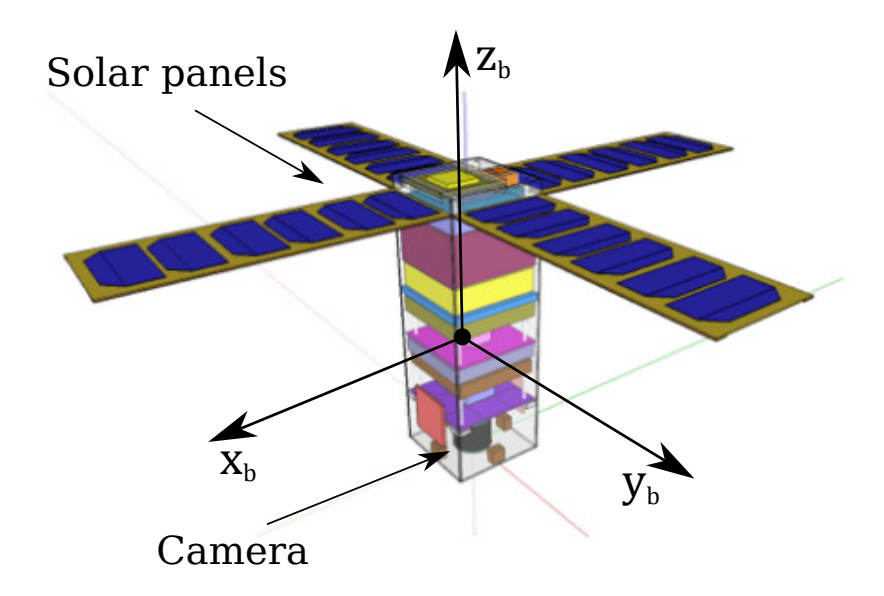


Figure 2.1: Preliminary design of the Meteorix satellite [2].

2.1.2 Modes of Operation

As mentioned in the introduction, the Meteorix mission is separated into three main modes of operation: (i) detumbling mode, (ii) alignment mode, and (iii) nominal mode, which as noted earlier, has two sub-modes; Earth-pointing and Sun-pointing. The purpose of detumbling mode is to reduce the satellite's angular velocity after departure from the launch vehicle. The departure causes the satellite to spin at an unknown rate, and in this state the satellite cannot make any observations of the Earth or accurately point its solar panels toward the Sun. The deployment of the solar panels can partially reduce the satellite's angular momentum but active control is required to further detumble the satellite to an acceptable angular rate. The alignment mode is activated when a near-zero angular rate is detected. In this mode, the satellite should point its solar panels toward the sun and align its y_b -axis with the orbit normal. Alignment with the orbit normal allows the satellite to take advantage of the gyroscopic stiffness provided by the flywheel and perform all subsequent maneuvers about this axis. Once good alignment has been achieved and the batteries have been fully recharged, the nominal mission mode is ac-

tivated. The satellite must alternate between pointing the camera toward the Earth to make observations and pointing the solar panels toward the Sun to recharge the batteries. Thus, two re-orientation maneuvers are to be performed during each orbit. To maximize the time for observations of meteors and space debris and assuming that ADCS takes 10 minutes to perform the reorientation, the maneuver to point the camera toward the Earth should be initiated 10 minutes before entering Earth's shadow. Subsequently, the maneuver to point the solar panels toward the Sun should be initiated only as the satellite exits Earth's shadow. This maximizes the time for meteor detection.

2.2 Power and Energy Analysis

It is necessary to verify that the satellite can receive enough power to sustain operation throughout the mission. The solar cell assembly chosen for the Meteorix mission is the TJ Solar Cell Assembly 3G30A from Azur Space Solar Power GmbH. The four solar panels each have six solar cells for a total of $n_s=24$ solar cells. Each cell has a surface area of $A_s=30.18 {\rm cm}^2$ and an energy efficiency of $\eta_s=29.3\%$ [51]. Considering the solar constant to be $S_R=1360.8~{\rm Wm}^{-2}$ [52] and the efficiency of the maximum power point tracking (MPPT) system to be $\eta_m=90\%$, the maximum power available from the solar panels is:

$$P_{max} = n_s \eta_s \eta_m S_R A_s \approx 25.99W \tag{2.1}$$

The actual power, P_s , generated by the solar panels and supplied to the satellite depends on the angle, θ_s , between the outward surface normal of the solar panels (also the \mathbf{z}_b axis) and the Sun direction. This is calculated with:

$$P_s = P_{max}cos(\theta_s) \tag{2.2}$$

An analysis on the power and energy consumption of the satellite's subsystems in the nominal mission mode allows us to determine if the satellite generates enough power to sustain full operation in nominal mode. Table 2.1 summarizes the estimated power consumption of each subsystem's components in the Earth-pointing and Sun-pointing modes. The high power consumption in Earth-pointing mode is due to the operation of the camera and the on-board meteor detection algorithm. Note that the values presented in Table 2.1 are merely estimates based on information from the EyeSat mission and a more in depth analysis should be performed prior to launch once the satellite design has been finalized. It is assumed that the power consumption during detumbling and alignment modes is equivalent to that in the Sun-pointing mode, as the camera and meteor detection chain will not be active.

Table 2.1: Power consumption of Meteorix subsystems during Earth-pointing and Sunpointing.

		Power Consu	imption (W)
Subsystem	Component	Earth-pointing	Sun-pointing
Command and Data handling	On-board computer	5.00	2.00
	Camera	2.00	0.20
	ADCS board	1.20	1.20
ADCS	Magnetorquers	1.00	1.00
	Reaction wheel	0.80	0.80
	Magnetometer	0.30	0.30
Communications	GPS receiver	0.12	0.12
	UHF/VHF	2.0	0.5
	S-band transceiver	2.0	0.5
Electrical power system	MPPT	0.2	0.2
Thermal control system	Thermoelectric cooler	2.0	2.0
	Total consumed power (W)	16.62	8.82

The satellite must use the energy stored in the batteries during Earth-pointing mode and during the attitude re-orientation maneuvers. With this information and using Table 2.1, the energy drawn from the batteries over one orbit can be estimated. First, let T_{ep} be the

time spent pointing the camera toward the Earth and let T_m be the time required for each of the reorientation maneuvers (assumed equal). The energy drawn from the batteries during one orbit is then:

$$E_b = P_{ep}T_{ep} + 2P_mT_m \tag{2.3}$$

It is assumed that the power consumed during maneuvers, P_m , is equivalent to that in Sun-pointing mode as the camera and on-board detection chain will not be active. In Sunpointing mode, the solar panels provide power to the satellite's subsystems and recharge the batteries in parallel. The energy consumed by the satellite in Sun-pointing mode is simply:

$$E_{sp} = P_{sp}T_{sp} \tag{2.4}$$

where P_{sp} , the power consumption in Sun-pointing mode, is obtained from Table 2.1 and T_{sp} is the time spent Sun-pointing. For one orbit, it is estimated that $T_{ep}=35$ minutes, $T_m=10$ minutes, and $T_{sp}=40$ minutes. The estimated total energy consumed over one orbit is therefore:

$$E_T = E_b + E_{sp} = 18.52 \,\text{Wh}$$
 (2.5)

It is assumed that the satellite's power distribution system has an efficiency of 90%. Using D-SPOSE, it was determined that the angle between Meteorix's orbital plane and the Sun direction is 22.5° . Thus, the best Sun-pointing angle that can be acheived while keeping the y_b axis aligned with the orbit normal is $\theta_s = 22.5^{\circ}$. Therefore, the maximum energy generated by the solar panels and supplied to the satellite is estimated to be:

$$E_s = 0.9P_sT_{sp} = 14.41 \,\text{Wh}$$
 (2.6)

Evidently, with the assumption that the camera and detection chain are active for the entire duration of Earth-pointing mode, the total energy consumed over one orbit is greater than the energy generated by the solar panels. Thus, to ensure that the energy in the batteries is not depleted below a safe threshold, the camera and on-board detection chain should not be operated for the entire duration of Earth-pointing mode.

2.3 Attitude Control and Estimation Requirements

To fulfill the scientific objectives of the mission, the satellite must be able to meet specific attitude control and estimation requirements during each mode of operation. In each mode, the attitude controller needs a desired attitude and angular velocity. The desired attitude is calculated from the desired body-fixed frame orientation defined by $\mathcal{F}_d = \{\mathbf{x}_d, \mathbf{y}_d, \mathbf{z}_d\}$. The main attitude control requirement is defined with a pointing angle, β , between the satellite's \mathbf{z}_b axis and the desired \mathbf{z}_d direction in the inertial frame. A secondary pointing angle, γ , defines the alignment of the satellite \mathbf{y}_b axis with the orbit normal. It is desired to maintain good alignment with the orbit normal to take advantage of the gyroscopic stability provided by the flywheel. The desired angular velocity of the satellite in each mode is defined by ω_d with a desired angular rate of $\omega_d = ||\omega_d||$. The satisfaction of the attitude estimation requirement in each mode is quantified with the total angular error, $\delta \alpha$, between the satellite's true attitude and the estimated attitude. Similarly, the quality of angular velocity estimation is defined with $\delta \omega$, the magnitude of the difference between the true and estimated angular velocity.

2.3.1 Detumbling Mode

The goal of detumbling mode is to simply reduce the satellite's angular momentum, so it does not have a strict attitude pointing requirement. The desired angular velocity passed to the attitude controller is simply zero. However, the satellite is considered to be detumbled and can transition to the alignment mode when its angular rate, $\omega = ||\omega||$, meets the following criteria:

$$\omega < 0.3$$
 °/s (2.7)

The widely used B-dot control only requires knowledge of the magnitude and direction of the magnetic field to successfully detumble the satellite. If the satellite's attitude and angular velocity are estimated, more sophisticated state feedback control laws can be employed to detumble the satellite with faster response time and more precision than B-dot control [31]. As stated in the introduction, a magnetometer-only MEKF is envisioned for attitude and angular velocity estimation which is fedback to a sliding mode attitude controller. The angular velocity estimate must be small enough for the attitude controller to successfully detumble the satellite. While there is no strict attitude estimation requirement in this mode, it is desired that the attitude estimate error be relatively small at the end of detumbling mode. Therefore, the estimation requirements in the detumbling mode are set as $\delta \alpha < 5$ ° and $\delta \omega < 0.1$ °/s.

2.3.2 Alignment Mode

This mode requires the attitude controller to point the solar panels toward the sun and also align the satellite's y_b -axis with the orbit normal. The desired orientation of the body-fixed frame in this mode is shown in Figure 2.2 and is expressed in the inertial frame as:

$$\mathbf{z}_{d} = \frac{\mathbf{n}_{o}^{\times}(\mathbf{r}_{sun}^{\times}\mathbf{n}_{o})}{||\mathbf{n}_{o}^{\times}(\mathbf{r}_{sun}^{\times}\mathbf{n}_{o})||}$$
(2.8)

$$\mathbf{y}_d = \frac{\mathbf{n}_o}{||\mathbf{n}_o||} \tag{2.9}$$

$$\mathbf{x}_d = \mathbf{y}_d^{\times} \mathbf{z}_d \tag{2.10}$$

where \mathbf{n}_o is the direction of the orbit normal and \mathbf{r}_{sun} is the Sun direction obtained from the Sun ephemeris data. The orbit normal direction is calculated through the cross product of the satellite's position and velocity vectors:

$$\mathbf{n}_o = \mathbf{r}^{\times} \mathbf{v} \tag{2.11}$$

The pointing angles β and γ are illustrated in Figure 2.2. By aligning the \mathbf{y}_b axis with the orbit normal, subsequent maneuvers only need to be performed about the orbit normal as the flywheel provides gyroscopic stability on the \mathbf{y}_b axis. Therefore the satellite should point its solar panels toward the Sun as best as possible while keeping \mathbf{y}_b well aligned with the orbit normal, and maintain a near-zero angular rate. The attitude control requirements in this mode are thus $\beta < 1^{\circ}$, $\gamma < 2^{\circ}$ and $\omega \approx 0^{\circ}/\mathrm{s}$. To achieve this pointing accuracy, the attitude controller requires good estimates of the satellite's state. Therefore the estimation requirements are set as $\delta \alpha < 2^{\circ}$ and $\delta \omega < 0.01^{\circ}/\mathrm{s}$.

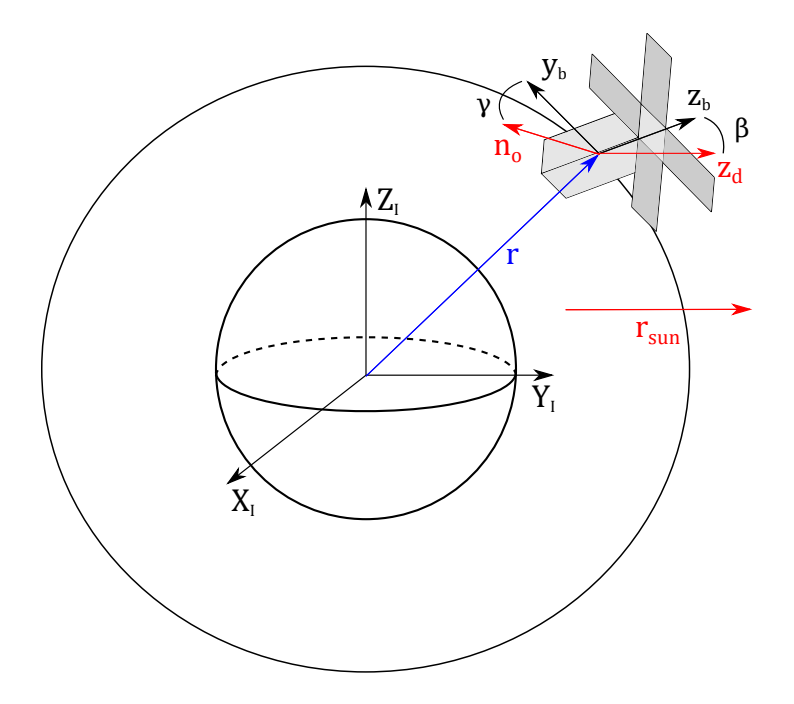


Figure 2.2: Desired orientation in alignment mode.

2.3.3 Nominal Mode

The desired satellite orientations in nominal mode are illustrated in Figure 2.3. To point the camera directly toward Earth, the satellite's \mathbf{z}_b axis must be aligned with the position vector, \mathbf{r} , and the \mathbf{y}_b axis must remain aligned with the orbit normal:

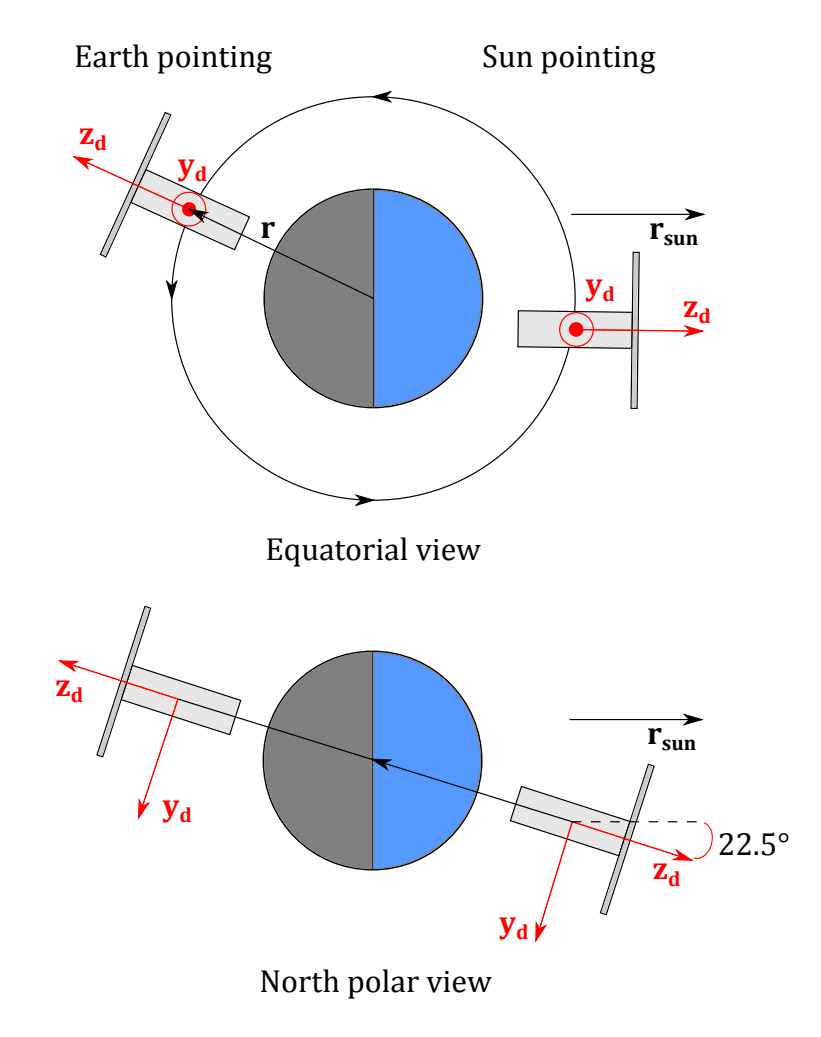


Figure 2.3: Desired orientations in nominal mode.

$$\mathbf{z}_d = \frac{\mathbf{r}}{||\mathbf{r}||} \tag{2.12}$$

$$\mathbf{y}_d = \frac{\mathbf{n}_o}{||\mathbf{n}_o||} \tag{2.13}$$

$$\mathbf{x}_d = \mathbf{y}_d^{\times} \mathbf{z}_d \tag{2.14}$$

The desired orientation in Sun-pointing mode is the same as that in alignment mode, described by Equations (2.8) - (2.10). As stated earlier, β defines the angle between \mathbf{z}_b and \mathbf{z}_d . The required pointing angles in Sun-pointing mode are $\beta < 1^\circ$ and $\gamma < 2^\circ$. In Earthpointing mode, a $\mathbf{z}_b - \mathbf{z}_d$ angle of $\beta < 20^\circ$ is adequate given that the camera has a 40°

Mode	Control Requirements		Estimation Requirements	
Detumbling		$\omega < 0.3^{\circ}/\mathrm{s}$	$\delta \alpha < 5^{\circ}$	$\delta\omega < 0.1^{\circ}/\mathrm{s}$
Alignment	β < 1°, γ < 2°	$\omega \approx 0^{\circ}/s$	$\delta \alpha < 2^{\circ}$	$\delta\omega < 0.01^{\circ}/\mathrm{s}$
Earth-pointing	$\beta < 20^{\circ}$, $\gamma < 2^{\circ}$	$\omega \approx 0.06^{\circ}/\mathrm{s}$	$\delta \alpha < 0.5^{\circ}$	$\delta\omega < 0.01^{\circ}/\mathrm{s}$
Sun-pointing	$\beta < 1^{\circ}, \gamma < 2^{\circ}$	$\omega \approx 0^{\circ}/\mathrm{s}$	$\delta \alpha < 0.5^{\circ}$	$\delta\omega < 0.01^{\circ}/\mathrm{s}$

Table 2.2: Attitude control and estimation requirements of the Meteorix mission.

field of view. The attitude estimation accuracy in Earth-pointing mode greatly impacts the meteor positioning accuracy [7]. It is shown in [7] that to achieve a desired meteor positioning accuracy of 1 km through stereoscopic measurements, the attitude estimate should be accurate to within 0.05° . However, this assumed that high accuracy sensors such as a star-tracker are used. As stated earlier, Meteorix will only use one magnetometer for attitude estimation and therefore a desired accuracy of $\delta \alpha < 0.5$ ° is proposed. This estimation accuracy should be maintained throughout the nominal mission mode.

In Sun-pointing mode, the desired angular velocity of the satellite is zero. To keep the camera pointing directly to nadir in the Earth-pointing mode, the satellite should rotate at a rate equal to its orbital rate, about the orbit normal:

$$\boldsymbol{\omega}_d = \frac{2\pi \mathbf{n}_o}{T} \tag{2.15}$$

where T is the orbital period. Given Meteorix's orbital period of approximately 94.7 minutes and keeping the \mathbf{y}_b axis aligned with the orbit normal, this represents a desired angular rate of $\omega_d \approx 0.06$ °/s about the \mathbf{y}_b axis. With this control requirement, required angular velocity estimate accuracy is set as $\delta\omega < 0.01$ °/s. To summarize, the attitude control and estimation requirements for each mission mode are listed in Table 2.2.

Chapter 3

Meteorix Simulation Model

The Meteorix simulation model is detailed in this chapter, starting with a description of the simulation environment in Section 3.1. The orbit and attitude dynamics and kinematics models are presented in Section 3.2, and the magnetic field model is outlined in Section 3.3. The perturbations included in the simulations of Meteorix are outlined in Section 3.4.

3.1 Simulation Environment

The Debris SPin/Orbit Simulation Environment (D-SPOSE) is a high-fidelity propagator developed by Sagnieres for long-term simulation of space debris [53]. This tool includes numerical integrator for propagating the satellite's orbit and attitude equations of motion and allows for the inclusion of several environmental models and external disturbances. The D-SPOSE framework, written in C, has been modified for the Meteorix mission to include the specific satellite model and the attitude estimation and control algorithms. The orbit and attitude equations of motion for Meteorix, as described in Section 3.2, are propagated using a fixed timestep, fifth order Runge-Kutta Dormand-Prince numerical integrator [54].

3.2 Equations of Motion

3.2.1 Orbit Dynamics

Orbital motion of a satellite is most commonly expressed in an Earth Centered Inertial (ECI) frame. In D-SPOSE, the True-Equator Mean-Equinox (TEME) ECI frame is used as it corresponds to the reference frame of Two-Line Element sets (TLE) describing the position with time of space objects which are input into D-SPOSE [53]. Throughout this thesis the TEME frame is referred to simply as the inertial frame. The orbital motion of the satellite is described by:

$$\ddot{\mathbf{r}} = -\frac{\mu}{r^3}\mathbf{r} + \sum_j \mathbf{a}_j(\mathbf{r}, \mathbf{v}, \mathbf{q}, \boldsymbol{\omega})$$
(3.1)

where μ is Earth's gravitational parameter, \mathbf{r} is the position of the spacecraft in the inertial frame and is a function of time, t, $r = ||\mathbf{r}||$, and \mathbf{v} is the satellite's velocity in the inertial frame. The terms \mathbf{a}_j represent the accelerations due to orbital perturbations, which are a function of the satellite's position, velocity, attitude, and angular velocity. The attitude is parameterized with a quaternion, \mathbf{q} , which describes the orientation of the body-fixed frame with respect to the inertial frame and ω is the angular velocity of the body-fixed frame with respect to the inertial frame. The position and velocity are all expressed in the inertial frame while the angular velocity is expressed in the body-fixed frame.

3.2.2 Attitude Dynamics and Kinematics

The attiude dynamics equation is evaluated in the body-fixed frame and relates the evolution of the satellite's angular velocity to the sum of external torques about the satellite's center of mass. The standard rotational equations of motion are augmented to account for the angular momentum of the flywheel on Meteorix as well as the magnetic actuation.

Thus, the attitude dynamice are defined by:

$$\mathbf{J}\dot{\boldsymbol{\omega}} + \boldsymbol{\omega}^{\times}(\mathbf{J}\boldsymbol{\omega} + \mathbf{H}_f) = \boldsymbol{\tau}_{mc} + \sum_{j} \boldsymbol{\tau}_{j}(\mathbf{r}, \mathbf{v}, \mathbf{q}, \boldsymbol{\omega})$$
 (3.2)

where **J** is Meteorix's inertia matrix, \mathbf{H}_f is the angular momentum of the flywheel, τ_{mc} is the control torque generated by the magnetic actuators, and τ_j are the perturbing torques which can be a function of the satellite's position, velocity, attitude, and angular velocity. The control torque is produced by the interaction of the magnetic actuators with Earth's magnetic field, \mathbf{B}_B , expressed in the body-fixed frame:

$$\tau_{mc} = \mathbf{m}_{act}^{\times} \mathbf{B}_{B} \tag{3.3}$$

in which \mathbf{m}_{act} is the vector of dipole moments produced by the magnetic actuators on each satellite body axis and is the input from the attitude controller. The control torque is clearly constrained to lie in a plane perpendicular to the magnetic field and the magnetic actuators alone cannot provide instantaneous three-axis controllability. With the flywheel oriented to spin about the satellite \mathbf{y}_b axis, its angular momentum in the satellite body-fixed frame is:

$$\mathbf{H}_f = \begin{bmatrix} 0 \\ H_f \\ 0 \end{bmatrix} \tag{3.4}$$

The flywheel is set to spin at a constant rate with an angular momentum of $H_f = 1.5 \times 10^{-3}$ Nms. This was chosen by the Meteorix design team and is taken from the Hyperion Technologies RW210 data sheet [55]. Note that on the real satellite, the magnetic actuators and flywheel must be calibrated prior to launch to calculate scale factors, misalignment terms, and any bias in their outputs. For the purposes of this thesis, they are assumed to be perfectly calibrated with no bias.

As noted earlier, the satellite's attitude is parameterized by the unit quaternion defined with scalar and vector parts as:

$$\mathbf{q} = \begin{bmatrix} q_0 \\ \mathbf{q}_v \end{bmatrix} \tag{3.5}$$

In this work the modern convention for quaternions is used as opposed to the Hamilton convention. The quaternion is a singularity-free attitude representation and it is subject to the unit norm constraint: $q_0^2 + \mathbf{q}_v^{\top} \mathbf{q}_v = 1$. The rotation matrix representation of the attitude is computed from the quaternion using:

$$\mathbf{C}(\mathbf{q}) = (q_0^2 - \mathbf{q}_v^{\mathsf{T}} \mathbf{q}_v) \mathbf{1}_{3 \times 3} + 2\mathbf{q}_v \mathbf{q}_v^{\mathsf{T}} - 2q_0 \mathbf{q}_v^{\mathsf{X}}$$
(3.6)

where $\mathbf{1}_{3\times3}$ is the identity matrix. This matrix transforms components of a vector in the inertial frame to those in the body-fixed frame. The attitude kinematics are described by:

$$\dot{\mathbf{q}} = \frac{1}{2}\mathbf{q} \otimes \begin{bmatrix} 0 \\ \omega \end{bmatrix} \tag{3.7}$$

where the \otimes operator represents the quaternion product. In this work, the following definition of the quaternion product is used:

$$\mathbf{q} \otimes \mathbf{p} = \begin{bmatrix} q_0 p_0 - \mathbf{q}_v^{\top} \mathbf{p}_v \\ q_0 \mathbf{p}_v + p_0 \mathbf{q}_v - \mathbf{q}_v^{\times} \mathbf{p}_v \end{bmatrix}$$
(3.8)

For implementation, it is convenient to express the attitude kinematics with an alternative representation of Equation (3.7) given by:

$$\dot{\mathbf{q}} = \frac{1}{2}\mathbf{\Omega}(\boldsymbol{\omega})\mathbf{q} \tag{3.9}$$

where $\Omega(\omega)$ is a 4x4 matrix formed with components of ω :

$$oldsymbol{\Omega}(oldsymbol{\omega}) = egin{bmatrix} 0 & -oldsymbol{\omega}^{ op} \ oldsymbol{\omega} & -oldsymbol{\omega}^{ imes} \end{bmatrix}$$

It is useful to calcuate the Euler angle representation of the attitude for analysis purposes, as the quaternion can be difficult to interpret. The 3-2-1 Euler angles are calculated from the quaternion with:

$$\psi = \operatorname{atan2}(2(q_0q_3 + q_1q_2), 1 - 2(q_2^2 + q_3^2))$$
(3.10)

$$\theta = \arcsin(2(q_0q_2 - q_3q_1)) \tag{3.11}$$

$$\phi = \operatorname{atan2}(2(q_0q_1 + q_2q_3), 1 - 2(q_1^2 + q_2^2))$$
(3.12)

where ψ , θ , and ϕ represent the yaw, pitch, and roll angles, respectively.

3.3 Magnetic Field Model

D-SPOSE uses the 13th Generation International Geomagnetic Reference Field (IGRF) to model the Earth's magnetic field [19]. The IGRF provides a 13th order spherical harmonic expansion of the Earth's magnetic potential in the Earth-Centered Earth-Fixed (ECEF) frame [53] and is given by:

$$V(r,\phi,\lambda,t) = a \sum_{n=1}^{k} (\frac{a}{r})^{n+1} \sum_{m=0}^{n} (g_n^m(t)cos(m\lambda) + h_n^m(t)sin(m\lambda)) P_n^m[cos(\phi)]$$
 (3.13)

where r is the radial distance from the center of the Earth, a is the geomagnetic convention for Earth's mean reference spherical radius, ϕ is the colatitude, and λ is the longitude. The Gauss coefficients, g_n^m and h_n^m , are functions of time and are obtained from the IGRF coefficients table [56]. A recursive algorithm is included in D-SPOSE to obtain the Schmidt normalized associated Legendre functions, P_n^m , evaluated at ϕ [53]. The magnetic field

vector in the ECEF frame is calculated with:

$$\mathbf{B} = -\nabla V \tag{3.14}$$

In D-SPOSE, the magnetic field vector, \mathbf{B} , is transformed from the ECEF frame to the inertial frame to get \mathbf{B}_I . The details of this transformation as well as the derivation of an anatytical expression for $\dot{\mathbf{B}}_I$, the time rate of change of the magnetic field in the inertial frame, are given in [53]. The magnetic field vector and its derivative in the body-fixed frame are calculated with:

$$\mathbf{B}_B = \mathbf{C}(\mathbf{q})\mathbf{B}_I \tag{3.15}$$

$$\dot{\mathbf{B}}_B = \mathbf{C}(\mathbf{q})\dot{\mathbf{B}}_I - \boldsymbol{\omega}^{\times}\mathbf{B}_B \tag{3.16}$$

In Chapter 4, Equations (3.15) and (3.16) are reintroduced as the measurement model of the magnetomter-only MEKF.

3.4 Perturbations

3.4.1 Standard LEO perturbations

In this work, the following environmental perturbations are included in the propagation of the orbit and attitude dynamics: aerodynamic drag and torque, acceleration due to non-spherical Earth gravitational terms and torque due to gravity gradient, and solar radiation pressure and torque. These are three of the most prominent perturbations for nanosatellites in LEO. The models used for these perturbations are listed in Table 3.1 and the equations describing how these perturbations are calculated in D-SPOSE can be found in [53]. To model the aerodynamic drag and solar radiation pressure perturbations, a tessalated surface geometry model of Meteorix was built by Sagnieres in [37]. The satellite

is composed of 28 triangular surfaces with its solar panels in their open configuration as shown in Figure 3.1. A drag coefficient $c_D=2.2$ is used in the calculation of aerodynamic drag and torque. The effects of winds arising from co-rotating atmosphere are also considered. The solar radiation pressure parameters are set as $A_p=2$ and $F_{10.7}=80sfu$ (1 sfu = 10^{-22} Wm⁻²Hz⁻¹). A_p is a planetary index reflecting the amount of geomagnetic activity, while $F_{10.7}$ is the solar radio flux at 10.7 cm [37]. The coefficients of absorption (σ_a) , diffuse reflection (σ_{rd}) , and specular reflection (σ_{rs}) of each surface of the satellite are needed for calculating the effects of solar radiation pressure. The coefficients are assumed to be the same for all surfaces with $\sigma_a=0.4$, $\sigma_{rd}=0.4$, and $\sigma_{rs}=0.2$, except for the solar panels which are set to $\sigma_a=0.7$, $\sigma_{rd}=0.25$, and $\sigma_{rs}=0.05$ [37]. The Sun direction, ${\bf r}_{sun}$, is obtained from planetary ephemerides provided by the Virtual Observatory of the Institut de Mécanique Céleste et de Calcul des Éphémérides assuming a starting date of January 5, 2010 [57].

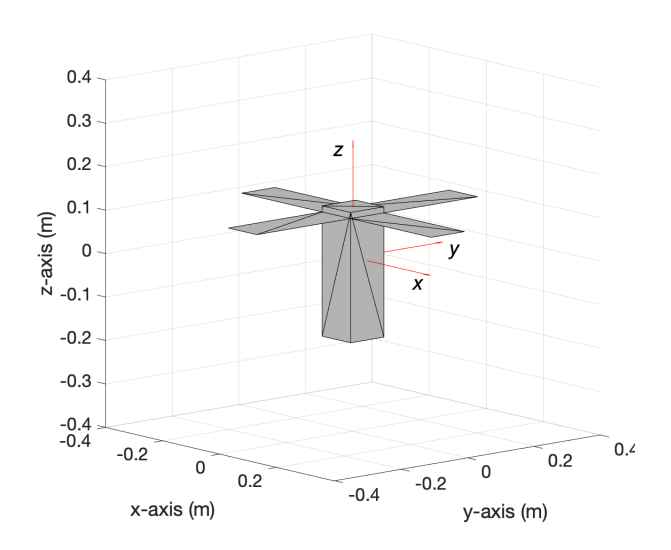


Figure 3.1: Tesselated surface geometry model of Meteorix in the body-fixed frame

An analysis on the effect of the perturbing torques on the Meteorix mission was carried out in [37]. It was found that the gravity gradient, aerodynamic, and solar radiation pressure torques are all similar in magnitude, on the order of 10^{-8} Nm. For comparison, the

Perturbation Model

Aerodynamic drag and torque NRLMSISE-00 [58]

Gravity gradient acceleration and torque EGM2008 [59]

Solar radiation pressure and torque Montenbruck and Gill [60]

Table 3.1: Perturbation models.

magnetic actuators produce torques on the order of 10^{-6} - 10^{-5} Nm on average. Simulation results showed that the baseline PD attitude controller can perform adequately well against these perturbations [37]. However, the aerodynamic torque is shown to increase with higher solar activity. Additional simulations were performed with $A_p = 80$ and $F_{10.7} = 250$ sfu, resulting in aerodynamic torques to be on the order of 10^{-6} Nm. This had an adverse affect on attitude control, causing the ponting errors in Earth- and Sun-pointing modes to reach approximately 20° and 40° , respectively [37].

3.4.2 Residual Magnetic Moment

The effect of residual magnetic moment was not studied in [37]. However for small satellites such as Meteorix, the torque caused by the residual magnetic moment is often much more significant than the three perturbations discussed above. The residual magnetic moment, \mathbf{m}_r , interacts with the magnetic field to produce a perturbing torque analogously to Equation (3.3):

$$\boldsymbol{\tau}_{mr} = \mathbf{m}_r^{\times} \mathbf{B}_B \tag{3.17}$$

The effect of the residual magnetic moment on the EyeSat mission was studied in [34]. It was shown that the pointing accuracy of EyeSat's magnetic attitude control law worsens with increasing residual magnetic moment. A residual magnetic moment with a magnitude of 0.035 Am² results in an average pointing accuracy of 40°. This represents a moment of 0.02 Am² on each body-fixed frame axis, equivalent to 10 % of the maximum dipole moment produced by each magnetorquer. The EyeSat team recommended that the

residual magnetic moment must be lower than 10% of the magnetic actuation capacity in all directions [34]. In this thesis, the residual magnetic moment is first assumed to be zero for the formulation of the attitude estimation and control algorithms in Chapter 4 and 5. Its effect on the ADCS performance is analyzed in a sensitivity study at the end of Chapter 5, and methods for estimation and compensation of the residual magnetic moment are discussed.

Chapter 4

Attitude Estimation

In this chapter a magnetometer-only MEKF is formulated for attitude and angular velocity estimation of the Meteorix satellite. First, a general EKF formulation is presented in Section 4.1 to show the basic algorithm structure for state estimation of nonlinear systems. The traditional gyro-based MEKF is then detailed in Section 4.2 and its advantages over the EKF for handling quaternions are highlighted. This provides the basis from which the magnetometer-only MEKF is derived in Section 4.3. The implementation of the algorithms and the key differences between the gyro-based MEKF and magnetometer-only MEKF are then discussed in Section 4.4. In Section 4.5, the performance of each estimation algorithm is evaluated through Monte Carlo simulations.

4.1 Extended Kalman Filter

The EKF is a well established tool for state estimation of nonlinear systems and is known to deal effectively with uncertainty that arises from noisy sensor data [12]. As such, it is a commonly used algorithm for sattelite attitude estimation. The EKF operates in a recursive manner, consisting of a predicton step and an update step. It uses the dynamics model of the system, linearized about the previous state estimate, to predict the current state. It then updates the state estimate using a weighted average of the predicted state

and measurements from sensors. The weights are calculated from the covariance, a measure of the uncertainty of the system, and more weight is given to the values with the least uncertainty. The resulting state estimate is proven to be closer to the true state than both the predicted and measured values [12].

We start by formulating an EKF for a general nonlinear system described by the following process and measurement models:

$$\dot{\mathbf{x}}(t) = \mathbf{f}(\mathbf{x}, \mathbf{u}, t) + \mathbf{w}(t) \tag{4.1}$$

$$\mathbf{z}(t) = \mathbf{h}(\mathbf{x}, t) + \boldsymbol{\eta}(t) \tag{4.2}$$

where $\mathbf{x} \in \mathbb{R}^{n \times 1}$ is the system state, $\mathbf{u} \in \mathbb{R}^{p \times 1}$ is the control input to the system, and $\mathbf{z} \in \mathbb{R}^{m \times 1}$ is the measurement from the system's sensors. Uncertainty in the system is represented by \mathbf{w} in the process model and $\boldsymbol{\eta}$ in the measurement model. These are assumed to be zero-mean white Gaussian processes and therefore have normal probability distributions with covariances $\mathbf{Q} \in \mathbb{R}^{n \times n}$ and $\mathbf{R} \in \mathbb{R}^{m \times m}$, respectively:

$$\mathbf{p}(\mathbf{w}) \sim N(0, \mathbf{Q}) \tag{4.3}$$

$$\mathbf{p}(\boldsymbol{\eta}) \sim N(0, \mathbf{R}) \tag{4.4}$$

Defining the estimate error as $\delta \mathbf{x} = \mathbf{x} - \hat{\mathbf{x}}$, the error covariance, $\mathbf{P} \in \mathbb{R}^{n \times n}$, defined by:

$$\mathbf{P} = cov(\mathbf{x} - \hat{\mathbf{x}}) = E\{ [\mathbf{x} - \hat{\mathbf{x}}]^{\top} [\mathbf{x} - \hat{\mathbf{x}}] \}$$
(4.5)

describes the likelihood of the state estimate. For implementation on a satellite's flight computer, it is necessary to formulate the EKF algorithm in discrete-time. The predicted state estimate at timestep k, defined as $\hat{\mathbf{x}}_k^-$, is obtained by propagating the state estimate

from the previous timestep, $\hat{\mathbf{x}}_{k-1}$, using the following discrete prediction model:

$$\hat{\mathbf{x}}_{k}^{-} = \hat{\mathbf{x}}_{k-1} + \mathbf{f}(\hat{\mathbf{x}}_{k-1}, \mathbf{u}_{k-1}) \Delta t \tag{4.6}$$

This is simply the first order approximation of the process model in Equation (4.1). The predicted error covariance is then propagated with:

$$\mathbf{P}_{k}^{-} = \mathbf{\Phi}_{k-1} \mathbf{P}_{k-1} \mathbf{\Phi}_{k-1}^{\mathsf{T}} + \mathbf{Q} \Delta t \tag{4.7}$$

where Φ_{k-1} is the first-order state transition matrix:

$$\mathbf{\Phi}_{k-1} = \mathbf{1}_{n \times n} + \mathbf{F}_{k-1} \Delta t \tag{4.8}$$

and \mathbf{F}_{k-1} is the Jacobian of the process model evaluated at the previous state estimate and control input:

$$\mathbf{F}_{k-1} = \frac{\partial \mathbf{f}}{\partial \mathbf{x}} \Big|_{\hat{\mathbf{x}}_{k-1}, \mathbf{u}_{k-1}} \tag{4.9}$$

In the above, Δt is the update rate of the estimator and is typically chosen to be equal to the sampling rate of the system's sensors or the on board computer. The measurement residual is defined by:

$$\mathbf{v}_k = \mathbf{z}_k - \mathbf{h}(\hat{\mathbf{x}}_k^-) \tag{4.10}$$

This signifies the discrepancy between the measurement and the estimated measurement. The state estimate is updated at every timestep by multiplying the measurement residual with the Kalman gain, $\mathbf{K}_k \in \mathbb{R}^{n \times m}$:

$$\mathbf{K}_k = \mathbf{P}_k^{\mathsf{T}} \mathbf{H}_k^T (\mathbf{H}_k \mathbf{P}_k^{\mathsf{T}} \mathbf{H}_k^{\mathsf{T}} + \mathbf{R})$$
 (4.11)

$$\hat{\mathbf{x}}_k = \hat{\mathbf{x}}_k^- + \mathbf{K}_k \mathbf{v}_k \tag{4.12}$$

In Equation (4.11), the matrix $\mathbf{H}_k \in \mathbb{R}^{m \times n}$ is the Jacobian of the measurement model evaluated at the predicted state estimate:

$$\mathbf{H}_{k} = \frac{\partial \mathbf{h}}{\partial \mathbf{x}} \Big|_{\hat{\mathbf{x}}_{k}^{-}} \tag{4.13}$$

Finally, the error covariance is updated with:

$$\mathbf{P}_k = (\mathbf{1}_{n \times n} - \mathbf{K}_k \mathbf{H}_k) \mathbf{P}_k^{-} (\mathbf{1}_{n \times n} - \mathbf{K}_k \mathbf{H}_k)^{\top} + \mathbf{K}_k \mathbf{H}_k \mathbf{K}_k^{\top}$$
(4.14)

The general EKF algorithm is summarized in Table 4.1. In the next section a modified version of the EKF is introduced for application to attitude estimation — the Multiplicative Extended Kalman Filter (MEKF).

Table 4.1: The EKF algorithm.

$$\begin{split} \textbf{Initialize} & \quad \hat{\mathbf{x}}_0 = E(\mathbf{x}_0) \\ & \quad \mathbf{P}_0 = E\{[\mathbf{x}_0 - \hat{\mathbf{x}}_0]^\top [\mathbf{x}_0 - \hat{\mathbf{x}}_0]\} \end{split}$$

$$\begin{split} \textbf{Predict} & \quad \hat{\mathbf{x}}_k^- = \hat{\mathbf{x}}_{k-1} + \mathbf{f}(\hat{\mathbf{x}}_{k-1}, \mathbf{u}_{k-1}) \Delta t \\ & \quad \mathbf{P}_k^- = \Phi_{k-1} \mathbf{P}_{k-1} \Phi_{k-1}^\top + \mathbf{Q} \Delta t \end{split}$$

$$\end{split}$$

$$\begin{split} \textbf{Update} & \quad \mathbf{K}_k = \mathbf{P}_k^- \mathbf{H}_k^T (\mathbf{H}_k \mathbf{P}_k^- \mathbf{H}_k^\top + \mathbf{R})^{-1} \\ & \quad \hat{\mathbf{x}}_k = \hat{\mathbf{x}}_k^- + \mathbf{K}_k \mathbf{v}_k \\ & \quad \mathbf{P}_k = (\mathbf{1}_{n \times n} - \mathbf{K}_k \mathbf{H}_k) \mathbf{P}_k^- (\mathbf{1}_{n \times n} - \mathbf{K}_k \mathbf{H}_k)^\top + \mathbf{K}_k \mathbf{H}_k \mathbf{K}_k^\top \end{split}$$

4.2 Multiplicative Extended Kalman Filter

As shown in Chapter 3, the satellite's attitude is represented with a unit quaternion, $\mathbf{q} = [q_0, \mathbf{q}_v]^{\mathsf{T}}$, which must satisfy the unit norm constraint given by: $q_0^2 + \mathbf{q}_v^{\mathsf{T}} \mathbf{q}_v = 1$. The most straight forward way to estimate the quaternion is to treat it like any other vector state and use Equations (4.6) and (4.12); however, the additive prediction and update

equations can clearly violate the unit norm constraint and normalization of the quaternion is required after every update. This can result in larger than necessary estimation errors. A popular variation of the EKF that properly handles the quaternion is the MEKF and the formulation presented here is drawn from [14]. The MEKF estimates the quaternion error of the estimate instead of the quaternion and updates the estimate by multiplying the error by the predicted quaternion. This is proven to limit the estimation error caused by the unit norm constraint [14]. The quaternion error is updated with magnetometer measurements, while the predicted quaternion is obtained by propagating the quaternion kinematics with measurement from a gyroscope. As such, we refer to this formulation as the gyro-based MEKF. The attitude quaternion error is defined by:

$$\delta \mathbf{q} = \mathbf{q} \otimes \hat{\mathbf{q}}^{-1} \tag{4.15}$$

where ${\bf q}$ is the true quaternion and $\hat{{\bf q}}$ is the estimated quaternion, both assumed to be unit quaternions. The inverse of a unit quaternion is defined through

$$\mathbf{q}^{-1} = \begin{bmatrix} q_0 \\ -\mathbf{q}_v \end{bmatrix} \tag{4.16}$$

The quaternion error kinematics can be shown to be [14]:

$$\delta \dot{\mathbf{q}} = -\begin{bmatrix} 0 \\ \hat{\boldsymbol{\omega}}^{\times} \delta \mathbf{q}_{v} \end{bmatrix} + \frac{1}{2} \delta \mathbf{q} \otimes \begin{bmatrix} 0 \\ \delta \boldsymbol{\omega} \end{bmatrix}$$
(4.17)

where $\delta \omega$ is the angular velocity estimate error given by:

$$\delta \omega = \omega - \hat{\omega} \tag{4.18}$$

If the estimated quaternion is "close" to the true quaternion, we can assume $\delta \mathbf{q} \approx [1\ 0\ 0\ 0]^{\mathsf{T}}$ and obtain the following first-order approximation of the quaternion error kinematics

[14]:

$$\delta \dot{\mathbf{q}} \approx -\begin{bmatrix} 0 \\ \hat{\boldsymbol{\omega}}^{\times} \delta \mathbf{q}_v \end{bmatrix} + \frac{1}{2} \begin{bmatrix} 0 \\ \delta \boldsymbol{\omega} \end{bmatrix}$$
 (4.19)

which can be simplified to:

$$\delta \dot{q}_0 = 0 \tag{4.20}$$

$$\delta \dot{\mathbf{q}}_v = -\hat{\boldsymbol{\omega}}^{\times} \delta \mathbf{q}_v + \frac{1}{2} \delta \boldsymbol{\omega}$$
 (4.21)

Thus, the dimension of the system in the MEKF can be reduced by one state by removing the scalar part of the quaternion error. This reduces the computational complexity of the algorithm and makes implementation on real systems easier than an EKF that estimates the full quaternion. As mentioned above, the gyroscope measurement is used to propagate the quaternion estimate in the prediction step. However, any bias in the gyroscope measurement will accumulate and cause significant drift and error in the state estimate. Therefore, the gyro-based MEKF estimates the following error state:

$$\delta \mathbf{x} = \begin{bmatrix} \delta \mathbf{q}_v \\ \delta \mathbf{b}_g \end{bmatrix} \tag{4.22}$$

where $\delta \mathbf{b}_g = \mathbf{b}_g - \hat{\mathbf{b}}_g$ is the gyroscope bias error. A widely used gyroscope sensor model is:

$$\omega = \tilde{\omega} - \mathbf{b}_a - \eta_v \tag{4.23}$$

$$\dot{\mathbf{b}}_g = \boldsymbol{\eta}_u \tag{4.24}$$

where $\tilde{\omega}$ is the measurement, \mathbf{b}_g is the gyro bias, and η_v and η_u are independent zeromean Gaussian noise processes with covariances $\sigma_v^2 \mathbf{1}_{3\times 3}$ and $\sigma_u^2 \mathbf{1}_{3\times 3}$. In practice, σ_v and σ_u are referred to as the angular random walk and rate random walk, respectively. These parameters are often provided by the manufacturer. The angular velocity estimate is obtained by subtracting the estimated gyroscope bias from the gyroscope measurement:

$$\hat{\boldsymbol{\omega}} = \tilde{\boldsymbol{\omega}} - \hat{\mathbf{b}}_q \tag{4.25}$$

and the angular velocity error is therefore:

$$\delta \boldsymbol{\omega} = \boldsymbol{\omega} - \hat{\boldsymbol{\omega}} = -(\delta \mathbf{b}_q + \boldsymbol{\eta}_v) \tag{4.26}$$

It is common practice to assume the gyroscope bias is constant, and thus the process model of the gyro-based MEKF is defined by the following error dynamics [14]:

$$\delta \dot{\mathbf{x}} = \mathbf{f} = \begin{bmatrix} -\hat{\boldsymbol{\omega}}^{\times} \delta \mathbf{q}_v + \frac{1}{2} \delta \boldsymbol{\omega} \\ \mathbf{0} \end{bmatrix}$$
(4.27)

Although the MEKF estimates the error state, the full state defined by

$$\mathbf{x} = \begin{bmatrix} \mathbf{q} \\ \mathbf{b}_g \end{bmatrix} \tag{4.28}$$

is still predicted and updated at each timestep. The gyro-based MEKF predicts the current state using the previous estimated state and gyroscope measurement as follows:

$$\hat{\boldsymbol{\omega}}_{k}^{-} = \tilde{\boldsymbol{\omega}} - \hat{\mathbf{b}}_{a|k-1} \tag{4.29}$$

$$\hat{\mathbf{q}}_k^- = \hat{\mathbf{q}}_{k-1} + \frac{1}{2} \mathbf{\Omega}(\hat{\boldsymbol{\omega}}_k^-) \hat{\mathbf{q}}_{k-1} \Delta t$$
(4.30)

$$\hat{\mathbf{b}}_{g|k}^{-} = \hat{\mathbf{b}}_{g|k-1} \tag{4.31}$$

The error covariance is handled in the same way as in the EKF. It is predicted with Equation (4.7) and updated with (4.14). However, it does not have the same meaning as in the EKF. It represents the likelihood of the error state, not the likelihood of the actual state estimate, and is therefore more difficult to interpret. As such, the measurement residual

is often used as an indicator of the MEKF performance. The process Jacobian is obtained by substituting Equation (4.26) into (4.27) and evaluating the following:

$$\mathbf{F}_{k-1} = \frac{\partial \mathbf{f}}{\partial (\delta \mathbf{x})} \Big|_{\hat{\mathbf{x}}_{k-1}} = \begin{bmatrix} -\hat{\boldsymbol{\omega}}_{k-1}^{\times} & -\frac{1}{2} \mathbf{1}_{3 \times 3} \\ \mathbf{0}_{3 \times 3} & \mathbf{0}_{3 \times 3} \end{bmatrix}$$
(4.32)

Measurement from a single 3-axis magnetometer is used to update the quaternion error and gyroscope bias error. The magnetometer measures the magnetic field in the body-fixed frame which is related to the satellite's attitude with respect to the inertial frame through:

$$\mathbf{B}_B = \mathbf{C}(\mathbf{q})\mathbf{B}_I \tag{4.33}$$

where C(q) is the true attitude matrix and B_I is obtained from the IGRF model, as described in Chapter 3. In practice, the magnetometer is modelled with:

$$\mathbf{B}_m = \mathbf{A}_m \mathbf{B}_B + \mathbf{b}_m + \boldsymbol{\eta}_m \tag{4.34}$$

where A_m is the callibration matrix of scale factors and misalignments terms, b_m is the magnetometer bias vector, and η_m is the sensor noise. It is assumed that the magnetometer is perfectly callibrated, and thus the sensor model is reduced to:

$$\mathbf{B}_m = \mathbf{B}_B + \boldsymbol{\eta}_m \tag{4.35}$$

The measurement model of the gyro-based MEKF is therefore:

$$\mathbf{h}(\mathbf{x}) = \mathbf{B}_B = \mathbf{C}(\mathbf{q})\mathbf{B}_I \tag{4.36}$$

$$\mathbf{z} = \mathbf{B}_m = \mathbf{h}(\mathbf{x}) + \boldsymbol{\eta}_m \tag{4.37}$$

The measurement Jacobian can be expressed in a simple form. First, the true attitude matrix is defined by:

$$C(\mathbf{q}) = C(\delta \mathbf{q})C(\hat{\mathbf{q}}) \tag{4.38}$$

The estimated measurement is defined as $\mathbf{h}(\hat{\mathbf{x}}^-) = \mathbf{C}(\hat{\mathbf{q}}^-)\mathbf{B}_I$. Making use of the first-order approximation of the attitude error matrix given by

$$\mathbf{C}(\delta \mathbf{q}) = \mathbf{1}_{3 \times 3} - 2[\delta \mathbf{q}_v]^{\times} \tag{4.39}$$

the estimation error of the magnetometer measurement is simply:

$$\delta \mathbf{h} = \mathbf{h}(\mathbf{x}) - \mathbf{h}(\hat{\mathbf{x}}^{-}) = 2[\mathbf{C}(\hat{\mathbf{q}}^{-})\mathbf{B}_{I}]^{\times} \delta \mathbf{q}_{v}$$
(4.40)

Therefore, the measurement Jacobian of the gyro-based MEKF at timestep k is:

$$\mathbf{H}_{k} = \frac{\partial(\delta \mathbf{h})}{\partial(\delta \mathbf{x})}\Big|_{\hat{\mathbf{x}}_{k}^{-}} = \begin{bmatrix} 2[\mathbf{C}(\hat{\mathbf{q}}_{k}^{-})\mathbf{B}_{I}]^{\times} & \mathbf{0}_{3\times3} \end{bmatrix}$$
(4.41)

In the update step the Kalman gain is calculated with Equation (4.11) and is partitioned as $\mathbf{K}_k = [\mathbf{K}_{q|k}, \ \mathbf{K}_{b|k}]^{\mathsf{T}}$. Then, the quaternion estimate is updated as follows:

$$\delta \hat{\mathbf{q}}_{v|k} = \mathbf{K}_{q|k} \mathbf{v}_k \tag{4.42}$$

$$\delta \mathbf{q}_k^* = \begin{bmatrix} 1\\ \frac{1}{2}\delta \hat{\mathbf{q}}_{v|k} \end{bmatrix} \tag{4.43}$$

$$\hat{\mathbf{q}}_k = \delta \hat{\mathbf{q}}_k^* \otimes \hat{\mathbf{q}}_k^- \tag{4.44}$$

Since the quaternion error is assumed to be small, the small angle approximation $\delta \mathbf{q}_k^* = [1 \ \frac{1}{2} \delta \mathbf{q}_{v|k}]^{\mathsf{T}}$, is applied in Equation (4.43). The quaternion estimate must be normalized after the update step as the approximation still violates the unit norm constraint. However, since the quaternion error represents a small rotation, the magnitude of the constraint violation is less than if the full quaternion and additive update equation were used [14].

Lastly, the gyroscope bias estimate is updated with

$$\delta \hat{\mathbf{b}}_{g|k} = \mathbf{K}_{b|k} \mathbf{v}_k \tag{4.45}$$

$$\hat{\mathbf{b}}_{g|k} = \hat{\mathbf{b}}_{g|k}^{-} + \delta \hat{\mathbf{b}}_{g|k} \tag{4.46}$$

4.3 Magnetometer-only MEKF

The magnetometer-only MEKF derived in this section assumes that a gyroscope is not used to estimate the satellite's angular velocity. Instead of using the bias adjusted gyroscope measurements to obtain the angular velocity estimate, the calculated time rate of change of the magnetic field is used to estimate the angular velocity error directly. In addition, the satellite's attitude dynamics model is used to propagate the angular velocity estimate in the prediction step. Therefore, the magnetometer-only MEKF estimates the following error state:

$$\delta \mathbf{x} = \begin{bmatrix} \delta \mathbf{q}_v \\ \delta \boldsymbol{\omega} \end{bmatrix} \tag{4.47}$$

and the corresponding full state is thus:

$$\mathbf{x} = \begin{bmatrix} \mathbf{q} \\ \boldsymbol{\omega} \end{bmatrix} \tag{4.48}$$

The process model of the magnetometer-only MEKF consists of the quaternion error kinematics given by Equation (4.21), and the angular velocity error dynamics. To derive the angular velocity error dynamics, first recall the satellite attitude dynamics from Equation (3.2) in Chapter 3, written in a slightly different form and excluding any external disturbances:

$$\dot{\boldsymbol{\omega}} = \mathbf{J}^{-1}(-\boldsymbol{\omega}^{\times}(\mathbf{J}\boldsymbol{\omega} + \mathbf{H}_f) + \boldsymbol{\tau}_{mc})$$
(4.49)

The true magnetic control torque is given by:

$$\tau_{mc} = \mathbf{u}^{\times} \mathbf{B}_{B} = \mathbf{u}^{\times} (\mathbf{C}(\mathbf{q}) \mathbf{B}_{I}) \tag{4.50}$$

However, since the true attitude matrix C(q) is not known, the filter must use the estimated magnetic control torque in the propagation of the estimated angular velocity. The estimated magnetic control torque is defined by:

$$\hat{\boldsymbol{\tau}}_{mc} = \mathbf{u}^{\times}(\mathbf{C}(\hat{\mathbf{q}})\mathbf{B}_{I}) \tag{4.51}$$

and the error dynamics are then derived as:

$$\delta \dot{\boldsymbol{\omega}} = \mathbf{J}^{-1} (-\hat{\boldsymbol{\omega}}^{\times} (\mathbf{J} \delta \boldsymbol{\omega}) + (\mathbf{J} \hat{\boldsymbol{\omega}})^{\times} \delta \boldsymbol{\omega} + \mathbf{H}_{f}^{\times} \delta \boldsymbol{\omega} + \delta \boldsymbol{\tau}_{mc})$$
(4.52)

where $\delta \tau_{mc} = \tau_{mc} - \hat{\tau}_{mc}$. The process model of the magnetometer-only MEKF is thus defined by:

$$\delta \dot{\mathbf{x}} = \mathbf{f} = \begin{bmatrix} -\hat{\boldsymbol{\omega}}^{\times} \delta \mathbf{q}_v + \frac{1}{2} \delta \boldsymbol{\omega} \\ \mathbf{J}^{-1} (-\hat{\boldsymbol{\omega}}^{\times} (\mathbf{J} \delta \boldsymbol{\omega}) + (\mathbf{J} \hat{\boldsymbol{\omega}})^{\times} \delta \boldsymbol{\omega} + \mathbf{H}_f^{\times} \delta \boldsymbol{\omega} + \delta \boldsymbol{\tau}_{mc}) \end{bmatrix}$$
(4.53)

and the process Jacobian is calculated by taking the partial derivative of the process model with respect to the error state, evaluated at the previous state estimate and control input:

$$\mathbf{F}_{k-1} = \frac{\partial \mathbf{f}}{\partial (\delta \mathbf{x})} \Big|_{\hat{\mathbf{x}}_{k-1}, \mathbf{u}_{k-1}} = \begin{bmatrix} -\hat{\boldsymbol{\omega}}_{k-1}^{\times} & \frac{1}{2} \mathbf{1}_{3 \times 3} \\ 2\mathbf{J}^{-1}(\mathbf{u}_{k-1}^{\times} [\mathbf{C}(\hat{\mathbf{q}}_{k-1})\mathbf{B}_{I}]^{\times}) & \mathbf{J}^{-1}(\mathbf{H}_{f}^{\times} - \hat{\boldsymbol{\omega}}_{k-1}^{\times} \mathbf{J} + [\mathbf{J}\hat{\boldsymbol{\omega}}_{k-1}]^{\times}) \end{bmatrix}$$

$$(4.54)$$

It is important to distinguish between the process model that is used to derive the process Jacobian and the equations used to propagate the full state in the prediction step. The full quaternion and angular velocity estimates are propagated with:

$$\hat{\mathbf{q}}_{k}^{-} = \hat{\mathbf{q}}_{k-1} + \frac{1}{2} \mathbf{\Omega}(\hat{\boldsymbol{\omega}}_{k-1}) \hat{\mathbf{q}}_{k-1} \Delta t$$
(4.55)

$$\hat{\boldsymbol{\omega}}_{k}^{-} = \hat{\boldsymbol{\omega}}_{k-1} + \mathbf{f}_{\boldsymbol{\omega}}(\hat{\mathbf{x}}_{k-1}, \mathbf{u}_{k-1}) \Delta t \tag{4.56}$$

where \mathbf{f}_{ω} is given by Equation (4.49) and is evaluated with the previous state estimate and control input.

To update the angular velocity estimate, the magnetometer-only MEKF takes the rate of change of the magnetic field in the body-fixed frame, defined by:

$$\dot{\mathbf{B}}_B = \mathbf{C}(\mathbf{q})\dot{\mathbf{B}}_I - \boldsymbol{\omega}^{\times} \mathbf{B}_B \tag{4.57}$$

The full measurement model of the magnetometer-only MEKF is therefore:

$$\mathbf{h}(\mathbf{x}) = \begin{bmatrix} \mathbf{B}_B \\ \dot{\mathbf{B}}_B \end{bmatrix} = \begin{bmatrix} \mathbf{C}(\mathbf{q})\mathbf{B}_I \\ \mathbf{C}(\mathbf{q})\dot{\mathbf{B}}_I - \boldsymbol{\omega}^{\times}\mathbf{B}_B \end{bmatrix} = \begin{bmatrix} \mathbf{C}(\mathbf{q})\mathbf{B}_I \\ \mathbf{C}(\mathbf{q})\dot{\mathbf{B}}_I - \boldsymbol{\omega}^{\times}(\mathbf{C}(\mathbf{q})\mathbf{B}_I) \end{bmatrix}$$
(4.58)

and the measurement is:

$$\mathbf{z} = \begin{bmatrix} \mathbf{B}_m \\ \dot{\tilde{\mathbf{B}}}_m \end{bmatrix} = \mathbf{h}(\mathbf{x}) + \boldsymbol{\eta} \tag{4.59}$$

where $\dot{\hat{\mathbf{B}}}_m$ is the filtered finite difference of \mathbf{B}_m . This is calculated in two steps. First, $\dot{\mathbf{B}}_m$ is obtained through the following finite difference:

$$\dot{\mathbf{B}}_{m|k} = \frac{\mathbf{B}_{m|k} - \mathbf{B}_{m|k-1}}{\Delta t} \tag{4.60}$$

where Δt is the magnetometer sampling rate. Next, a first-order low pass filter is applied to reduce the noise resulting from the finite difference. For an input signal X and an output signal Y, a linear, time-invariant digital filter is described by the transfer function

H(z) in the frequency domain (z):

$$H(z) = \frac{Y}{X} = \frac{B(z)}{A(z)} = \frac{b_0 + b_1 z^{-1} + b_2 z^{-2} + \dots + b_n z^{-n}}{1 + a_1 z^{-1} + a_2 z^{-2} + \dots + a_n z^{-n}}$$
(4.61)

where n is the order of the filter and $B = [b_0, b_1, ...b_n]$ and $A = [1, a_1, ...a_n]$ are the transfer function coefficients. In discrete-time, the filter is implemented as a difference equation obtained by solving:

$$Ay = Bx (4.62)$$

For a first order filter (n = 1) we obtain:

$$y_k = b_0 x_k + b_1 x_{k-1} - a_1 y_{k-1} (4.63)$$

This is a recursive filter, known as an infinite impulse response (IIR) filter, that depends on the current and previous input as well as the previous output. In the magnetomter-only MEKF, $\dot{\mathbf{B}}_m$ is filtered to obtain $\dot{\tilde{\mathbf{B}}}_m$:

$$\dot{\tilde{\mathbf{B}}}_{m|k} = b_0 \dot{\mathbf{B}}_{m|k} + b_1 \dot{\mathbf{B}}_{m|k-1} - a_1 \dot{\tilde{\mathbf{B}}}_{m|k-1}$$
(4.64)

The coefficients b_0 , b_1 , and a_1 are calculated using Matlab's butter function. The user defined inputs to this function are the order, n, and normalized cutoff frequency, W_n . In this work, the normalized cutoff frequency was chosen by comparing the signal generated by the finite difference (Equation (4.60) to the true derivative of the magnetic field in the satellite body-fixed frame (Equation (4.57). The Earth's magnetic field changes relatively slowly from the perspective of the Meteorix satellite, with a period of approximately 1 orbit. Considering the magnetometer is sampled at 1 Hz ($\Delta t = 1$ s), a normalized cutoff frequency of $W_n = 0.01$ is shown to filter the signal reasonably well.

The measurement model of the magnetometer-only MEKF is defined in Equation (4.58)

and it is straight forward to obtain the measurement Jacobian at timestep k as:

$$\mathbf{H}_{k} = \frac{\partial \mathbf{h}}{\partial (\delta \mathbf{x})} \Big|_{\hat{\mathbf{x}}_{k}^{-}} = \begin{bmatrix} 2[\mathbf{C}(\hat{\mathbf{q}}_{k}^{-})\mathbf{B}_{I}]^{\times} & \mathbf{0}_{3\times3} \\ 2([\mathbf{C}(\hat{\mathbf{q}}_{k}^{-})\dot{\mathbf{B}}_{I}]^{\times} - \hat{\boldsymbol{\omega}}_{k}^{-\times}[\mathbf{C}(\hat{\mathbf{q}}_{k}^{-})\mathbf{B}_{I}]^{\times}) & [\mathbf{C}(\hat{\mathbf{q}}_{k}^{-})\mathbf{B}_{I}]^{\times} \end{bmatrix}$$
(4.65)

The Kalman gain is calculated with Equation (4.11) and is partitioned as $\mathbf{K}_k = [\mathbf{K}_{q|k}, \ \mathbf{K}_{w|k}]^{\top}$. The quaternion and angular velocity estimates are then updated as follows:

$$\delta \hat{\mathbf{q}}_{v|k} = \mathbf{K}_{q|k} \mathbf{v}_k \tag{4.66}$$

$$\delta \hat{\mathbf{q}}_k^* = \begin{bmatrix} 1\\ \frac{1}{2} \delta \hat{\mathbf{q}}_{v|k} \end{bmatrix} \tag{4.67}$$

$$\hat{\mathbf{q}}_k = \delta \hat{\mathbf{q}}_k^* \otimes \hat{\mathbf{q}}_k^- \tag{4.68}$$

$$\delta \hat{\boldsymbol{\omega}}_k = \mathbf{K}_{\boldsymbol{\omega}|k} \mathbf{v}_k \tag{4.69}$$

$$\hat{\boldsymbol{\omega}}_k = \hat{\boldsymbol{\omega}}_k^- + \delta \hat{\boldsymbol{\omega}}_k \tag{4.70}$$

4.4 Implementation

The two attitude estimation methods are implemented within the DSPOSE framework and are summarized in Table 4.2. It is important to reiterate some of the differences between the two methods. One of the main differences is in the measurement model. The magnetometer-only MEKF estimates the satellite's angular velocity by taking the derivative of the magnetometer reading and treating it as a measurement. This requires some extra computation by means of the finite difference and low pass filter described in Equations (4.60) and (4.64), respectively. The gyro-based MEKF does not produce the angular velocity estimate explicitly, but only the attitude and gyroscope bias estimates. It uses the magnetometer measurement only for updating the attitude estimate, and as a result the measurement model is of smaller size. In particular, the magnetometer-only MEKF has $\mathbf{z}_k \in \mathbb{R}^{6\times 1}$, $\mathbf{H}_k \in \mathbb{R}^{6\times 6}$, $\mathbf{R} \in \mathbb{R}^{6\times 6}$ while the gyro-based MEKF has $\mathbf{z}_k \in \mathbb{R}^{3\times 1}$, $\mathbf{H}_k \in \mathbb{R}^{3\times 6}$,

Table 4.2: Estimator summary.

	Gyro-based MEKF				
Measurement	$\mathbf{z}_k = \left[\mathbf{B}_m ight]$				
State Prediction	$\hat{\mathbf{q}}_k^- = \hat{\mathbf{q}}_{k-1} + \frac{1}{2}\mathbf{\Omega}(\hat{\boldsymbol{\omega}}_k^-)\hat{\mathbf{q}}_{k-1}\Delta t \qquad \hat{\boldsymbol{\omega}}_k^- = \tilde{\boldsymbol{\omega}}_k - \hat{\mathbf{b}}_{g k-1} \qquad \hat{\mathbf{b}}_{g k}^- = \hat{\mathbf{b}}_{g k-1}$				
Process Jacobian	$\mathbf{F}_{k-1} = egin{bmatrix} -\hat{oldsymbol{\omega}}_{k-1}^{ imes} & -rac{1}{2}1_{3 imes 3} \ 0_{3 imes 3} & 0_{3 imes 3} \end{bmatrix}$				
Measurement Jacobian	$\mathbf{H}_k = \begin{bmatrix} 2[\mathbf{C}(\hat{\mathbf{q}}_k^-)\mathbf{B}_I]^{\times} & 0_{3\times 3} \end{bmatrix}$				
State Update	$\delta \hat{\mathbf{q}}_{v k} = \mathbf{K}_{q k} \mathbf{v}_{k} \qquad \delta \hat{\mathbf{b}}_{g k} = \mathbf{K}_{b k} \mathbf{v}_{k}$ $\delta \hat{\mathbf{q}}_{k}^{*} = \begin{bmatrix} 1 \\ \frac{1}{2} \delta \hat{\mathbf{q}}_{v k} \end{bmatrix} \qquad \hat{\mathbf{b}}_{g k} = \hat{\mathbf{b}}_{g k}^{-} + \delta \hat{\mathbf{b}}_{g k}$ $\hat{\mathbf{q}}_{k} = \delta \hat{\mathbf{q}}_{k}^{*} \otimes \hat{\mathbf{q}}_{k}^{-}$				
	Magnetometer-only MEKF				
Measurement	$\mathbf{z}_k = egin{bmatrix} \mathbf{B}_m \ \dot{\hat{\mathbf{B}}}_m \end{bmatrix}$				
State Prediction	$\hat{\mathbf{a}}_{k-1}^- = \hat{\mathbf{a}}_{k-1} + \frac{1}{5} \mathbf{\Omega}(\hat{\boldsymbol{\omega}}_{k-1}) \hat{\mathbf{a}}_{k-1} \Delta t$ $\hat{\boldsymbol{\omega}}_{k-1}^- = \hat{\boldsymbol{\omega}}_{k-1} + \mathbf{f}_{\omega}(\hat{\mathbf{x}}_{k-1}, \mathbf{u}_{k-1}) \Delta t$				

$$\begin{array}{lll} \text{Measurement} & \mathbf{z}_k = \begin{bmatrix} \mathbf{B}_m \\ \dot{\tilde{\mathbf{B}}}_m \end{bmatrix} \\ \text{State Prediction} & \hat{\mathbf{q}}_k^- = \hat{\mathbf{q}}_{k-1} + \frac{1}{2} \mathbf{\Omega}(\hat{\omega}_{k-1}) \hat{\mathbf{q}}_{k-1} \Delta t & \hat{\omega}_k^- = \hat{\omega}_{k-1} + \mathbf{f}_{\boldsymbol{\omega}}(\hat{\mathbf{x}}_{k-1}, \mathbf{u}_{k-1}) \Delta t \\ \\ \text{Process Jacobian} & \mathbf{F}_{k-1} = \begin{bmatrix} -\hat{\omega}_{k-1}^{\times} & \frac{1}{2} \mathbf{1}_{3 \times 3} \\ 2\mathbf{J}^{-1}(\mathbf{u}_{k-1}^{\times}[\mathbf{C}(\hat{\mathbf{q}}_{k-1})\mathbf{B}_I]^{\times}) & \mathbf{J}^{-1}(\mathbf{H}_f^{\times} - \hat{\omega}_{k-1}^{\times}\mathbf{J} + [\mathbf{J}\hat{\omega}_{k-1}]^{\times}) \end{bmatrix} \\ \text{Measurement Jacobian} & \mathbf{H}_k = \begin{bmatrix} 2[\mathbf{C}(\hat{\mathbf{q}}_k^-)\mathbf{B}_I]^{\times} & \mathbf{0}_{3 \times 3} \\ 2([\mathbf{C}(\hat{\mathbf{q}}_k^-)\hat{\mathbf{B}}_I]^{\times} - \hat{\omega}_k^{\times}[\mathbf{C}(\hat{\mathbf{q}}_k^-)\mathbf{B}_I]^{\times}) & [\mathbf{C}(\hat{\mathbf{q}}_k^-)\mathbf{B}_I]^{\times} \end{bmatrix} \\ \text{State Update} & \delta \hat{\mathbf{q}}_{v|k} = \mathbf{K}_{q|k}\mathbf{v}_k & \delta \hat{\omega}_k = \mathbf{K}_{\omega|k}\mathbf{v}_k \\ \delta \hat{\mathbf{q}}_k^* = \begin{bmatrix} 1 \\ \frac{1}{2}\delta \hat{\mathbf{q}}_{v|k} \end{bmatrix} & \hat{\omega}_k = \hat{\omega}_k^- + \delta \hat{\omega}_k \\ \hat{\mathbf{q}}_k = \delta \hat{\mathbf{q}}_k^* \otimes \hat{\mathbf{q}}_k^- \end{aligned}$$

 $\mathbf{R} \in \mathbb{R}^{3 \times 3}$. A second key difference between the two methods is in the propagation of the states. The magnetometer-only MEKF uses the attitude dynamics model to propagate the angular velocity estimate and is therefore susceptible to uncertainties in the model. These uncertainties can arise from unmodelled disturbance torques, errors in the satel-

lite's moments of inertia, or errors in the flywheel parameters. The gyro-based MEKF uses the bias adjusted gyroscope measurement to update the angular velocity estimate which then propagates the quaternion estimate. While it is not as susceptible to the uncertainties mentioned above, it has it's own limitations. The first is that the predicted angular velocity estimate obtained from $\hat{\omega}_k^- = \tilde{\omega}_k - \hat{\mathbf{b}}_{g|k-1}$ can be particularly noisy depending on the characteristics of the gyroscope. Consequently, a low pass filter should be applied if $\hat{\omega}$ is to be fed back to the attitude controller. Secondly, if the satellite's angular velocity is relatively slow and the initial gyroscope bias estimates are far off from the truth, the gyro-based MEKF may have poor convergence time.

The performance of both attitude estimation methods is affected by many factors including the sensor noise parameters, the initial estimate errors, and tunable parameters. The magnetometer and gyroscope noise parameters are listed in Table 4.3. The values were obtained from the data sheets of the Honeywell HMC5883L magnetometer [61] and the Analog Devices ADIS16405 IMU [62], respectively. The tunable parameters for both estimation methods are the initial error covariance, P_0 , and the process covariance, P_0 . They were chosen by running several simulations with fixed initial conditions and varying the values of P_0 and Q. The parameters which provided the best results for each estimator are used for all simulations presented in this thesis and are summarized in Table 4.4.

Table 4.3: Sensor noise parameters.

$$\sigma_m = 200 \text{ [nT]}$$
 $\sigma_v = 4.89 \times 10^{-4} \text{ [rad/s}^{1/2]}$ $\sigma_u = 3.14 \times 10^{-5} \text{ [rad/s}^{3/2]}$

4.5 Simulation Results

The Monte Carlo method is used to compare the two estimation methods by averaging the performance over 100 simulation runs with a wide range of initial estimates. The

Estimator	Parameter	Value		
	R	$diag[\sigma_m^21_{3\times3},(2\sigma_m)^21_{3\times3}]$		
Magnetometer-only MEKF	Q	$\text{diag}[(1\times 10^{-8})1_{3\times 3}, (1\times 10^{-9})1_{3\times 3}]$		
	\mathbf{P}_0	$\mathrm{diag}[(1\times 10^{-3})1_{3\times 3},(1\times 10^{-6})1_{3\times 3}]$		
	R	$[\sigma_m^2 1_{3 imes 3}]$		
Gyro-based MEKF	Q	$diag[(1\times 10^{-9})1_{3\times 3}, (1\times 10^{-10})1_{3\times 3}]$		
	\mathbf{P}_0	$\text{diag}[(1\times 10^{-3})1_{3\times 3}, (1\times 10^{-9})1_{3\times 3}]$		

Table 4.4: Estimator parameters.

attitude estimate error is first initialized with:

$$\delta \mathbf{q}_0 = \begin{bmatrix} \cos(\delta \alpha_0/2) \\ \mathbf{a}_0 \sin(\delta \alpha_0/2) \end{bmatrix}$$
(4.71)

The angle, $\delta\alpha_0$, and the axis, \mathbf{a}_0 , are selected randomly by a sphere point picking method as follows:

$$\delta\alpha_0 = \mathcal{U}(0,30) \quad [^{\circ}] \tag{4.72}$$

$$\mathbf{a}_0 = \begin{bmatrix} \sqrt{1 - v^2} \cos(\phi) \\ \sqrt{1 - v^2} \sin(\phi) \\ v \end{bmatrix}$$
(4.73)

where $v = \mathcal{U}(-1,1)$, $\phi = \mathcal{U}(0,2\pi)$, and \mathcal{U} represents a uniform random distribution. The initial attitude estimate is then calculated with $\hat{\mathbf{q}}_0 = \delta \mathbf{q}_0 \otimes \mathbf{q}_0$. The angular velocity estimate is initialized with

$$\hat{\boldsymbol{\omega}}_0 = \boldsymbol{\omega}_0 - \delta \boldsymbol{\omega}_0 \tag{4.74}$$

where the components of $\delta \omega_0$ are chosen as $\delta \omega_{i,0} = \mathcal{U}(-2,2)$ [°/s]. Similarly, for the gyrobased MEKF the gyroscope bias estimate is initialized with

$$\hat{\mathbf{b}}_{q|0} = \mathbf{b}_{q|0} - \delta \mathbf{b}_{q|0} \tag{4.75}$$

and $\delta b_{g|i,0} = \mathcal{U}(-0.01, 0.01)$ [°/s].

Two initial angular velocity scenarios are considered and summarized in Table 4.5. In each scenario, the satellite's attitude is initialized in the Earth-pointing orientation. In the tumbling scenario, the satellite's angular velocity is initialized to a moderate tumbling rate of 4 °/s on all axes. In the Earth-pointing scenario the satellite is initialized to spin only about its pitch axis at a rate equal to its orbital rate. This is the desired angular velocity of the satellite in the Earth-pointing phase of the nominal mode, in which the performance requirement of the attitude estimation is most strict.

Table 4.5: Initial angular velocity scenarios.

Tumbling	$\omega_0 = \begin{bmatrix} 4 & 4 & 4 \end{bmatrix}$ °/s
Earth-pointing	$\omega_0 = [0\ 0.06341\ 0] ^{\circ}/\mathrm{s}$

The metrics used to assess the accuracy of each estimator are the root mean square (RMS) errors in the estimated states. The RMS angular velocity errors are calculated as the RMS of the difference between the true and estimated angular velocity for each body-fixed frame component ($\omega_x, \omega_y, \omega_z$). Specific to the gyro-based MEKF, the RMS gyroscope bias errors are calculated as the RMS of the difference between the true and estimated gyro-scope bias, also for each body-fixed frame component. For the attitude estimation accuracy, the quaternion error can be difficult to interpret. Instead, the Euler angle errors as well as the total angular error are calculated. To calculate the Euler angle errors, the quaternion error is obtained from Equation (4.15) and then used in Equations (3.10) -

(3.12) to get $\delta \psi$, $\delta \theta$, and $\delta \phi$. The total angular error is calculated with:

$$\delta \alpha_k = 2\cos^{-1}(\delta q_{0|k}) \tag{4.76}$$

$$\delta\alpha = \sqrt{\sum_{k=1}^{N} \frac{\delta\alpha_k^2}{N}} \tag{4.77}$$

For both initial angular velocity scenarios, the two estimation methods are analyzed using data from 100 simulations with the state estimates initialized as described in Equations (4.71) - (4.75). For all simulations, the satellite dynamics are propagated for 15 orbits - approximately 1 day - with a timestep of $\Delta t = 1$ s. Estimation with either method is initialized at t = 0 and is executed with a timestep of $\Delta t = 1$ s. The performance is assessed without active attitude control, and therefore the control input, u, is zero for all t.

4.5.1 Tumbling Scenario

The estimation results of the tumbling scenario are summarized in Tables 4.6 - 4.8. It was found that both estimators converge within 1 orbit. For the Meteorix mission, the long term accuracy of the estimator is prioritized over convergence time and as such all RMS errors are calculated starting at t=1 orbit, rather than t=0. Table 4.6 shows the average RMS Euler angle and total angular errors of each estimator with their respective standard deviations. Tables 4.7 and 4.8 show the angular velocity errors and the gyroscope bias errors, respectively, also with their standard deviations. The estimation errors of the gyrobased MEKF and magnetometer-only MEKF over the first 30 minutes of each simulation are shown in Figures 4.1 and 4.2, respectively. The magnetometer-only MEKF was found to diverge in one out of the 100 Monte Carlo simulations and is not shown. The overall estimation accuracy of the magnetometer-only MEKF suffers in the tumbling scenario. The gyro-based MEKF shows better average RMS attitude estimate errors but the standard deviations are an order of magnitude higher than those of the magnetometer-only MEKF.

Furthermore, the average RMS angular velocity estimate error with the magnetometer-only MEKF is slightly better than with the gyro-based MEKF. These results are explained by the fact that cubesat-grade gyroscopes typically have poor noise characteristics. Both estimators meet the attitude estimate requirement of $\delta\alpha < 5\,^{\circ}$ in detumbling mode, but not the angular velocity estimate requirement of $\delta\omega < 0.1\,^{\circ}/s$. The estimation accuracy is expected to improve with active attitude control working to detumble the satellite.

Table 4.6: Attitude estimate errors in the tumbling scenario.

	Average RMS Error [°]				
Estimator	± Standard Deviation [°]				
	$\delta \psi$	$\delta \theta$	$\delta\phi$	$\delta \alpha$	
Magnetometer-only MEKF	2.3929	2.6858	2.3669	4.3064	
	0.0074	0.0062	0.0058	0.0108	
Gyro-based MEKF	1.4353	1.5745	1.4242	2.5624	
	0.0678	0.0786	0.0764	0.1274	

Table 4.7: Angular velocity estimate errors in the tumbling scenario.

	Average RMS Error [°/s]			
Estimator	\pm Standard Deviation [°/s]			
	$\delta\omega_x$	$\delta\omega_y$	$\delta\omega_z$	
Magnetometer-only MEKF	0.0996	0.0669	0.1035	
	0.0058	0.0190	0.0035	
Gyro-based MEKF	0.1811	0.0665	0.1517	
	0.0012	0.0113	0.0006	

Table 4.8: Gyroscope bias error of the gyro-based MEKF in the tumbling scenario.

	Average RMS Error [°/s]			
Estimator	\pm Standard Deviation [°/s]			
	$\delta b_{g x}$	$\delta b_{g y}$	$\delta b_{g z}$	
Gyro-based MEKF	0.0234	0.0334	0.0223	
	0.0016	0.0138	0.0008	

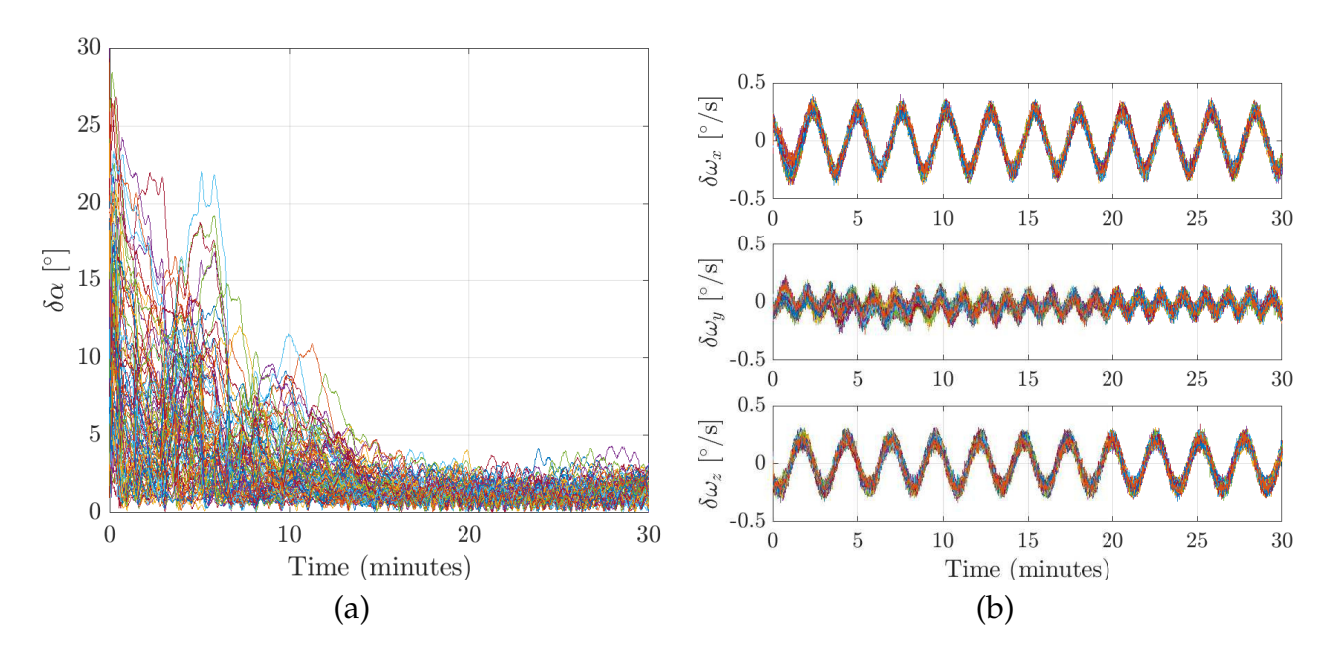


Figure 4.1: Gyro-based MEKF estimation errors in tumbling scenario from t=0 to t=30 minutes. (a) Total angular error, (b) Angular velocity error

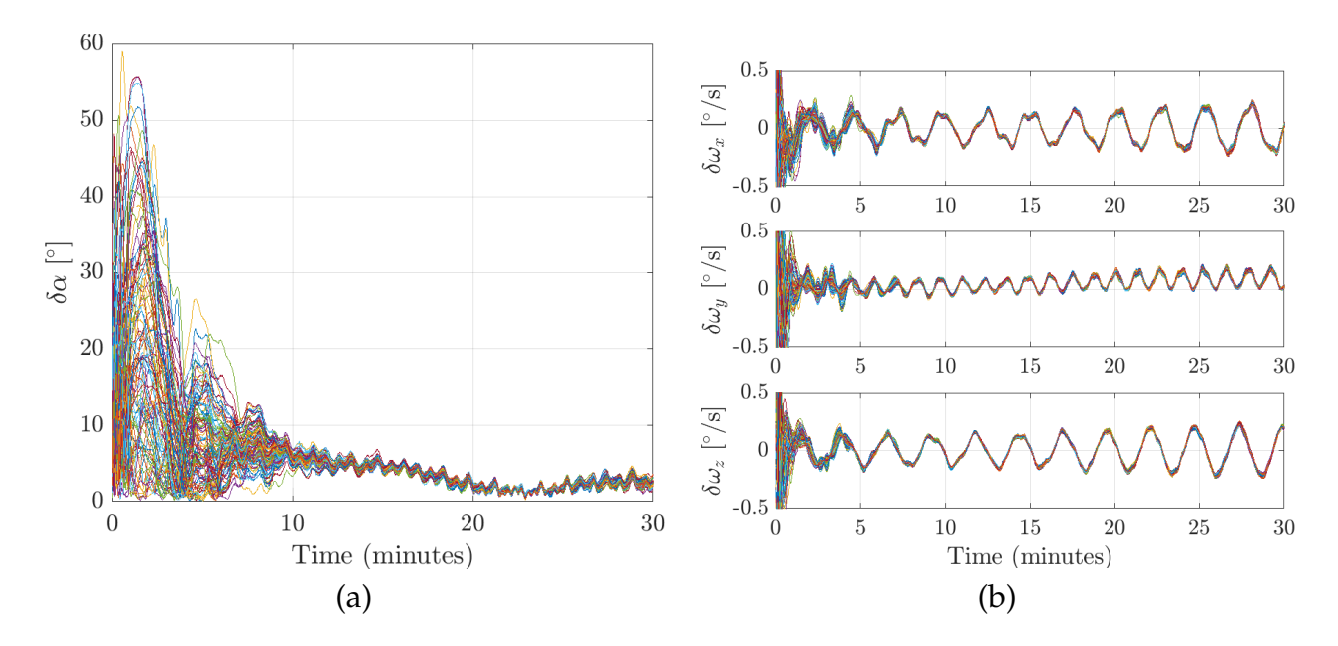


Figure 4.2: Magnetometer-only MEKF estimation errors in tumbling scenario from t=0 to t=30 minutes. (a) Total angular error, (b) Angular velocity error

4.5.2 Earth-Pointing Scenario

In the Earth-pointing scenario, the gyro-based MEKF diverged in all 100 Monte Carlo simulations. The signal to noise ratio of the gyroscope is too small to accurately measure the low angular rate. However, the magnetometer-only MEKF performs quite well in this scenario and the results are presented in Tables 4.9. There is a significant improvement in the attitude and angular velocity estimation accuracy compared to the tumbling scenario. Table 4.9 shows a total angular error of $\delta\alpha=0.2161\pm0.0035^\circ$ which meets the Earth-pointing estimation accuracy requirement of $\delta\alpha<0.5^\circ$. The angular velocity estimate error also meets the accuracy requirement of $\delta\omega<0.02^\circ/s$ and is sufficiently small for the attitude controller to maintain the low angular rate required in Earth-pointing mode. The estimation errors of all 100 Earth-pointing scenario simulations over the first 30 minutes are shown in Figure 4.3. In all simulations, the attitude and angular velocity estimates converge in less than 15 minutes. The performance of the magnetometer-only MEKF is further analyzed in combination with active attitude control in Chapter 5.

Table 4.9: Attitude and angular velocity estimate errors of the magnetometer-only MEKF in the Earth-pointing scenario.

Average RMS Error [°]			Average RMS Error [°/s]			
\pm Standard Deviation [$^{\circ}$]			\pm Standard Deviation [°/s]			
$\delta \psi$	$\delta heta$	$\delta\phi$	$\delta \alpha$	$\delta\omega_x$	$\delta\omega_y$	$\delta\omega_z$
0.1396	0.1021	0.1295	0.2161	0.0057	0.0054	0.0065
0.0026	0.0015	0.0033	0.0035	8e-05	7e-05	9e-05

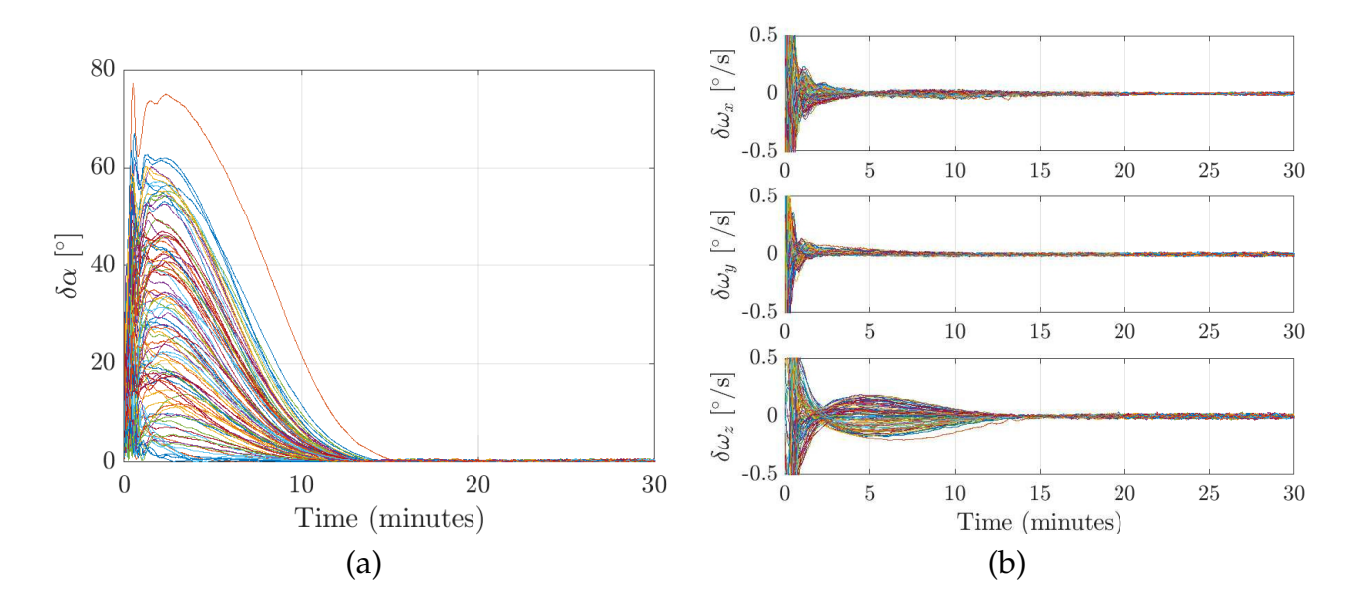


Figure 4.3: Magnetometer-only MEKF estimation errors in Earth-pointing scenario from t=0 to t=30 minutes. (a) Total angular error, (b) Angular velocity error

Chapter 5

Attitude Control

The Meteorix attitude control algorithms are formulated and compared in this chapter. First, the method for calculating the desired attitude in each operational mode and the criteria for switching between modes are outlined in Section 5.1. The PD control law developed for the EyeSat mission and applied to Meteorix in prior work is then presented in Section 5.2. A nonlinear sliding mode control law is then formulated in Section 5.3 based on the literature with a few modifications. The sliding mode controller uses full state feedback from the magnetometer-only MEKF while the PD controller only requires feedback of the rate of change of the magnetic field measurement. Simulation results are presented to compare the performance of each controller separately in the detumbling, alignment, and nominal modes in Section 5.4. In simulations of detumbling mode the PD and sliding mode controllers are also evaluated against the classical B-dot control – a current standard for cubesat missions. In Section 5.5, the robustness of the sliding mode controller is highlighted through a sensitivity study that evaluates the ADCS performance in the presence of several sources of error. The chapter concludes with a discussion on methods to further improve the magnetometer-only MEKF and sliding mode controller.

5.1 Setting the Desired Attitude

The desired rotation matrix, $C(\mathbf{q}_d)$, is calculated from the desired orientation of the body-fixed frame, $\mathcal{F}_d = \{\mathbf{x}_d, \mathbf{y}_d, \mathbf{z}_d\}$, which depends on the current operational mode as defined in Chapter 2. While the detumbling mode does not have an attitude pointing requirement, the attitude controllers still need a desired attitude to be defined. Therefore the desired attitude passed to the attitude controllers in detumbling mode is simply $C(\mathbf{q}_d) = \mathbf{1}_{3\times 3}$. As stated in Chapter 2, the alignment mode and Sun-pointing mode have the same desired body-fixed frame orientation in the inertial frame defined by:

$$\mathbf{z}_{d} = \frac{\mathbf{n}_{o}^{\times}(\mathbf{r}_{sun}^{\times}\mathbf{n}_{o})}{||\mathbf{n}_{o}^{\times}(\mathbf{r}_{sun}^{\times}\mathbf{n}_{o})||}$$
(5.1)

$$\mathbf{y}_d = \frac{\mathbf{n}_o}{||\mathbf{n}_o||} \tag{5.2}$$

$$\mathbf{x}_d = \mathbf{y}_d^{\times} \mathbf{z}_d \tag{5.3}$$

where we recall that \mathbf{n}_o is the orbit normal direction and \mathbf{r}_{sun} is the Sun direction, both expressed in the inertial frame. The desired body-fixed frame orientation in the inertial frame in Earth-pointing mode is defined by

$$\mathbf{z}_d = \frac{\mathbf{r}}{||\mathbf{r}||} \tag{5.4}$$

$$\mathbf{y}_d = \frac{\mathbf{n}_o}{||\mathbf{n}_o||} \tag{5.5}$$

$$\mathbf{x}_d = \mathbf{y}_d^{\times} \mathbf{z}_d \tag{5.6}$$

Then, the desired rotation matrix is calculated as follows:

$$\mathbf{C}(\mathbf{q}_d) = \begin{bmatrix} \mathbf{x}_d^\top \\ \mathbf{y}_d^\top \\ \mathbf{z}_d^\top \end{bmatrix}$$
 (5.7)

Recall from Chapter 2 that the angle β defines the angular error between the satellite's \mathbf{z}_b axis and the desired \mathbf{z}_d pointing direction. In addition, the angle γ defines the angular error between the satellite's \mathbf{y}_b axis and the orbit normal direction \mathbf{n}_o . Particular to the Sun-pointing orientation, $\beta = 0$ ° corresponds to the minimum Sun-pointing error of 22.5° as the satellite motion is constrained to the orbital plane, and the angle between Meteorix's orbital plane and the Sun direction is 22.5°.

The criteria for transitioning between modes are set as follows. The satellite transitions from detumbling to alignment mode once the angular rate has been reduced to $\omega < 0.3\,^{\circ}/\mathrm{s}$. The transition from alignment mode to nominal-mode occurs when either of β or γ is reduced below 5°. In the real mission, the transitions between Earth and Sun-pointing will be commanded through communication with the ground stations. In simulation, the transitions are commanded such that for each full orbit of the Earth, the satellite spends approximately 35 minutes Earth-pointing and approximately 60 minutes maneuvering and Sun-pointing.

It is important to note that in the subsequent presentation, the satellite's position, r, and velocity, v, are assumed to be perfectly known as they are used in the calculation of the desired attitude. On the real satellite, the position and velocity need to be estimated using a combination of GPS measurements and an orbital propagator. The uncertainty in these estimates is not accounted for in this thesis.

5.2 Proportional-Derivative Control

The PD control law presented here was originally developed for the EyeSat mission in [36] and applied to the Meteorix mission in [37]. The magnetic control input, \mathbf{m}_c , is calculated with:

$$\mathbf{m}_c = \frac{1}{||\mathbf{B}_d||^2} (K_P \mathbf{B}_d + K_D (\dot{\mathbf{B}}_d - \dot{\tilde{\mathbf{B}}}_m))$$
 (5.8)

where K_P and K_D are the proportional and derivative gains, respectively, and \mathbf{B}_d is the desired magnetic field vector in the body-fixed frame given by:

$$\mathbf{B}_d = \mathbf{C}(\mathbf{q}_d)\mathbf{B}_I \tag{5.9}$$

Notice that measured magnetic field, \mathbf{B}_m , is not included in the proportional part of the control law as it would disappear in the cross product that gives the resulting torque (Equation (5.11). The desired rate of change of the magnetic field, $\dot{\mathbf{B}}_d$, is calculated as a finite difference between the desired magnetic field vector at the current and previous time steps:

$$\dot{\mathbf{B}}_d = \frac{\mathbf{B}_{d|k} - \mathbf{B}_{d|k-1}}{\Delta t} \tag{5.10}$$

The magnetic field derivative, $\dot{\tilde{B}}_m$, is the filtered finite difference of the magnetometer measurement as defined in Equation (4.64). The components of the control input, m_c , are saturated between +/-0.2 Am², the limits of Meteorix's magnetorquers, and normalized to maintain the original direction of m_c . This gives the actual commanded control input, m_{act} . The magnetic control torque acting on the satellite is therefore:

$$\boldsymbol{\tau}_{mc} = \mathbf{m}_{act}^{\times} \mathbf{B}_{B} \tag{5.11}$$

The PD control law in Equation (5.8) is an extension of the classic B-dot control law. B-dot control is most commonly implemented in the following form:

$$\mathbf{m}_c = \frac{-k}{||\mathbf{B}_m||} \dot{\tilde{\mathbf{B}}}_m \tag{5.12}$$

where k is a constant scalar gain. In this work the B-dot control law is used as a baseline in the evaluation of the PD and sliding mode controller performance in detumbling mode.

5.3 Sliding Mode Control

While the PD control law does not require explicit knowledge of the satellite's attitude and angular velocity, it is unclear if it can meet the performance requirements in the presence of uncertainties and disturbances which will be present in the real system. For this reason, a nonlinear sliding mode control law is proposed. The formulation presented here is based on [41] and [45] with a few modifications.

For an arbitrary dynamic system, the basic premise of sliding mode control is to define a sliding surface, s, that depends on the states of interest of the system and design a control law to bring s to a desired value or trajectory (typically zero). For satellite attitude control, the sliding surface is commonly defined as a sum of the angular velocity error and attitude error [41]:

$$\mathbf{s} = \boldsymbol{\omega}_e + K_a \mathbf{q}_{e_n} \tag{5.13}$$

where K_q is a positive, constant gain, ω_e is the angular velocity error and \mathbf{q}_{e_v} is the vector part of the quaternion error. These are the attitude tracking errors defined by:

$$\mathbf{q}_e = \mathbf{q} \otimes \mathbf{q}_d^{-1} = [q_{e_0}, \ \mathbf{q}_{e_n}^{\top}]^{\top}$$
(5.14)

$$\boldsymbol{\omega}_e = \boldsymbol{\omega} - \mathbf{C}(\mathbf{q}_e)\boldsymbol{\omega}_d \tag{5.15}$$

where ω_d is the desired angular velocity, \mathbf{q}_d is the desired attitude quaternion, and the rotation matrix $\mathbf{C}(\mathbf{q}_e)$ brings the desired frame to the body-fixed frame. The sliding mode control input is separated into an equivalent control torque, τ_{eq} , and a reaching control torque, τ_{rh} . The total control torque, τ_c , is defined as:

$$\tau_c = \tau_{eq} + \tau_{rh} \tag{5.16}$$

The equivalent control torque is that which keeps the satellite on the sliding manifold defined by:

$$\mathbf{s} = \mathbf{0}, \ \dot{\mathbf{s}} = \mathbf{0} \tag{5.17}$$

The time rate of change of s represents the evolution of the sliding surface as a result of the satellite rotational motion. The evaluation of \dot{s} requires the definition of the attitude error dynamics, $\dot{\omega}_e$, and kinematics, \dot{q}_e . The error dynamics are defined as:

$$\dot{\boldsymbol{\omega}}_e = \dot{\boldsymbol{\omega}} - \mathbf{C}(\mathbf{q}_e)\dot{\boldsymbol{\omega}}_d - \dot{\mathbf{C}}(\mathbf{q}_e)\boldsymbol{\omega}_d \tag{5.18}$$

In the above, we use a reduced version of the satellite attitude dynamics model in which the angular momentum of the flywheel, \mathbf{H}_f , is omitted:

$$\dot{\boldsymbol{\omega}} = \mathbf{J}^{-1}(-\boldsymbol{\omega}^{\times}\mathbf{J}\boldsymbol{\omega} + \boldsymbol{\tau}_{mc}) \tag{5.19}$$

If \mathbf{H}_f were included, the resulting sliding mode control input would negate the stabilizing effect of the flywheel. The desired angular velocity is zero in all operational modes with the exception of Earth-pointing mode in which it is constant at $\boldsymbol{\omega}_d = [0, 2\pi/T, 0]^{\top} \, ^{\circ}/\mathrm{s}$. Therefore, $\dot{\boldsymbol{\omega}}_d = \mathbf{0}^{\circ}/\mathrm{s}^2$, and with the identity $\dot{\mathbf{C}}(\mathbf{q}_e) = -\boldsymbol{\omega}_e^{\times} \mathbf{C}(\mathbf{q}_e)$, the error dynamics become:

$$\dot{\boldsymbol{\omega}}_e = \mathbf{J}^{-1}(-\boldsymbol{\omega}^{\times}\mathbf{J}\boldsymbol{\omega} + \boldsymbol{\tau}_{mc}) + \boldsymbol{\omega}_e^{\times}\mathbf{C}(\mathbf{q}_e)\boldsymbol{\omega}_d$$
 (5.20)

The quaternion error kinematics are defined as:

$$\dot{\mathbf{q}}_{e_v} = \frac{1}{2} q_{e_0} \boldsymbol{\omega}_e - \frac{1}{2} \boldsymbol{\omega}_e^{\times} \mathbf{q}_{e_v}, \quad \dot{q}_{e_0} = -\frac{1}{2} \boldsymbol{\omega}_e^{\top} \mathbf{q}_{e_v}$$
 (5.21)

In this thesis, the sliding surface is modified to prevent the quaternion unwinding phenomenon where two quaternions, \mathbf{q} and $-\mathbf{q}$, represent the same orientation in space. This can cause the satellite to make unnecessarily large maneuvers to reach the desired

attitude. Therefore, we redefine the sliding surface of (5.13) as:

$$\mathbf{s} = \boldsymbol{\omega}_e + K_q \operatorname{sgn}(q_{e_0}) \mathbf{q}_{e_v} \tag{5.22}$$

where multiplication by $\operatorname{sgn}(q_{e_0})$ ensures that the satellite is driven to the desired attitude in the shortest distance. The equivalent control torque is calculated by evaluating $\dot{\mathbf{s}} = \mathbf{0}$. With $\tau_{mc} = \tau_{eq}$, the equivalent control torque is solved for as follows:

$$\dot{\mathbf{s}} = \dot{\boldsymbol{\omega}}_e + K_q \operatorname{sgn}(q_{e_0}) \dot{\mathbf{q}}_{e_v} \tag{5.23}$$

$$\mathbf{0} = \mathbf{J}^{-1}(-\boldsymbol{\omega}^{\times}(\mathbf{J}\boldsymbol{\omega}) + \boldsymbol{\tau}_{eq}) + \boldsymbol{\omega}_{e}^{\times}\mathbf{C}(\mathbf{q}_{e})\boldsymbol{\omega}_{d} + \frac{1}{2}K_{q}\operatorname{sgn}(q_{e_{0}})(q_{e_{0}}\boldsymbol{\omega}_{e} - \boldsymbol{\omega}_{e}^{\times}\mathbf{q}_{e_{v}})$$
(5.24)

$$\boldsymbol{\tau}_{eq} = \boldsymbol{\omega}^{\times} (\mathbf{J}\boldsymbol{\omega}) - \mathbf{J}(\boldsymbol{\omega}_{e}^{\times} \mathbf{C}(\mathbf{q}_{e}) \boldsymbol{\omega}_{d}) - \frac{1}{2} K_{q} \operatorname{sgn}(q_{e_{0}}) \mathbf{J}(q_{e_{0}} \boldsymbol{\omega}_{e} - \boldsymbol{\omega}_{e}^{\times} \mathbf{q}_{e_{v}})$$
(5.25)

Note that in Equation (5.23), the term resulting from the derivative of $\operatorname{sgn}(q_{e_0})$ is omitted. Its inclusion would result in an impulsive control input whenever $q_{e_0}=0$, since by definition $\frac{\mathrm{d}}{\mathrm{dt}}\operatorname{sgn}(q_{e_0})=2\delta(q_{e_0})$, where $\delta(\cdot)$ is the dirac delta function. The value of q_{e_0} is zero only when there is a 180° error between \mathbf{q} and \mathbf{q}_d ; however we do not expect the attitude error to be that large.

The purpose of the reaching control torque is to drive the sliding surface and its time rate of change to zero. The following reaching control law is used [45]:

$$\tau_{rh} = -K_s \mathbf{s} - K_{ss} \tanh(\mathbf{s}) \tag{5.26}$$

where K_s and K_{ss} are positive constant gains. In [45], sgn(s) is used instead of tanh(s). However, when s is close to zero the value of sgn(s) can switch rapidly between -1 and 1. This is known as chattering and can cause large, high frequency oscillations in the control input. Here, tanh(s) is chosen as opposed to sgn(s) as it provides a smoother control input when the sign of s changes. To summarize, the total control input is given by:

$$\boldsymbol{\tau}_{c} = \boldsymbol{\omega}^{\times}(\mathbf{J}\boldsymbol{\omega}) - \mathbf{J}(\boldsymbol{\omega}_{e}^{\times}\mathbf{C}(\mathbf{q}_{e})\boldsymbol{\omega}_{d}) - \frac{1}{2}K_{q}\operatorname{sgn}(q_{e_{0}})\mathbf{J}(q_{e_{0}}\boldsymbol{\omega}_{e} - \boldsymbol{\omega}_{e}^{\times}\mathbf{q}_{e_{v}}) - K_{s}\mathbf{s} - K_{ss}\tanh(\mathbf{s})$$
(5.27)

However, as previously stated, the control torque τ_c cannot be commanded directly to the magnetic actuators as it is constrained to be perpendicular to the magnetic field. First, the magnetic actuator dipole moment, m_c , required to produced τ_c is calculated with:

$$\mathbf{m}_c = \frac{[\mathbf{B}_B]^{\times} \boldsymbol{\tau}_c}{\|\mathbf{B}_B\|^2} \tag{5.28}$$

As was done with the PD control law, the components of \mathbf{m}_c are saturated between ± 0.2 Am² and normalized to maintain the original direction, giving \mathbf{m}_{act} . The magnetic control torque acting on the satellite is then calculated with Equation (5.11).

The sliding mode controller was implemented to use the state feedback from the magnetometeronly MEKF and thus its performance is heavily dependent on the estimation accuracy. The sliding mode control law with estimated state feedback is now defined as:

$$\boldsymbol{\tau}_{c} = \hat{\boldsymbol{\omega}}^{\times}(\mathbf{J}\hat{\boldsymbol{\omega}}) - \mathbf{J}(\hat{\boldsymbol{\omega}}_{e}^{\times}\mathbf{C}(\hat{\mathbf{q}}_{e})\boldsymbol{\omega}_{d}) - \frac{1}{2}K_{q}\operatorname{sgn}(\hat{q}_{e_{0}})\mathbf{J}(\hat{q}_{e_{0}}\hat{\boldsymbol{\omega}}_{e} - \hat{\boldsymbol{\omega}}_{e}^{\times}\hat{\mathbf{q}}_{e_{v}}) - K_{s}\hat{\mathbf{s}} - K_{ss}\tanh(\hat{\mathbf{s}})$$
(5.29)

where the attitude and angular velocity tracking errors are computed from the estimated states and the desired states with:

$$egin{aligned} \hat{oldsymbol{\omega}}_e &= \hat{oldsymbol{\omega}} - \mathbf{C}(\hat{\mathbf{q}}_e) oldsymbol{\omega}_d \ \\ \hat{\mathbf{q}}_e &= \hat{\mathbf{q}} \otimes \mathbf{q}_d^{-1} \ \\ \hat{\mathbf{s}} &= \hat{oldsymbol{\omega}}_e + K_g \hat{\mathbf{q}}_{ev} \end{aligned}$$

In addition, Equation (5.28) is modified as:

$$\mathbf{m}_c = \frac{[\hat{\mathbf{B}}_B]^{\times} \boldsymbol{\tau}_c}{\|\hat{\mathbf{B}}_B\|^2} \tag{5.30}$$

where $\hat{\mathbf{B}}_B$ is the estimated magnetic field in the body-fixed frame, calculated with $\hat{\mathbf{B}}_B = \mathbf{C}(\hat{\mathbf{q}})\mathbf{B}_I$.

Initial simulation results showed that the sliding mode controller (5.29) did not perform adequately for aligning the satellite's y_b axis with the orbit normal in the alignment mode. This was attributed to the fact that the control torque has to work against the angular momentum of the flywheel to align y_b with the orbit normal. To remedy this, the scalar control gains K_q and K_s in Equation (5.29) were replaced with a diagonal matrix of gains, defined as follows:

$$\mathbf{K}_q = K_q \operatorname{diag}\{c_{q_1}, c_{q_2}, c_{q_3}\}$$

$$\mathbf{K}_s = K_s \operatorname{diag}\{c_{s_1}, c_{s_2}, c_{s_3}\}$$

where c_{q_i} , i=1,2,3 and c_{s_i} , i=1,2,3 are the individual weights. Using matrix gains allows us to give more control authority to different components of the control input. Since the angular momentum of the flywheel is along the satellite's \mathbf{y}_b axis, more control authority can be given to the x and z components of the control input. This is done by setting the weights as $c_{q_{1,3}} > c_{q_2}$ and $c_{s_{1,3}} > c_{s_2}$. The control gain K_{ss} is kept scalar as no benefit was found to replace it with a matrix gain.

5.4 Simulations of Attitude Control

The performance of the PD and sliding mode control laws are compared in simulation of each mission mode. The PD control gains were defined as in previous work [37], while the sliding mode control gains were tuned by trial and error until adequate performance

was observed. The control parameters used for all simulations carried out in this chapter are presented in Table 5.1. The simulations are performed with attitude and angular velocity estimation by the magnetometer-only MEKF using the same parameters as in Chapter 4. The estimate errors of the magnetometer-only MEKF are initialized to small values in order to get a baseline evaluation of the sliding mode controller. The initial attitude estimate error is set to 2° in each of the yaw, pitch, and roll angles while the angular velocity estimate error is set to $0.2^{\circ}/s$ in each component. Note that the PD controller is unaffected by attitude and angular velocity estimates as the only variable fedback is the derivative of the magnetic field measurement. The dynamics, estimation, and control are all run at a timestep of $\Delta t = 1$ s in all simulations presented in this chapter unless specified otherwise.

Table 5.1: Attitude control parameters.

PD Control		B-dot Control				
$K_P = 1 \times 10^{-6}$	$K_D = 3 \times 10^{-4}$	k = 20				
Sliding Mode Control						
$K_q = 1 \times 10^{-2}$	$K_s = 5 \times 10^{-4}$	$K_{ss} = 1 \times 10^{-5}$				
Alignment mode only:						
$c_{q_1} = 2$	$c_{q_2} = 0.1$	$c_{q_3} = 2$				
$c_{s_1} = 4$	$c_{s_2} = 0.5$	$c_{s_3} = 4$				

5.4.1 Detumbling Mode

Two detumbling scenarios are simulated; one with a moderate initial tumbling rate and one with a high initial tumbling rate, as shown in Table 5.2. The satellite is simulated for 3 orbits in both scenarios without transitioning to any of the other operational modes. In detumbling mode we are only interested in the satellite's angular velocity and the mag-

netic control inputs, as there is no strict attitude pointing requirement. The satellite angular velocity and the magnetic control inputs with each controller are shown in Figures 5.1 and 5.2 for each scenario, respectively.

Table 5.2: Initial conditions for detumbling.

Detumbling scenario 1	$\omega_0 = [5, 5, 5]^{\circ}/s$ $\psi_0 = 10^{\circ} \theta_0 = 10^{\circ} \phi_0 = 10^{\circ}$
Detumbling scenario 2	$\omega_0 = [10, 10, 10]^{\circ}/s$ $\psi_0 = 10^{\circ} \theta_0 = 10^{\circ} \phi_0 = 10^{\circ}$

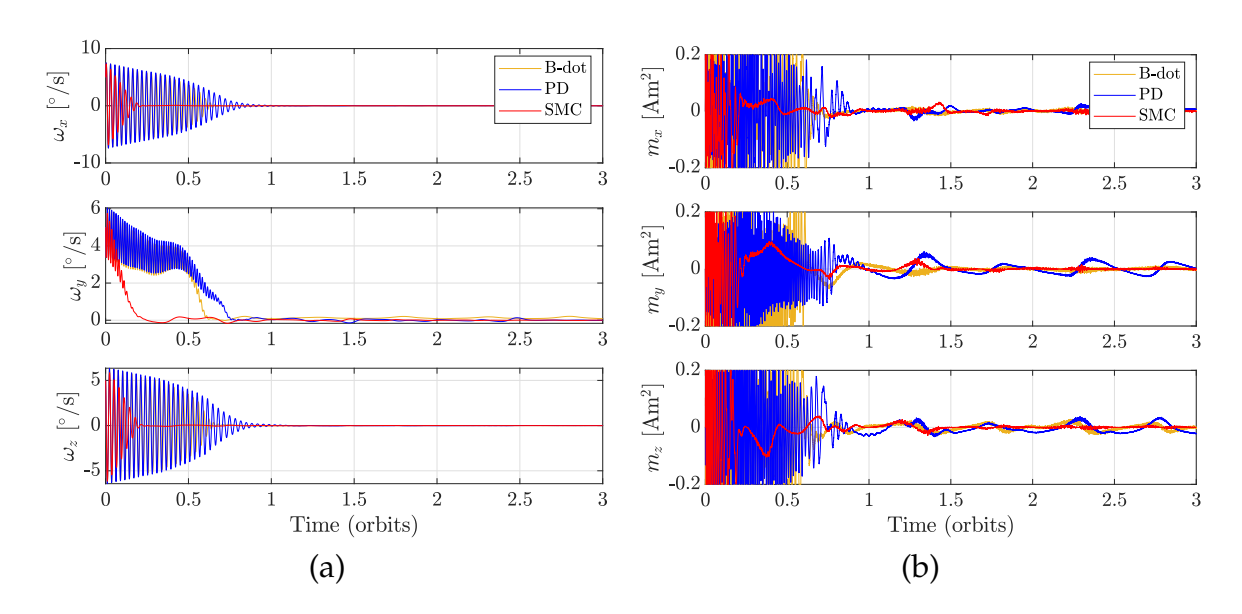


Figure 5.1: Detumbling scenario 1 results. (a) Angular velocity, (b) Magnetic control input

With a timestep of $\Delta t=1$ s, the B-dot and PD controllers fail to detumble the satellite for the high tumbling rate scenario (Figure 5.2). This is a result of the finite difference used to calculate the rate of chang of the magnetic field. The large time-step cannot capture the fast tumbling rate of the satellite. An additional simulation of scenario 2 was carried out with $\Delta t=0.1$ s with each controller and the results are shown in Figure 5.3. In this case, each controller detumbles the satellite in approximately the same amount of time. However, the sliding mode controller demonstrates superior performance both in terms

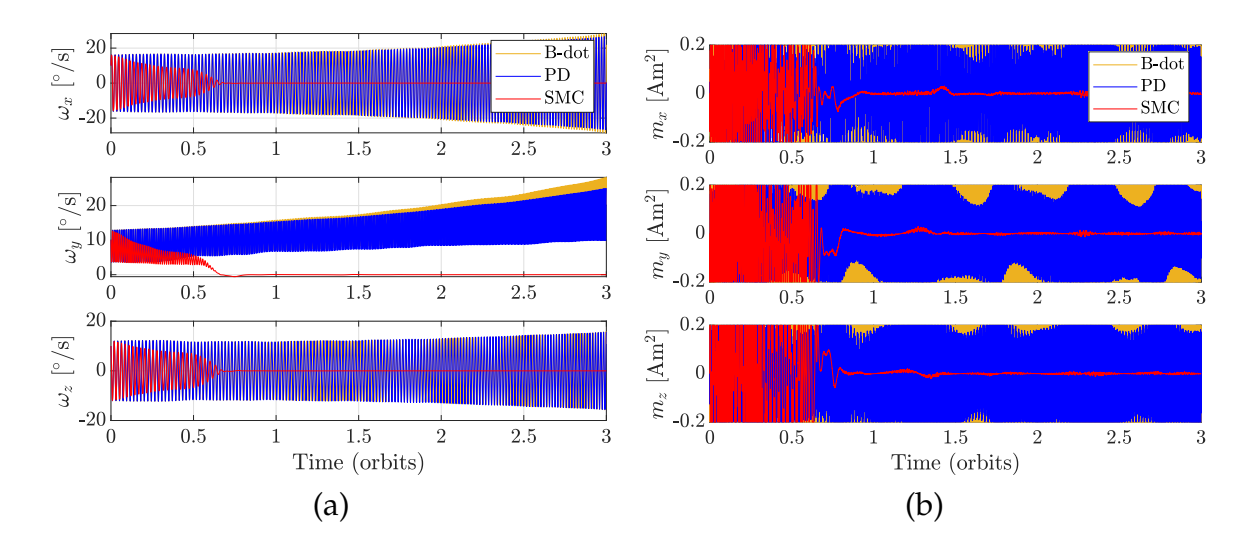


Figure 5.2: Detumbling scenario 2 results. (a) Angular velocity, (b) Magnetic control input

of control effort and residual angular rates. Figure 5.4 shows the satellite angular velocity response from t=1 orbit to t=3 orbits. The sliding mode controller maintains the angular rates low while the B-dot and PD controllers oscillate, with particularly large oscillations in ω_y up to $0.3\,^\circ$ /s. These results also indicate that the sliding mode controller is not very sensitive to the timestep.

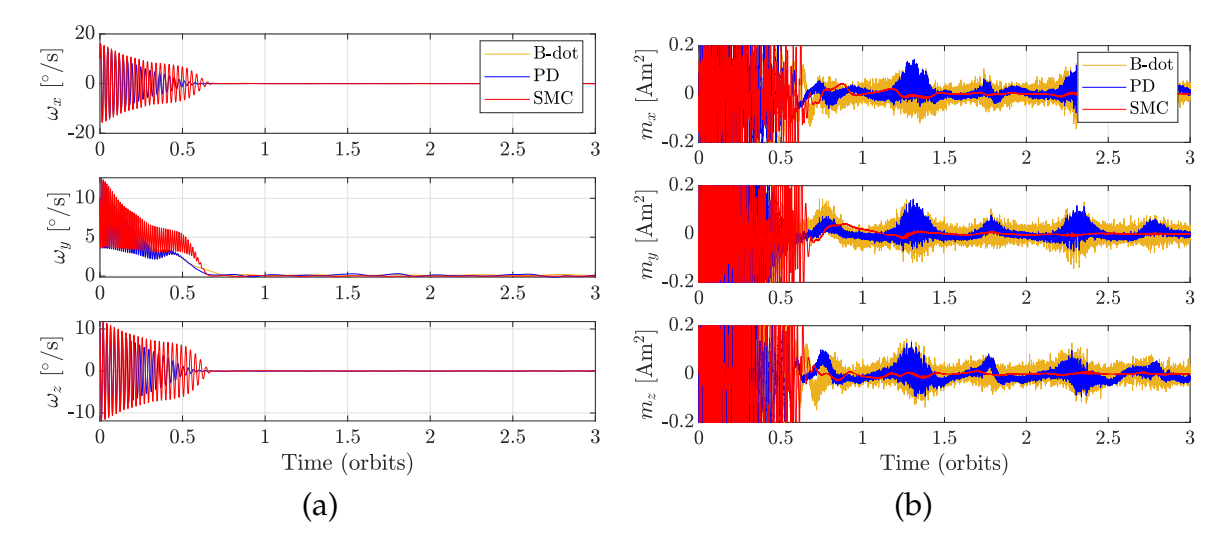


Figure 5.3: Detumbling scenario 2 with $\Delta t = 0.1$ s. (a) Angular velocity, (b) Magnetic control input

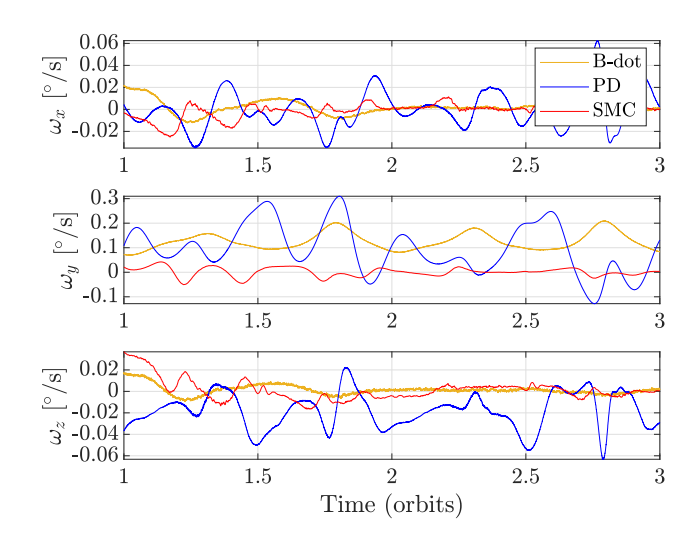


Figure 5.4: Angular velocity response after detumbling, $\Delta t = 0.1$ s.

5.4.2 Alignment Mode

For the alignment mode simulation, the initial attitude with respect to the inertial frame is the same as in Table 5.2 while the initial angular velocity is set to zero. The satellite is simulated for 3 orbits under PD and sliding mode control and does not transition to the nominal mode. Figure 5.5 shows the pointing angles γ and β , and Figure 5.6 shows the angular velocity and magnetic actuator inputs obtained with the two controllers. It is clear that the sliding mode controller achieves the desired alignment with the orbit normal and the Sun direction faster than the PD controller. However, it also uses more control effort as shown in Figure 5.6 (b). Further tuning of the PD controller was attempted, including a similar matrix gain modification as was done with the sliding mode controller, but this did not improve its performance in alignment mode.

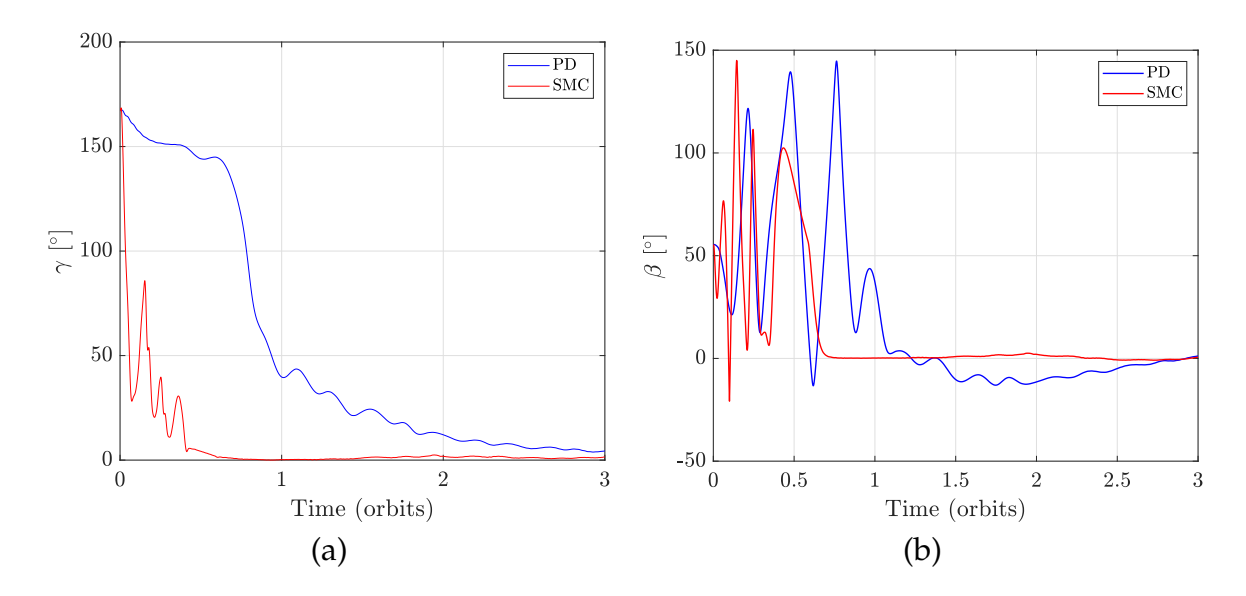


Figure 5.5: Alignment mode pointing angles. (a) y_b - n_o angle, (b) z_b - z_d angle

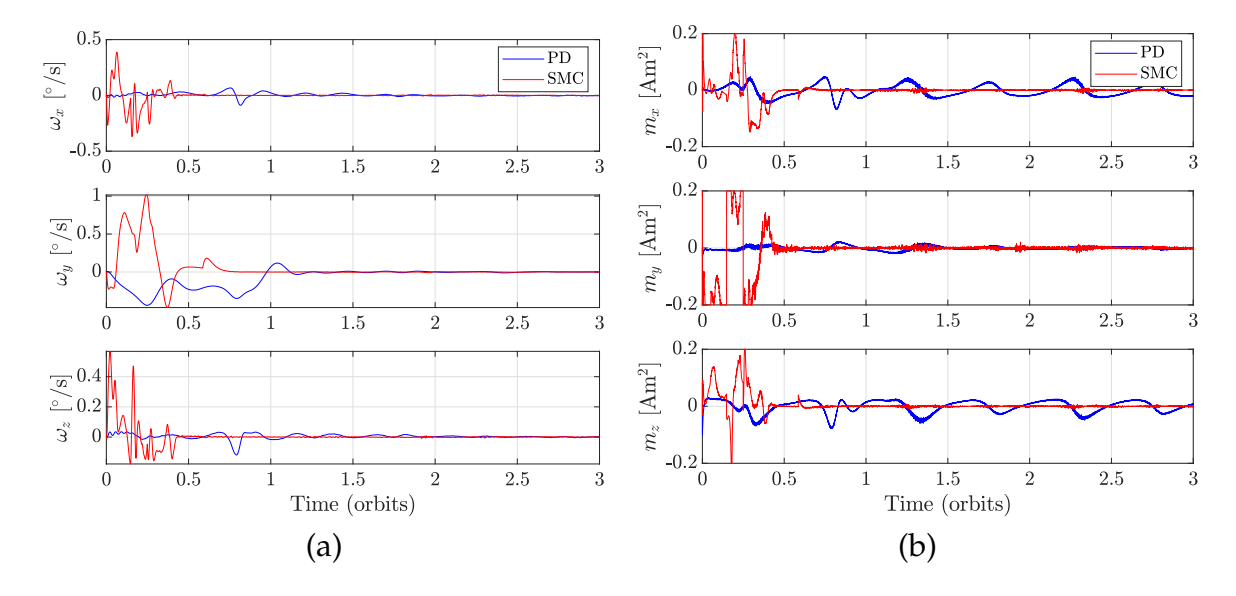


Figure 5.6: Alignment mode results. (a) Angular velocity, (b) Magnetic control input

5.4.3 Nominal Mode

A nominal mode simulation of 5 orbits is presented. Meteorix is initialized in the Earth-pointing orientation with $\beta=0^{\circ}$ and $\gamma=0^{\circ}$, and an initial angular velocity of $\omega_{0}=[0,\frac{2\pi}{T},0]^{\top}$ °/s. The pointing angles are shown in Figure 5.7 and the angular velocity and actuator inputs are shown in Figure 5.8. The transition from Earth- to Sun-pointing requires a $\approx 100^{\circ}$ reorientation and the transition from Sun-pointing to Earth-pointing

requires a $\approx 75\,^{\circ}$ reorientation, as indicated by the initial values of the red and blue lines, respectively. The PD controller completes the reorientation maneuvers slightly faster but has more overshoot. Excluding the maneuver time, the sliding mode controller results in smaller β in Earth- and Sun-pointing modes. In addition, the sliding mode controller offers better alignment with the orbit normal as shown in Figre 5.7 (b) and better angular velocity tracking as shown in Figure 5.8 (a). The x and z components of the magnetic actuator inputs demonstrate high fluctuations with the PD controller and also saturate during each transition, while they do not with the sliding mode controller.

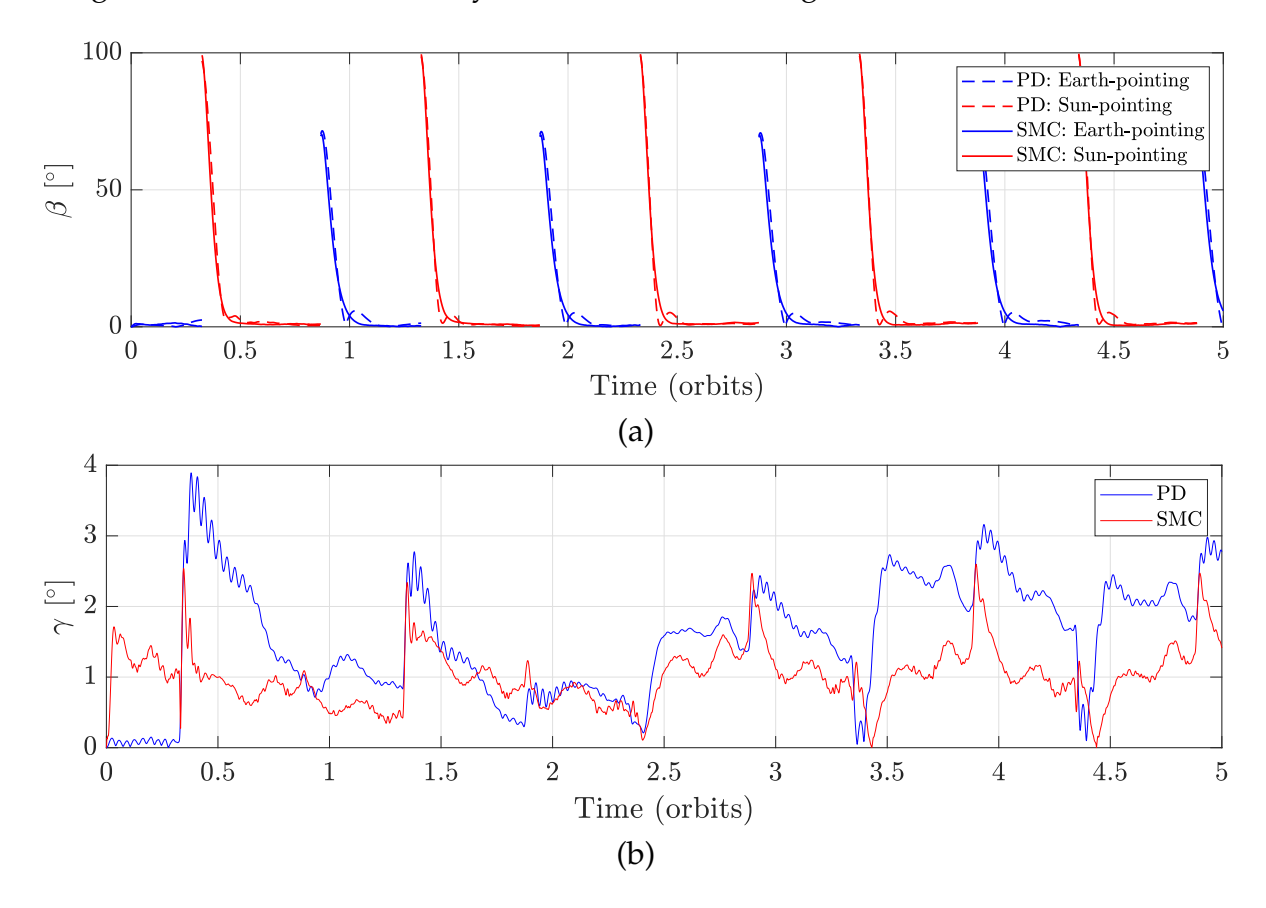


Figure 5.7: Nominal mode pointing angles. (a) \mathbf{z}_b - \mathbf{z}_d angle (b) \mathbf{y}_b - \mathbf{n}_o angle

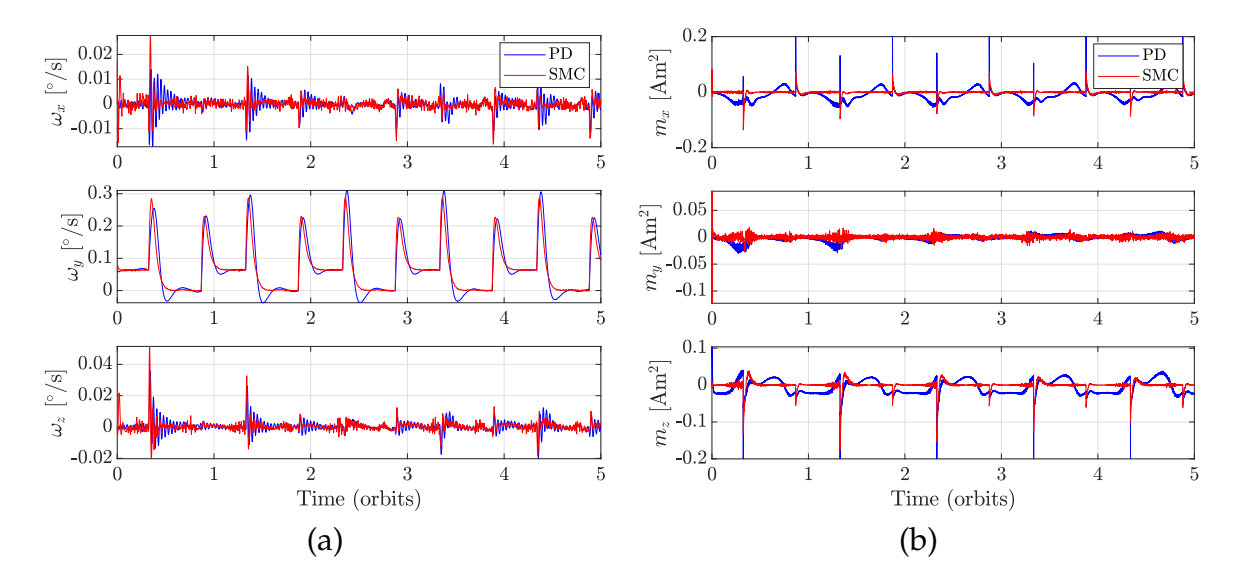


Figure 5.8: Nominal mode results. (a) Angular velocity, (b) Magnetic control input

An additional simulation of 1 day (15 orbits) is executed to capture the performance of each controller across all modes of operation. This is used as the ideal scenario to which the results of the sensitivity study in Section 5.5 are compared. Meteorix is initialized in detumbling mode with the initial conditions of detumbling scenario 1 in Table 5.2 and the same small initial estimate errors. The results from the first 5 orbits are shown in Figure 5.9 - 5.10. Figure 5.9 shows the pointing angles and Figure 5.10 shows the angular velocity and magnetic actuator inputs. The angular velocity and control input responses during the first orbit are similar to the detumbling results shown in Figure 5.1. Figure 5.10 shows the settled response after detumbling, from t = 1 orbit to t = 5 orbits. The attitude and angular velocity estimate errors over the first 5 orbits are shown in Figure 5.11. The fast detumbling and alignment time achieved with the sliding mode controller allow it to enter nominal mode much earlier than with the PD controller. In fact, the sliding mode controller enters nominal mode before the PD controller has even finished detumbling. The alignment mode starts significantly later with the PD controller as it takes almost one full orbit to detumble the satellite. The long detumbling time with the PD controller has a significant effect on the MEKF estimate errors in the first orbit, as seen in Figure 5.11. However, once detumbling has completed, the estimate errors are very similar with both

controllers as shown in Figure 5.12.

Overall, the attitude control and estimation requirements are satisfied in the ideal scenario. After the first 5 orbits, the PD and sliding mode controllers maintain average orbit normal alignment angles of $\gamma=1.59\,^\circ$ and $\gamma=0.97\,^\circ$, respectively. These are within the $\gamma<2\,^\circ$ requirement. In the nominal mode, the sliding mode controller achieves an average Sun-pointing angle of $\beta=0.50\,^\circ$ and average Earth-pointing angle of $\beta=1.78\,^\circ$ after the transitions between each orientation have completed. With the PD controller, the average Sun- and Earth-pointing angles are $\beta=1.84\,^\circ$ and $\beta=2.61\,^\circ$, respectively. The Sun-pointing angle with the PD controller does not quite meet the requirement of $\beta<1\,^\circ$. The average total angular error of the magnetometer-only MEKF after the first 5 orbits is $\delta\alpha=0.22\,^\circ$ with PD controller and $\delta\alpha=0.23\,^\circ$ with the sliding mode controller. With both controllers, the average angular velocity estimate error is $\delta\omega=0.008\,^\circ/s$. These estimation errors are within the nominal mode requirements of $\delta\alpha<0.5\,^\circ$ and $\delta\omega<0.02\,^\circ/s$.

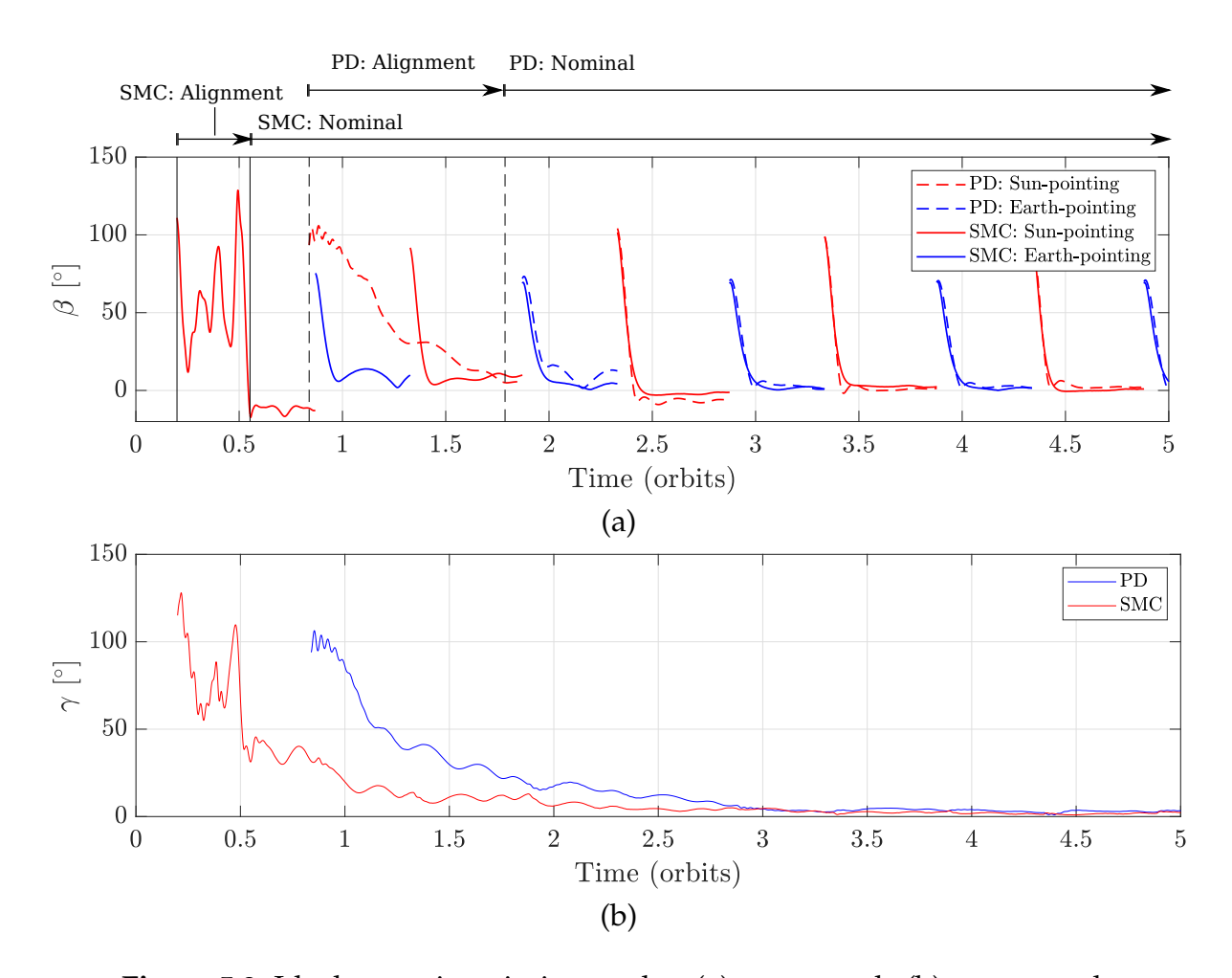


Figure 5.9: Ideal scenario pointing angles. (a) \mathbf{z}_b - \mathbf{z}_d angle (b) \mathbf{y}_b - \mathbf{n}_o angle

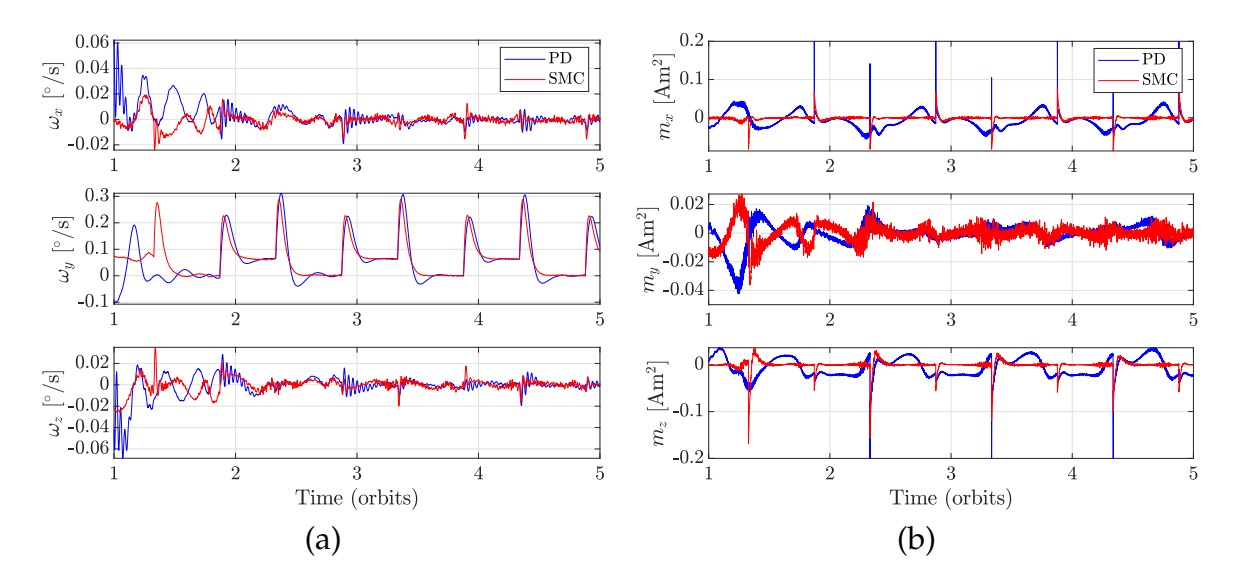


Figure 5.10: Ideal scenario ngular velocity and control inputs, from t=1 t to t=5 orbits. (a) Angular velocity, (b) Magnetic control input

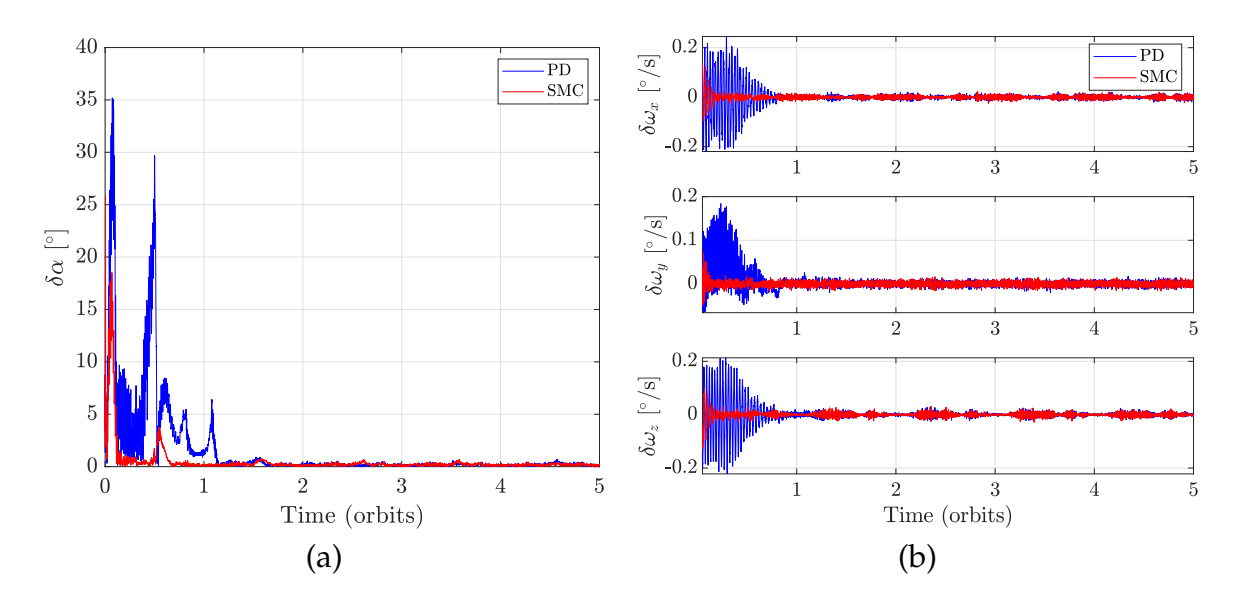


Figure 5.11: Estimate errors in ideal scenario. (a) Total angular error, (b) Angular velocity errors

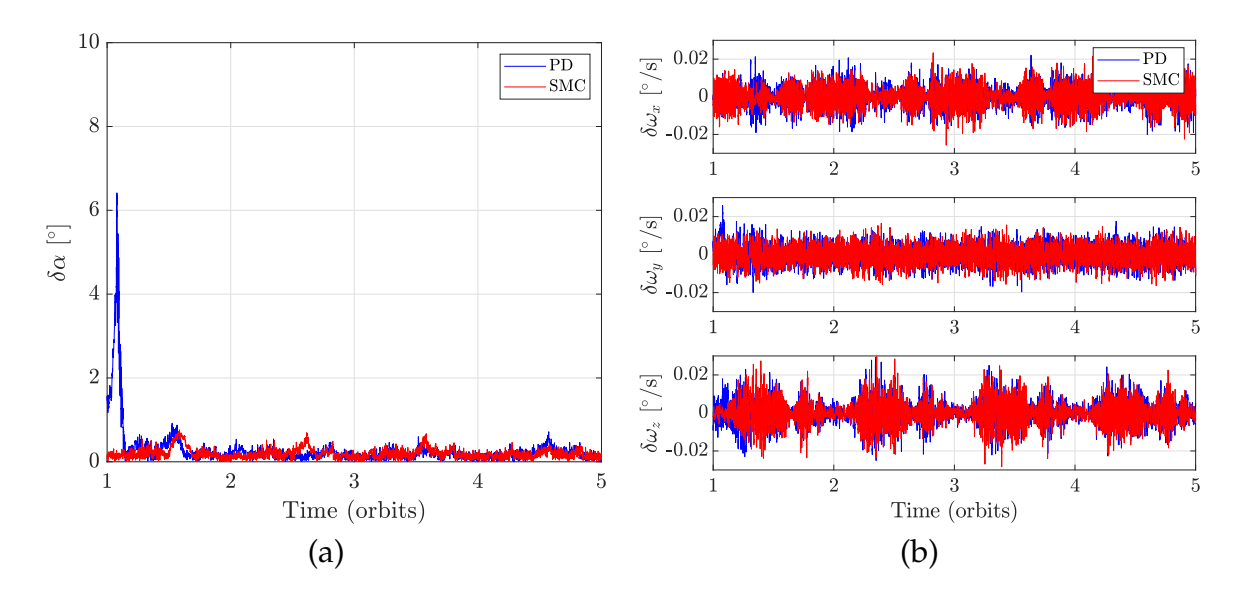


Figure 5.12: Estimate errors in ideal scenario from t=1 to t=5 orbits. (a) Total angular error, (b) Angular velocity errors

5.5 Sensitivity Study

Many possible sources of error exist for the control of the real satellite that will affect the overall ADCS performance. In this thesis, four sources of error are considered: (i) large initial estimate errors, (ii) uncertainty in the principal moments of inertia, (iii) misalignment of the flywheel axis, and (iv) residual magnetic moment. It is important to investigate the effect of these sources of error and uncertainties on the ADCS. The effect of each source of error is first tested indivually in simulations of 5 orbits with each controller, encapsulating all modes of operation with the initial conditions as given in Table 5.3 and also used in the ideal scenario in Section 5.4.3. A worst case scenario is then studied with a 1 day simulation (15 orbits) in which all of the above sources of error are present, and results are compared to the ideal scenario.

Table 5.3: Initial conditions for sensitivity study.

Satellite state	$\omega_0 = [5, 5, 5] ^{\circ}/s$ $\psi_0 = 10 ^{\circ}, \theta_0 = 10 ^{\circ}, \phi_0 = 10 ^{\circ}$
Estimate errors	$\delta \boldsymbol{\omega}_0 = [0.2, \ 0.2, \ 0.2] ^{\circ}/\mathrm{s}$ $\delta \psi_0 = 2 ^{\circ}, \delta \theta_0 = 2 ^{\circ}, \delta \phi_0 = 2 ^{\circ}$

5.5.1 Large Initial Estimate Errors

Large initial estimate errors can affect both the estimator and controller performance, particularly the sliding mode controller as it requires full state feedback from the MEKF. The estimate errors are initialized to $\delta\psi_0=\delta\theta_0=\delta\phi_0=20\,^\circ$ in attitude and $\delta\omega_0=[2,\ 2,\ 2]\,^\circ$ /s in angular velocity. It was found that these large initial estimate errors resulted in a slighlty longer detumbling time than in the ideal scenario, but the effect on alignment and nominal modes was negligible once the estimates had converged. Thus, the results look very similar to those presented in Figures 5.9 to 5.12. This is in agreement with the

results from Chapter 4, as we saw in the Monte Carlo simulations that the MEKF was able to converge in less than 20 minutes from large initial estimate errors up to 30° .

5.5.2 Inertia Uncertainty

The satellite's inertia properties will be estimated prior to launch, however, there will likely be uncertainty in these estimates. Uncertainties in the principal moments of inertia affect the attitude estimation accuracy as the magnetometer-only MEKF uses the attitude dynamics model to propagate the state estimates. The sliding mode controller is also affected as the error attitude dynamics are used in the calculation of the equivalent control torque. While the PD controller does not explicitly use the satellite's inertia to calculate the control input, the chosen PD gains may not provide the same performance as they are tuned for the particular values of the satellite's inertia.

Relative errors of +10% in each of J_{xx} , J_{yy} , and J_{zz} are considered. That is, the true principal moments of inertia used in the propagation of the attitude dynamics are 10% larger than the ones assumed by the MEKF and controllers. The pointing angles are shown in Figure 5.13, the angular velocity and control inputs are shown in Figure 5.14, and the MEKF estimate errors from t=1 to t=5 orbits are shown in Figure 5.15. Both controllers take slightly longer to detumble and align the satellite, which is expected given that the inertia is higher than what was assumed in the controller design. It takes longer for the sliding mode controller to achieve good alignment with the orbit normal, as seen in Figure 5.13 (b), compared to the ideal scenario in Figure 5.9 (b). Nonetheless, the pointing angles are small in the Earth- and Sun- pointing modes after the transitions. The MEKF showed very similar response in the first orbit to the ideal scenario. In addition, we can see in Figure 5.15 that the estimate errors from t=1 to t=5 orbits are similar to those in Figure 5.12 from the ideal scenario simulation.

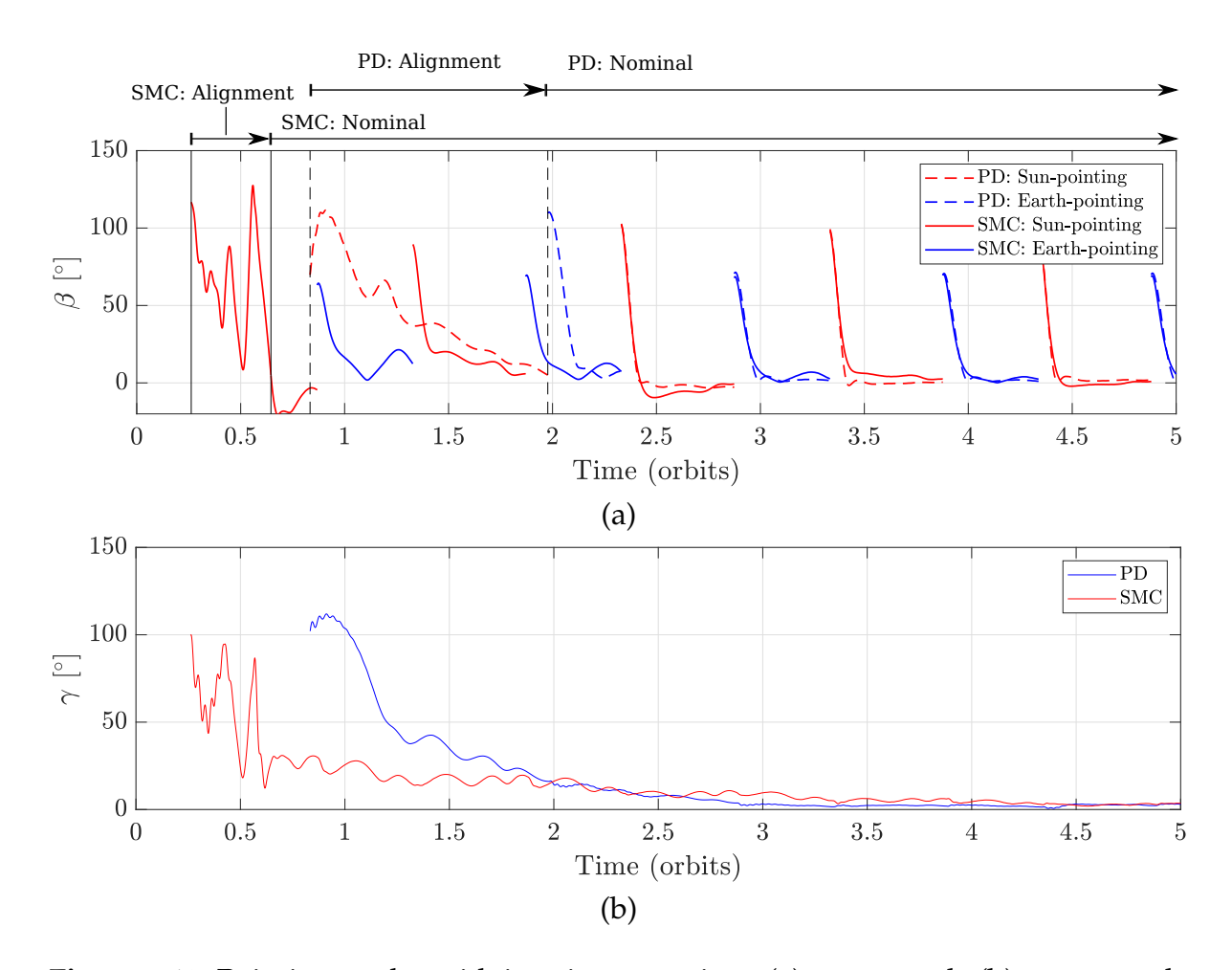


Figure 5.13: Pointing angles with inertia uncertainty. (a) \mathbf{z}_b - \mathbf{z}_d angle (b) \mathbf{y}_b - \mathbf{n}_o angle

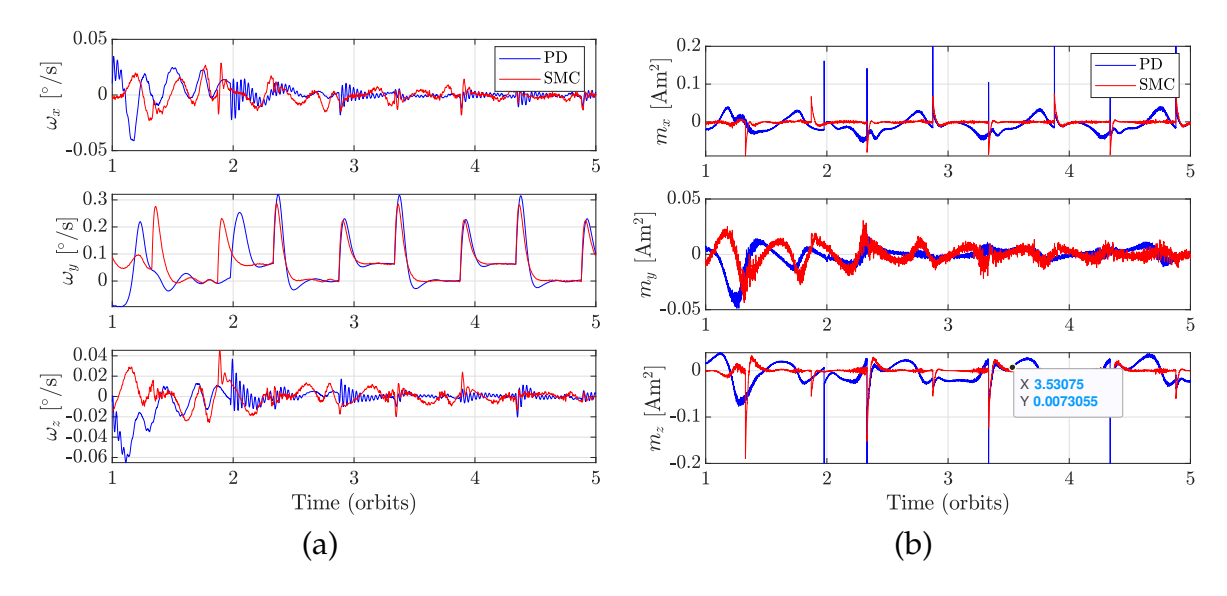


Figure 5.14: Angular velocity and control inputs with inertia uncertainty, from t=1 t to t=5 orbits. (a) Angular velocity, (b) magnetic control inputs

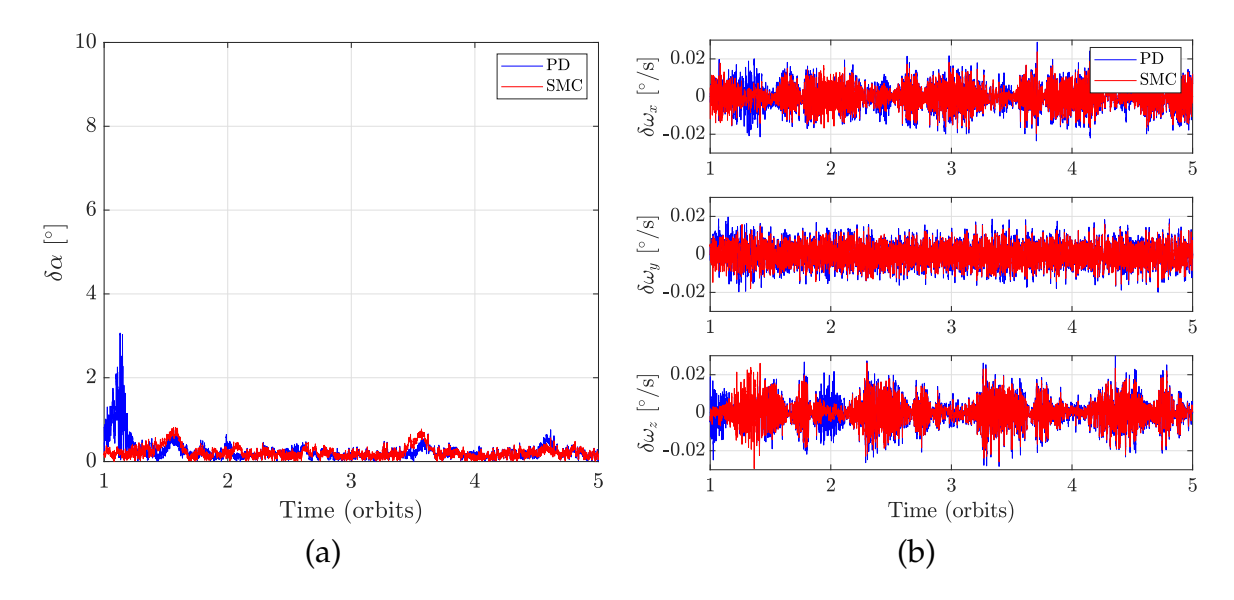


Figure 5.15: Estimate errors with inertia uncertainty, from t=1 to t=5 orbits. (a) Total angular error, (b) Angular velocity error

5.5.3 Flywheel Axis Misalignment

The magnetometer-only MEKF, sliding mode controller, and PD controller are all affected by misalignment of the flywheel axis as it affects the actual attitude dynamics of the system. The effect of the flywheel axis misalignment on the attitude dynamics is calculated with:

$$\mathbf{H}_f = \mathbf{C}_b^f \mathbf{h} \tag{5.31}$$

where h is the flywheel angular momentum in the flywheel frame ($\mathbf{h} = [0, h, 0]^{\top}$). The rotation matrix, \mathbf{C}_b^f , rotates components in the flyhweel frame to those in the body fixed frame and is defined as:

$$\mathbf{C}_{b}^{f} = \begin{bmatrix} \cos(\psi_{f}) & -\sin(\psi_{f})\cos(\phi_{f}) & \sin(\psi_{f})\sin(\phi_{f}) \\ \sin(\psi_{f}) & \cos(\psi_{f})\cos(\phi_{f}) & -\cos(\psi_{f})\sin(\phi_{f}) \\ 0 & \sin(\phi_{f}) & \cos(\phi_{f}) \end{bmatrix}$$
(5.32)

Here, the misalignment of the flywheel axis is parameterized by two angles, ψ_f and ϕ_f . The angle ψ_f represents a rotation of the flywheel axis around the satellite's \mathbf{z}_b axis and ϕ_f represents a rotation of the flywheel axis around the satellite's \mathbf{x}_b axis. The largest misalignment on either axis is expected to be 2 °, which allows for the use of the small angle approximation for \mathbf{C}_b^f :

$$\mathbf{C}_b^f = \begin{bmatrix} 1 & -\psi_f & 0 \\ \psi_f & 1 & -\phi_f \\ 0 & \phi_f & 1 \end{bmatrix} \tag{5.33}$$

Note that this uncertainty is introduced into the D-SPOSE attitude dyamics propagation model, and not in the models used by the MEKF or the sliding mode controller. For the results presented here, the flywheel misalignment is set to $\psi_f = 2^{\circ}$ and $\phi_f = 2^{\circ}$. As before, the satellite is simulated for 5 orbits with each controller, starting with the detumbling mode. Figure 5.16 shows the pointing angles and Figure 5.17 shows the satellite

angular velocity and magnetic control inputs. Figure 5.18 shows the MEKF estimate errors from t=1 to t=5 orbits. The PD and sliding mode controller still perform quite well. However, the estimation accuracy of the magneometer-only MEKF is significantly compromised with total angular errors of several degrees persisting after the detumbling mode is completed. In Figure 5.18 (a), the total angular error follows a similar profile as the y component of the satellite's angular velocity in Figure 5.17 (b). This is expected, as the flywheel misalignment causes the x and z components of its angular momentum in the body-fixed frame to become non-zero, while the MEKF attitude dynamics model assumes the flywheel is perfectly aligned.

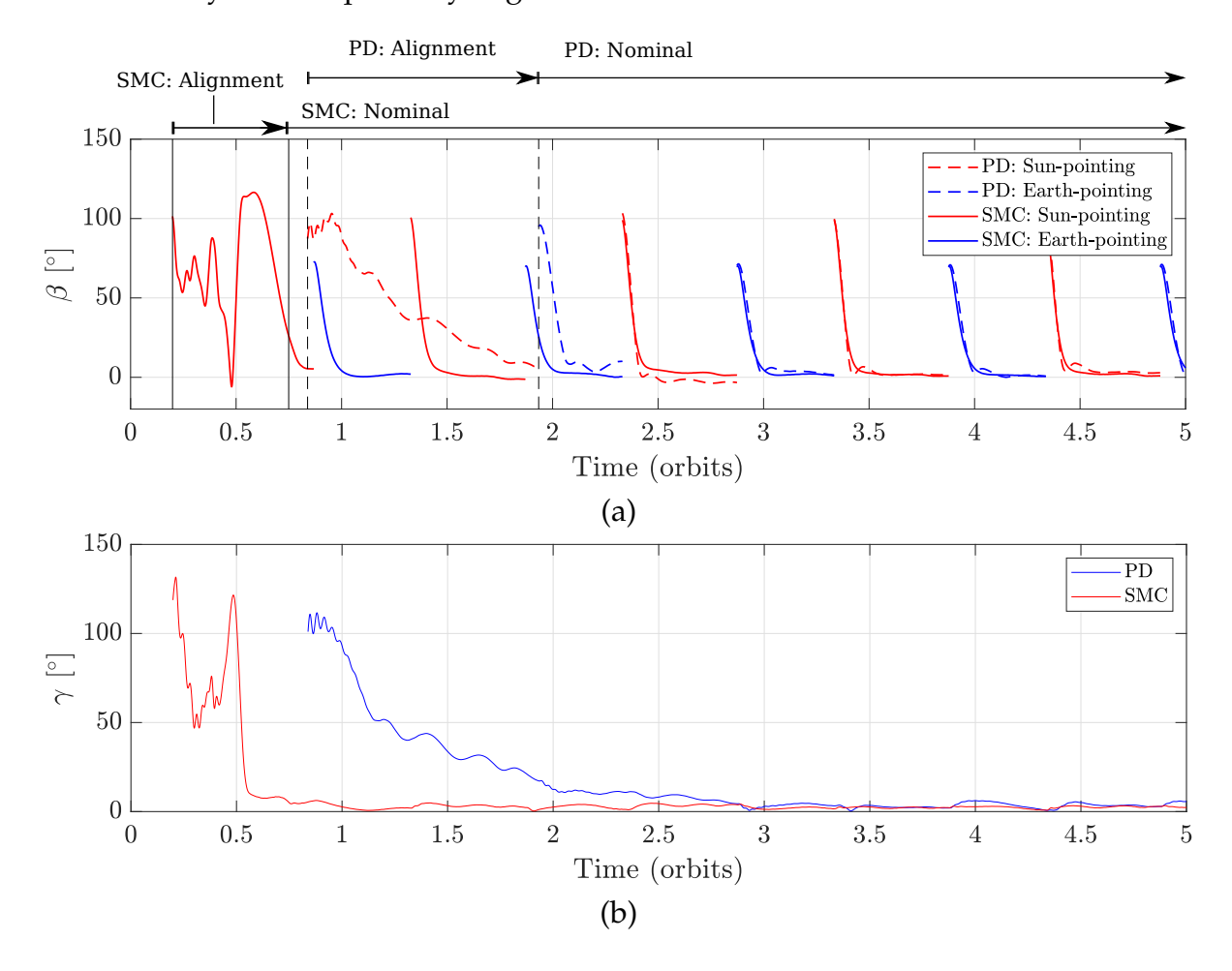


Figure 5.16: Pointing angles with flywheel misalignment. (a) \mathbf{z}_b - \mathbf{z}_d angle (b) \mathbf{y}_b - \mathbf{n}_o angle

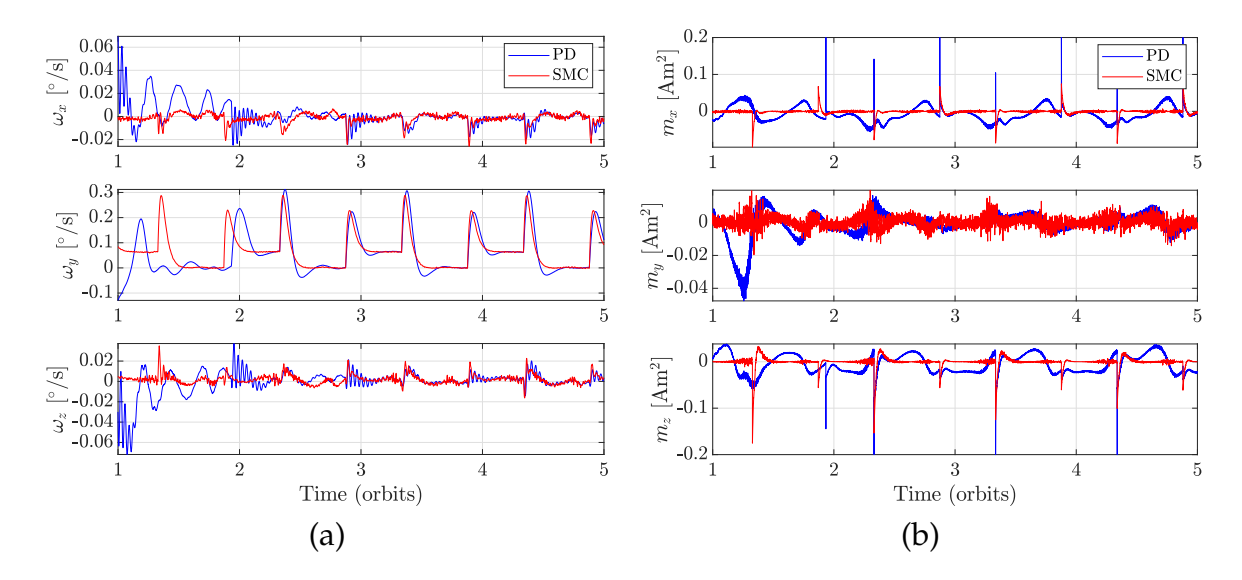


Figure 5.17: Angular velocity and control inputs with flywheel misalignment, from t = 1 t to t = 5 orbits. (a) Angular velocity, (b) magnetic control inputs

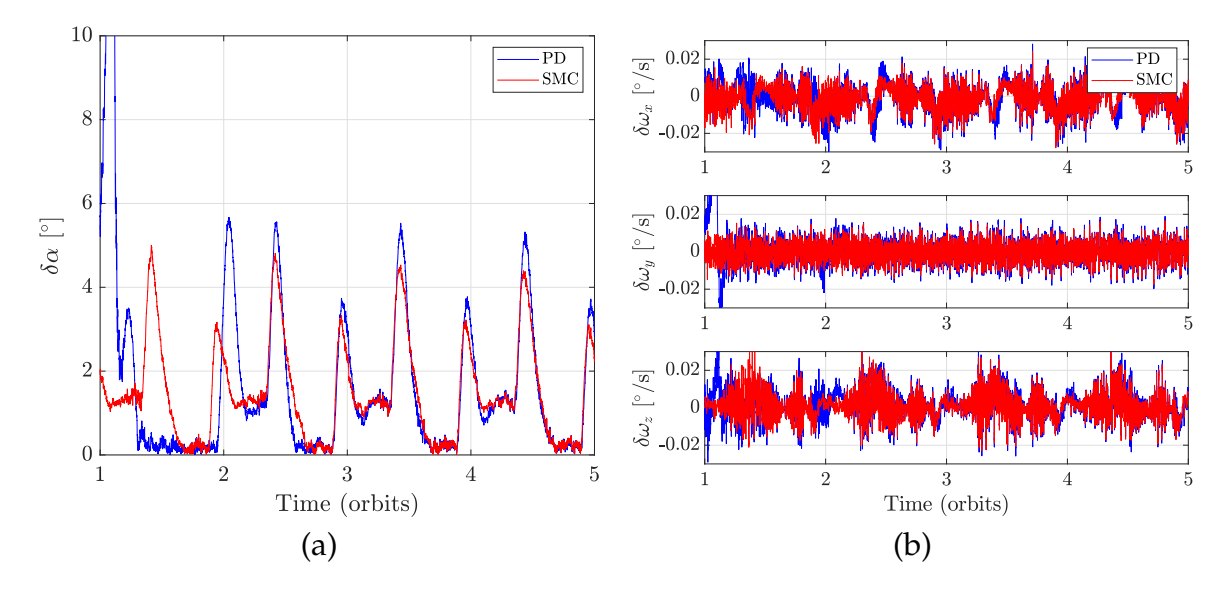


Figure 5.18: Estimate errors with flywheel misalignment, from t=1 to t=5 orbits. (a) Total angular error, (b) Angular velocity error

5.5.4 Residual Magnetic Moment

As stated in Chapter 3, the residual magnetic moment interacts with the Earth's magnetic field and produces a perturbing torque on the satellite. This affects the attitude dynamics, estimation, and control. While the residual magnetic moment can be measured before launch, errors will undoubtedly be present in this measurement. Figure 5.19 - Figure

5.20 show the effect of a residual magnetic moment of $\mathbf{m}_r = [0.01, 0.01, 0.01]^{\mathsf{T}} \, \mathrm{Am}^2$ on the PD and sliding mode controllers over 5 orbits, starting in detumbling mode. These values of m_r are comparable to measured residual magnetic moments of other 3U cubesats. For example, the Space Dart 3U cubesat had a residual magnetic moment strength of 0.009 Am² [63]. Figure 5.21 shows the attitude estimate errors of the magnetometeronly MEKF from t=1 to t=5 orbits. The major differences are seen in the nominal mode pointing angles and in the estimation errors. The performance of the PD controller is dramatically worse in this case, with the pointing angle β reaching almost 50° in Earthpointing mode and showing large fluctuations in Sun-pointing mode. This clearly does not meet the pointing requirement, recalling that the camera has a 20° field of view. In contrast, the sliding mode controller performs relatively well and shows robustness to the residual magnetic moment, with pointing angles $\beta < 10^{\circ}$ in Earth-pointing mode and $\beta < 5^{\circ}$ in Sun-pointing mode, after the transitions are completed. The accuracy of the magnetometer-only MEKF is significantly affected by the residual magnetic moment. The total angular error $\delta\alpha$ oscillates between 2 and 8°, and the oscillations are slightly larger with the PD controller. There is also a clear oscillation between ± 0.02 °/s in the y component of the angular velocity estimate error as seen in Figure 5.21 (b).

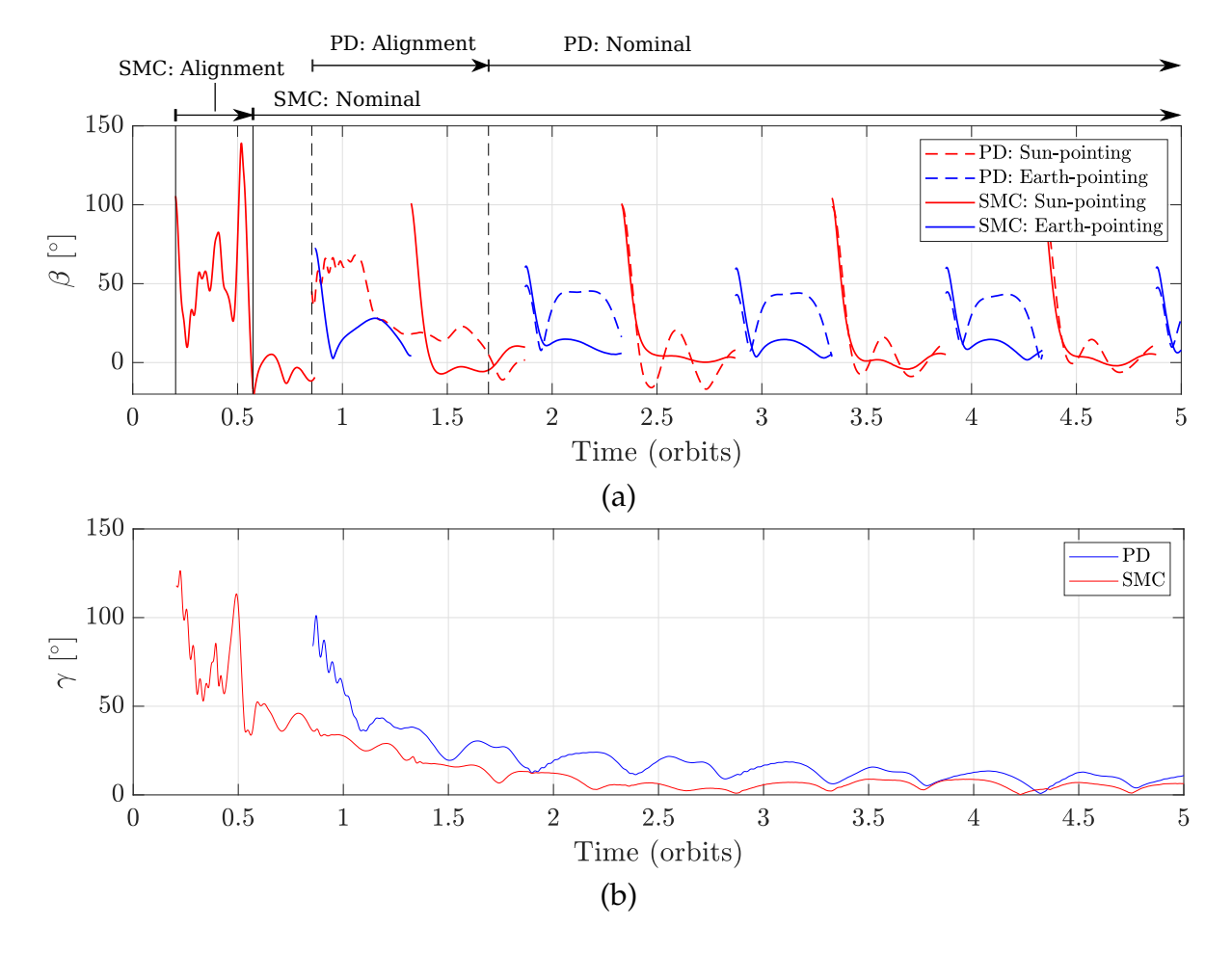


Figure 5.19: Pointing angles with residual magnetic moment. (a) \mathbf{z}_b - \mathbf{z}_d angle (b) \mathbf{y}_b - \mathbf{n}_o angle

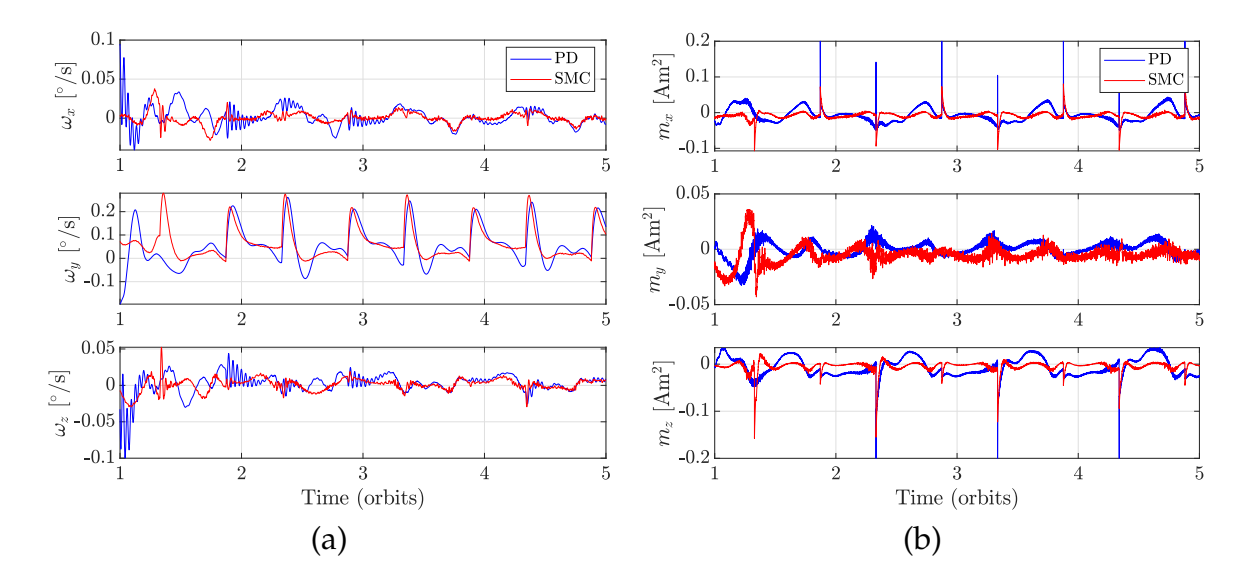


Figure 5.20: Angular velocity and control inputs with residual magnetic moment, from t = 1 t to t = 5 orbits. (a) Angular velocity, (b) magnetic control inputs

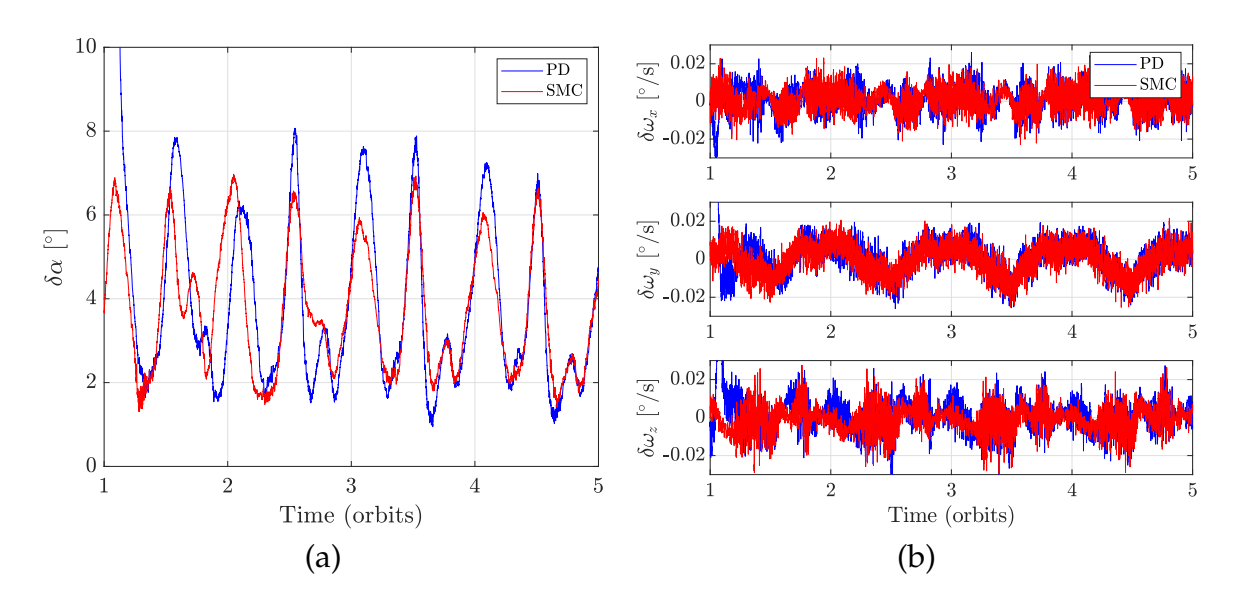


Figure 5.21: Estimate errors with residual magnetic moment, from t=1 t to t=5 orbits. (a) Total angular error, (b) Angular velocity errors

5.5.5 All Uncertainties Combined

The ADCS is tested in a worst case scenario including all sources of error as shown in Table 5.4. Meteorix is simulated for 1 day (15 orbits) starting in detumbling mode. The results are compared to the ideal scenario which was presented at the end of Section 5.4.3 and are summarized in Table 5.5. The time to detumble, $T_{detumble}$ is measured starting from t=0 to the time at which $\omega<0.3\,^\circ/\mathrm{s}$. The alignment time, T_{align} , is measured starting at the beginning of alignment mode to the time at which either $\gamma<5\,^\circ$ or $\beta<5\,^\circ$. The average orbit normal alignment angle, γ , is calculated starting from t=5 orbits. The average pointing angles in Sun-pointing, β_{SP} , and Earth-pointing, β_{EP} , are calculated starting 10 minutes after the initial transition to each mode, respectively, to allow time for maneuvering. The average attitude and angular velocity estimation errors, $\delta\alpha$ and $\delta\omega$, are also calculated starting from t=5 orbits.

In the ideal scenario, the sliding mode controller outperforms the PD controller in all operational modes and the attitude control and estimation requirements are met. The detumbling time with sliding mode control is more than 4 times faster than with PD control and the alignment time just less than 3 times faster. The sliding mode controller achieves an average pointing angle of $\beta_{SP}=0.5\,^{\circ}$ in Sun-pointing mode which is within the $\beta<1\,^{\circ}$ requirement. In addition, the average orbit normal alignment angle is well within the requirement of $\gamma<2\,^{\circ}$. The MEKF estimation errors are within the requirements of $\delta\alpha<0.5\,^{\circ}$ and $\delta\omega<0.02\,^{\circ}$ /s with both the PD and sliding mode controllers.

The worst case scenario results highlight the overall sensitivity of the ADCS to the sources of error considered. Figure 5.22 and 5.23 show the pointing angles and estimation errors with the PD controller in the ideal and worst case scenarios. Similarly, Figure 5.24 and 5.25 show compare the results with the sliding mode controller between the ideal and worst case scenarios. Interestingly, the PD controller has a longer detumbling time in the worst cases scenario than in the ideal scenario, but a shorter alignment time. However in

Figure 5.22 we can see that although β reaches the $<5\,^\circ$ mark earlier in the worst case, as indicated by the vertical solid line, the subesequent Earth-pointing angle is very poor. The sliding mode controller still meets the Earth-pointing requriement of $\beta < 20\,^\circ$ but does not meet the orbit normal alignment requirement of $\gamma < 2\,^\circ$ nor the Sun-pointing requirement of $\beta < 1\,^\circ$. However, γ and β_{SP} are significantly smaller with sliding mode control than with PD control. The total angular error of the MEKF does not meet the requirement of $\delta\alpha < 0.5\,^\circ$, with average errors of $\delta\alpha = 3.83\,^\circ$ with PD control and $\delta\alpha = 3.02\,^\circ$ with sliding mode control.

Table 5.4: Sources of error in worst case senario.

Initial estimate errors	$\delta \omega_0 = [2, 2, 2]^{\circ}/s$ $\delta \psi_0 = 20^{\circ} \delta \theta_0 = 20^{\circ} \delta \phi_0 = 20^{\circ}$		
Inertia uncertainty	+10% in J_{xx} , J_{yy} , J_{zz}		
Flywheel misalignment	$\psi_f=2^\circ$, $\phi_f=2^\circ$		
Residual magnetic moment	$\mathbf{m}_r = [0.01, \ 0.01, \ 0.01]^{\top} \ \mathbf{Am}^2$		

Table 5.5: Averaged ADCS performance results of 1 day simulations.

	Ideal Scenario		Worst Case Scenario	
	PD	SMC	PD	SMC
$T_{detumble}$ [min]	79.4	18.8	87.0	24.5
T_{align} [min]	89.7	33.5	77.8	43.9
Average γ [°]	1.59	0.97	11.06	5.20
Average β_{SP} [°]	1.84	0.50	6.18	3.31
Average β_{EP} [°]	2.61	1.78	34.67	11.41
Average $\delta \alpha$ [°]	0.22	0.23	3.83	3.02
Average $\delta\omega$ [°/s]	0.008	0.008	0.011	0.010

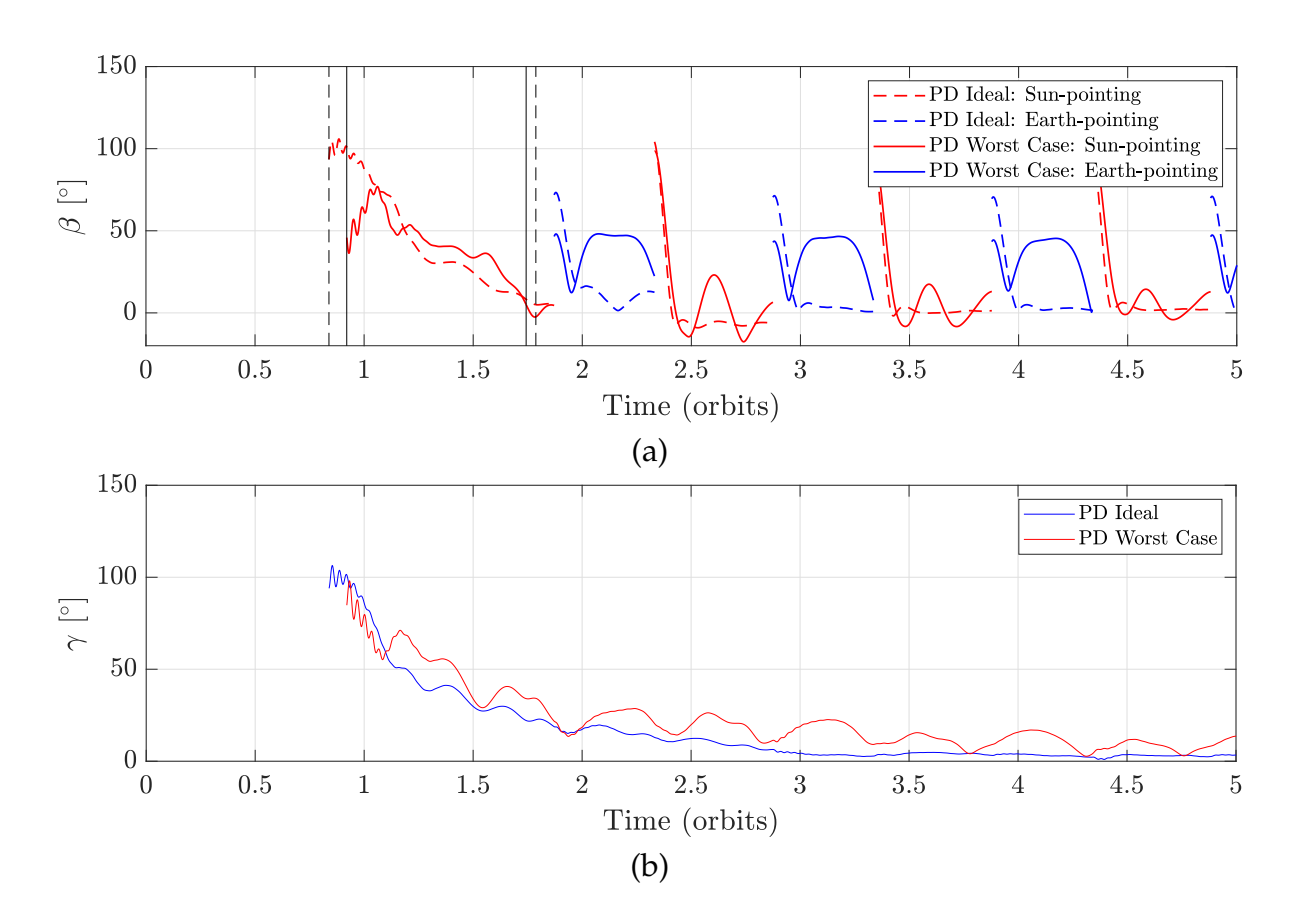


Figure 5.22: Pointing angles with PD control, ideal vs worst case scenario. (a) \mathbf{z}_b - \mathbf{z}_d angle (b) \mathbf{y}_b - \mathbf{n}_o angle

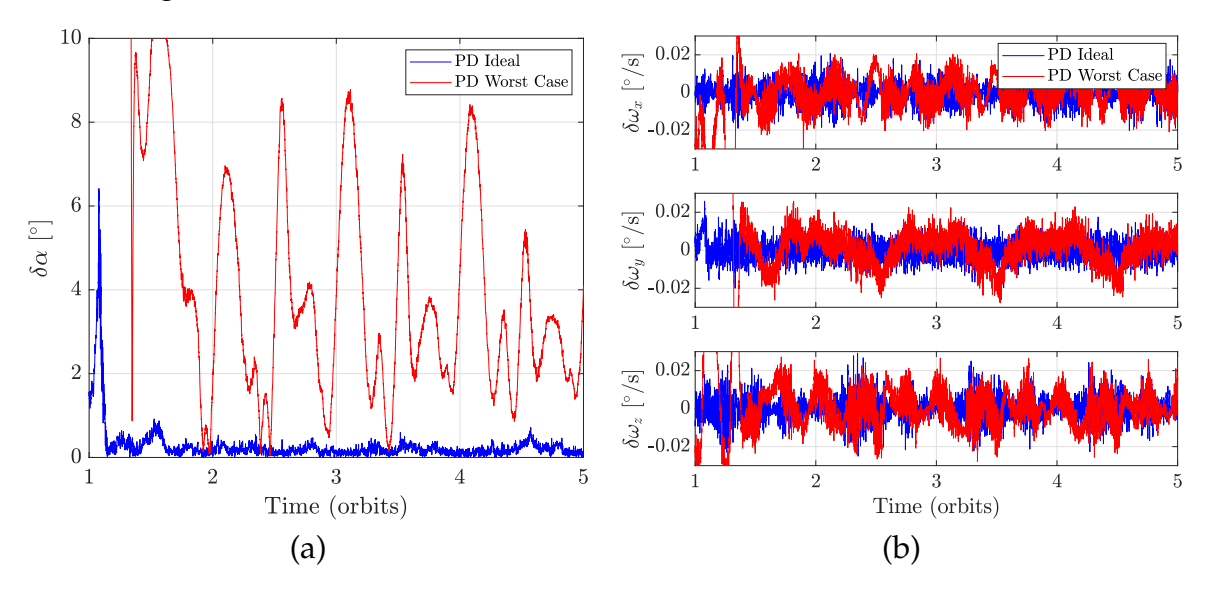


Figure 5.23: Estimate errors with PD control, ideal vs worst case scenario. (a) Total angular error, (b) Angular velocity errors

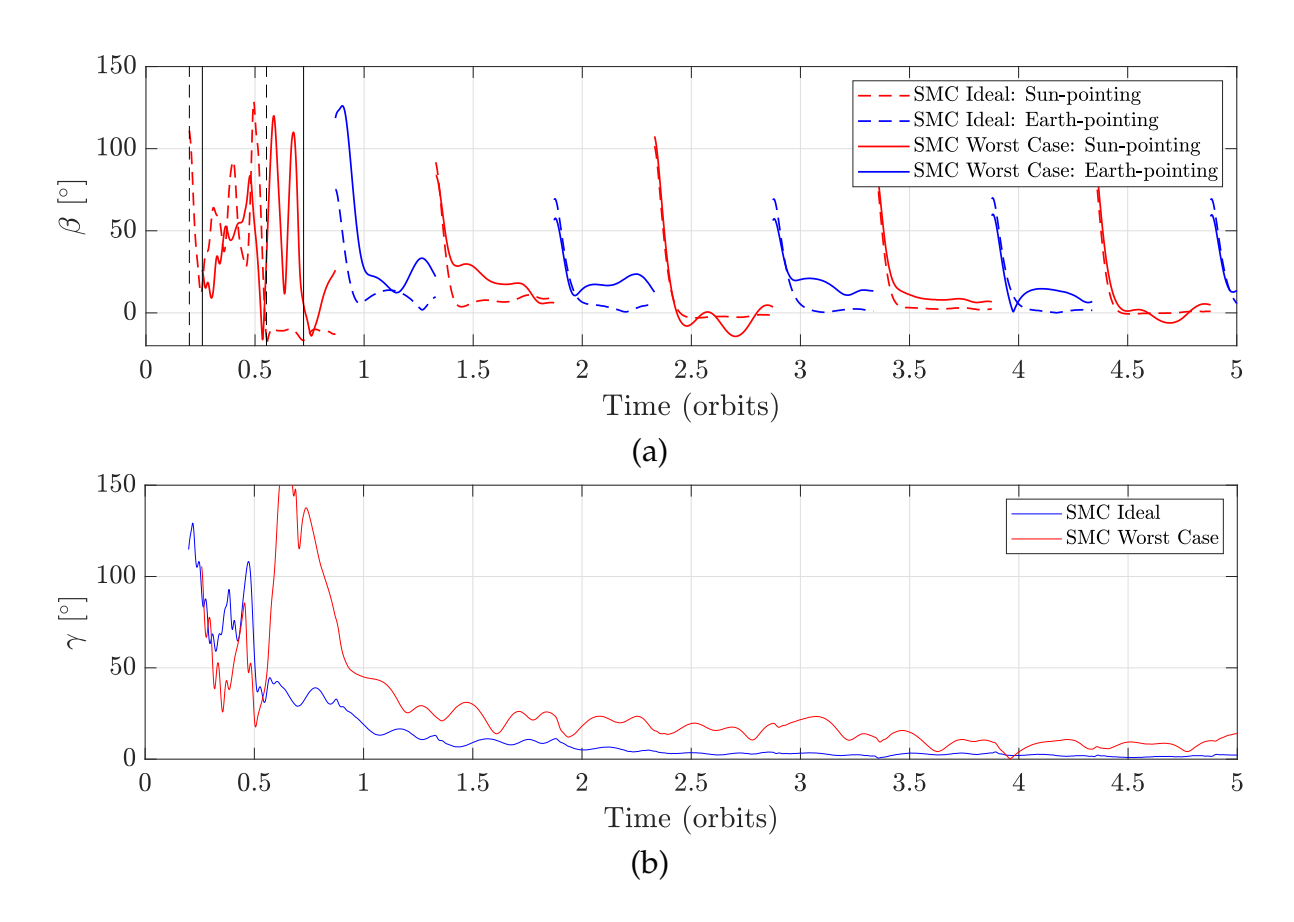


Figure 5.24: Pointing angles with sliding mode control, ideal vs worst case scenario. (a) \mathbf{z}_b - \mathbf{z}_d angle (b) \mathbf{y}_b - \mathbf{n}_o angle

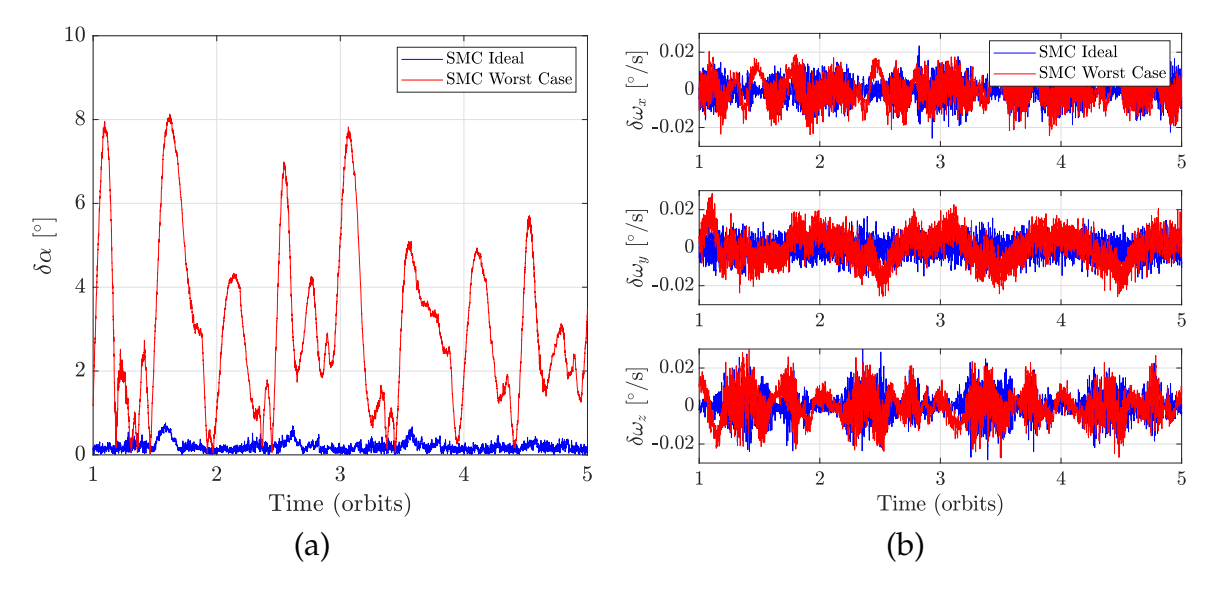


Figure 5.25: Estimate errors with sliding mode control, ideal vs worst case scenario. (a) Total angular error, (b) Angular velocity errors

Chapter 6

Conclusions

6.1 Summary of Research

This research focused on the development of an attitude determination and control system for the Meteorix mission, a cubesat mission dedicated to the autonomous detection of meteors and space debris entering the Earth's atmosphere. Accurate localization and tracking of meteors using an on-board camera and image processing chain requires high power consumption and is computationally expensive. This presented a constraint on the satellite: to use minimal sensors and actuators for attitude estimation and control. In particular, the ADCS hardware was constrained to a single magnetometer for attitude estimaton and three magnetic actuators for attitude control, with a single flywheel for gyroscopic stability. The mission was separated into three distinct modes of operation; detumbling mode, alignment mode, and nominal mode. Specific attitude estimation and control requirements were outlined for each mode based on the scientific objectives and power needs of the satellite, as well as the ADCS hardware constraints. The Meteorix satellite model and the ADCS were incorporated into D-SPOSE, a high fidelity orbit and attitude propagator.

Estimation of the attitude and angular velocity of Meteorix was accomplished with a magnetometer-only MEKF. Its formulation, as well as its performance, were compared to a traditional gyro-based MEKF that uses a gyroscope to measure angular velocity. The magnetometer-only MEKF relies on the measurements from the magnetometer and the satellite attitude dynamics model to estimate the attitude and angular velocity. The gyro-based MEKF estimates the attitude and gyroscope bias, and corrects the angular velocity measurements with the bias estimates. The performance of both algorithms was evaluated and compared through Monte Carlo simulations of two angular velocity scenarios with a wide range of initial estimate errors. Simulation results showed that the estimation accuracy of the magnetometer-only MEKF suffers in the high angular velocity scenario. However, in Chapter 5 the accuracy was shown to improve as active attitude control quickly detumbles the satellite. It was found that the gyro-based MEKF fails to converge in the low-angular velocity scenario, due to the poor noise characteristics of the gyro-scope. This highlighted the advantages of the magnetometer only MEKF as it met the attitude and angular velocity estimation requirements of Earth-pointing mode.

For attitude control of Meteorix, a nonlinear sliding mode controller was formulated and implemented to use full state feedback from the magnetometer-only MEKF. The sliding mode controller was compared to a simpler PD controller based on pure magnetic feedback. The performance was first evaluated in simulations of each operational mode. In simulations of detumbling mode, the two controllers were compared against the traditional B-dot control law commonly employed to detumble cubesats. The sliding mode controller outperformed both the B-dot and PD controllers, detumbling the satellite approximately 4 times faster. The siding mode controller was also superior to the PD controller in the alignment and nominal modes, showing faster alignment with the orbit normal and better Earth- and Sun-pointing accuracy.

A sensitivity study was conducted to investigate the overall ADCS performance in the presence of uncertainties and disturbances. The ADCS was tested against large initial estimate errors, inertia uncertainty, flywheel axis misalignment, and residual magnetic moment. The most significant effects on ADCS performance were flywheel misalignment and residual magnetic moment. In all cases, the sliding mode controller performed better than the PD controller, demonstrating its robustness. In the worst case scenario with all sources of error considered, the average Earth-pointing error with the PD controller was approximately 3 times larger than with the sliding mode controller, and did not meet the requirement of $\beta < 20^\circ$ imposed by the camera. The sliding mode controller was able to maintain an average Earth-pointing angle of $\beta \approx 11^\circ$, which is well within the requirement. The sliding mode controller also offered better alignment with the orbit normal and better Sun-pointing accuracy. However, the estimation accuracy of the magnetometer-only MEKF was significantly compromised in the worst case scenario, largely due to the flywheel axis misalignment and residual magnetic moment. Additional work is needed to improve the estimation accuracy.

6.2 Recommendations for Future Work

Many extensions can be made to the attitude estimation and control algorithms explored in this thesis to improve their performance and provide a more reliable ADCS for the Meteorix mission. First, attention should be given to the calibration of the satellite's sensors and actuators. In this work, it was assumed that the magnetometer was perfectly calibrated. However, it will have associated scale factors, misalignment terms, and biases in the signal that should be accounted for. This can be accomplished with online calibration methods. One such method was implemented in the EyeSat mission, in which an EKF was formulated to estimate the calibration matrix and bias terms of the magnetometer by comparing the norms of the magnetometer measurement and the IGRF magnetic field model. The estimates were fedback to the magnetometer measurement model and im-

proved the overall attitude estimation accuracy.

The magnetometer-only MEKF can be improved in a number of ways. First, it is recommended to estimate the residual magnetic moment as part of the MEKF state vector. The estimated residual magnetic moment can be included in the attitude dynamics model of the MEKF which would improve the overall attitude estimation accuracy. Furthermore, it can be fedback to the sliding mode controller and included as part of the equivalent control torque design. This would improve the overal robustness of the ADCS to residual magnetic moment. Improvements can also be made to account for uncertain parameters such as the satellite's inertia and the flywheel properties. There are many adaptive methods available in the literature to tackle these issues. It is also worth exploring other estimation and control techniques. A magnetometer-only unscented Kalman filter could be formulated and possibly provide better accuracy in the presence of uncertainties and disturbances. Optimal control formulations, such as LQR control, can also be implemented.

Further work can be done on simulation and validation. For example, the sensitivity study conducted in this work was limited and only considered one set of values for each source of error considered. Monte Carlo simulations that evaluate the ADCS performance over a range of sources of error could provide more conclusive results. Other sources of error, such as poor calibration of the magnetometer, or errors in the positional estimates from the GPS should be considered. A more rigorous power and energy analysis should also be conducted. It is crucial to verify that the proposed operational modes allow the satellite to generate enough power with the solar panels to sustain operation.

- [1] J. Puig-Suari, C. Turner, and R. J. Twiggs, "CubeSat: The Development and Launch Support Infrastructure for Eighteen Different Satellite Customers on One Launch," in *AIAA/USU Conference on Small Satellites*, 2001.
- [2] N. Rambaux, J. Vaubaillon, L. Lacassagne, D. Galayko, G. Guignan, M. Birlan, P. Boisse, M. Capderou, and N. Rambaux, "Meteorix: a cubesat mission dedicated to the detection of meteors and space debris," in 1st ESA NEO and Debris Detection Conference, ESA Space Safety Programme Office, 2019.
- [3] D. Koschny *et al.*, "Current activities at the ESA/ESTEC Meteor Research Group," in *International Meteor Conference Mistelbach*, Austria, p. 204, 2015.
- [4] R. Ishimaru, Y. Sakamoto, M. Kobayashi, S. Fujita, T. Gonai, and T. Matsui, "UV-Visible Observation of Meteors by CubeSat: S-CUBE Project," in *3rd International Workshop on Instrumentation for Planetary Mission*, vol. 1980, p. 4030, 2016.
- [5] T. Arai *et al.*, "On-Going Status of METEOR Project Onboard the International Space Station," in *49th Lunar and Planetary Science Conference*, 2018.
- [6] F. Colas et al., "FRIPON, the French fireball network," tech. rep., 2015.
- [7] H. Chen, N. Rambaux, and J. Vaubaillon, "Accuracy of meteor positioning from space- And ground-based observations," *Astronomy and Astrophysics*, vol. 642, p. 11, 2020.

[8] F. Apper, A. Ressouche, N. Humeau, M. Vuillemin, A. Gaboriaud, F. Viaud, and M. Couture, "Eye-Sat: A 3U Student CubeSat from CNES Packed with Technology," in 33rd AIAA/USU Conference on Small Satellites, 2019.

- [9] M. D. Shuster and S. D. Oh, "Three-axis attitude determination from vector observations," *Journal of Guidance, Control, and Dynamics*, vol. 4, no. 1, pp. 70–77, 1981.
- [10] F. L. Markley and J. L. Crassidis, Fundamentals of spacecraft attitude determination and control. Springer New York, 2014.
- [11] J. E. Keat, "Analysis of Least-Squares Attitude Determination Routine DOAO," 1977.
- [12] J. L. Crassidis, F. Landis Markley, and Y. Cheng, "Survey of nonlinear attitude estimation methods," *Journal of Guidance, Control, and Dynamics*, vol. 30, no. 1, pp. 12–28, 2007.
- [13] F. L. Markley, "Attitude error representations for Kalman filtering," *Journal of Guidance, Control, and Dynamics*, vol. 26, no. 2, pp. 311–317, 2003.
- [14] J. L. Crassidis and J. L. Junkins, Optimal Estimation of Dynamic Systems, Second Edition (Chapman & Hall/CRC Applied Mathematics & Nonlinear Science). Chapman & Hall/CRC, 2nd ed., 2011.
- [15] J. D. Searcy and H. J. Pernicka, "Magnetometer-only attitude determination using novel two-step kalman filter approach," *Journal of Guidance, Control, and Dynamics*, vol. 35, no. 6, pp. 1693–1701, 2012.
- [16] H. Yoon, K. M. Riesing, and K. Cahoy, "Kalman filtering for attitude and parameter estimation of nanosatellites without gyroscopes," *Journal of Guidance, Control, and Dynamics*, vol. 40, no. 9, pp. 2272–2288, 2017.
- [17] S. H. Mok, S. Y. Byeon, H. Bang, and Y. Choi, "Performance Comparison of Gyro-Based and Gyroless Attitude Estimation for CubeSats," *International Journal of Control, Automation and Systems*, vol. 18, no. 5, pp. 1150–1160, 2020.

[18] R. Burton, S. Rock, J. Springmann, and J. Cutler, "Online attitude determination of a passively magnetically stabilized spacecraft," *Acta Astronautica*, vol. 133, pp. 269–281, 2017.

- [19] P. Alken *et al.*, "International Geomagnetic Reference Field: the thirteenth generation," *Earth, Planets and Space*, vol. 73, no. 1, pp. 1–25, 2021.
- [20] G. Natanson, S. McLaughlin, and R. Nicklas, "A method of determining attitude from magnetometer data only," vol. -1, pp. 359–378, 1990.
- [21] M. Challa, G. Natanson, and N. Ottenstein, "Magnetometer-only attitude and rate estimates for spinning spacecraft," in *Astrodynamics Specialist Conference*, pp. 311–321, 2000.
- [22] M. L. Psiaki, F. Martel, and P. K. Pal, "Three-axis attitude determination via kalman filtering of magnetometer data," *Journal of Guidance, Control, and Dynamics*, vol. 13, no. 3, pp. 506–514, 1990.
- [23] G. F. Ma and X. Y. Jiang, "Unscented kalman filter for spacecraft attitude estimation and calibration using magnetometer measurements," in 2005 International Conference on Machine Learning and Cybernetics, ICMLC 2005, pp. 506–511, 2005.
- [24] P. Appel, "Attitude estimation from magnetometer and earth-albedo-corrected coarse sun sensor measurements," in *Acta Astronautica*, vol. 56, pp. 115–126, Pergamon, 2005.
- [25] H. Ma and S. Xu, "Magnetometer-only attitude and angular velocity filtering estimation for attitude changing spacecraft," *Acta Astronautica*, vol. 102, pp. 89–102, 2014.
- [26] M. Abdelrahman and S. Y. Park, "Simultaneous spacecraft attitude and orbit estimation using magnetic field vector measurements," *Aerospace Science and Technology*, vol. 15, no. 8, pp. 653–669, 2011.

[27] R. Wiśniewski and M. Blanke, "Fully magnetic attitude control for spacecraft subject to gravity gradient," *Automatica*, vol. 35, no. 7, pp. 1201–1214, 1999.

- [28] M. Lovera and A. Astolfi, "Global magnetic attitude control of inertially pointing spacecraft," *Journal of Guidance, Control, and Dynamics*, vol. 28, no. 5, pp. 1065–1067, 2005.
- [29] R. Wiśniewski, "Linear time-varying approach to satellite attitude control using only electromagnetic actuation," *Journal of Guidance, Control, and Dynamics*, vol. 23, no. 4, pp. 640–647, 2000.
- [30] A. C. Stickler and K. T. Alfriend, "Elementary magnetic attitude control system," *Journal of Spacecraft and Rockets*, vol. 13, no. 5, pp. 282–287, 1976.
- [31] M. Y. Ovchinnikov and D. S. Roldugin, "A survey on active magnetic attitude control algorithms for small satellites," 2019.
- [32] M. Shigehara, "Geomagnetic attitude control of an axisymmetric spinning satellite," *Journal of Spacecraft and Rockets*, vol. 9, no. 6, pp. 391–397, 1972.
- [33] K. Vega, D. Auslander, and D. Pankow, "Design and Modeling of an Active Attitude Control System for CubeSat Class Satellites," in *AIAA Modeling and Simulation Technologies Conference*, (Reston, Virigina), American Institute of Aeronautics and Astronautics, 2009.
- [34] F. Viaud and O. Lagrange, "Safe Mode Attitude Control of EyeSat Mission," in *EuroGNC*, (Warsaw, Poland), 2017.
- [35] M. Guelman, R. Waller, A. Shiryaev, and M. Psiaki, "Design and testing of magnetic controllers for Satellite stabilization," in *Acta Astronautica*, vol. 56, pp. 231–239, Pergamon, 2005.
- [36] F. Viaud, B. Charbaut, F. Apper, N. Humeau, and A. Ressouche, "Flight Dynamics for the Astronomy Mission EyeSat," in 4S Symposium, (Serrento, Italy), CNES, 2018.

[37] L. Sagnières, N. Rambaux, T. Vailant, Sharf, Inna, and F. Viaud, "Attitude control strategy for an Earth-observing CubeSat with high power consumption," Unpublished Manuscript, 2019.

- [38] S. Lagrasta and M. Bordin, "Normal mode magnetic control of LEO spacecrafts, with integral action," in 1996 Guidance, Navigation, and Control Conference and Exhibit, pp. 1–9, American Institute of Aeronautics and Astronautics Inc, AIAA, 1996.
- [39] E. Silani and M. Lovera, "Magnetic spacecraft attitude control: A survey and some new results," *Control Engineering Practice*, vol. 13, no. 3, pp. 357–371, 2005.
- [40] M. Lovera, "Periodic Attitude Control for Satellites with Magnetic Actuators: An Overview," *IFAC Proceedings Volumes*, vol. 34, no. 12, pp. 113–118, 2001.
- [41] R. Wiśniewski, "Sliding Mode Attitude Control for Magnetic Actuated Satellite," *IFAC Proceedings Volumes*, vol. 31, no. 21, pp. 179–184, 1998.
- [42] A. Sofyali and E. M. Jafarov, "Purely magnetic spacecraft attitude control by using classical and modified sliding mode algorithms," in *Proceedings of IEEE International Workshop on Variable Structure Systems*, pp. 117–123, 2012.
- [43] A. Sofyali and E. M. Jafarov, "Integral sliding mode control of small satellite attitude motion by purely magnetic actuation," in *IFAC Proceedings Volumes (IFAC-PapersOnline)*, vol. 19, pp. 7947–7953, IFAC Secretariat, 2014.
- [44] A. Sofyalı, E. M. Jafarov, and R. Wisniewski, "Robust and global attitude stabilization of magnetically actuated spacecraft through sliding mode," *Aerospace Science and Technology*, vol. 76, pp. 91–104, 2018.
- [45] K. Zhou, H. Huang, X. Wang, and L. Sun, "Magnetic attitude control for Earthpointing satellites in the presence of gravity gradient," *Aerospace Science and Technology*, vol. 60, pp. 115–123, 2017.

[46] J. Li, M. Post, T. Wright, and R. Lee, "Design of Attitude Control Systems for CubeSat-Class Nanosatellite," *Journal of Control Science and Engineering*, vol. 2013, p. 657182, 2013.

- [47] M. Abdelrahman and S. Y. Park, "Integrated attitude determination and control system via magnetic measurements and actuation," *Acta Astronautica*, vol. 69, no. 3-4, pp. 168–185, 2011.
- [48] N. Sugimura, T. Kuwahara, and K. Yoshida, "Attitude determination and control system for nadir pointing using magnetorquer and magnetometer," in *IEEE Aerospace Conference Proceedings*, vol. 2016-June, IEEE Computer Society, 2016.
- [49] R. H. Soja, M. Sommer, J. Herzog, R. Srama, E. Grün, J. Rodmann, P. Strub, J. Vaubaillon, A. Hornig, and L. Bausch, "The Interplanetary Meteoroid Environment for eXploration (IMEX) project," in *Proceedings of the International Meteor Conference, Giron, France*, 18-21 September 2014, pp. 146–149, 2014.
- [50] ISISPACE, Magnetorquer Board (iMTQ), 2013. Available at https://www.isispace.nl/wp-content/uploads/2016/02/iMTQ-Brochure-v1.pdf.
- [51] Azur Space Solar Power GmbH, 30% Triple Junction GaAs Solar Cell Assembly, 2016. Available at http://www.azurspace.com/images/products/0003401-01-01_DB_3G30A.pdf.
- [52] G. Kopp and J. L. Lean, "A new, lower value of total solar irradiance: Evidence and climate significance," *Geophysical Research Letters*, vol. 38, no. 1, 2011.
- [53] L. B. M Sagnières and I. Sharf, *Modeling and Simulation of Long-term Rotational Dynamics of Large Space Debris*. PhD thesis, McGill University, 2019.
- [54] J. R. Dormand and P. J. Prince, "A family of embedded Runge-Kutta formulae," *Journal of Computational and Applied Mathematics*, vol. 6, no. 1, pp. 19–26, 1980.

[55] Hyperion Technologies, RW210 Series Reaction Wheel, 2018. Available at https://hyperiontechnologies.nl/wp-content/uploads/2018/07/ HT-RW210_V1.02_Flyer.pdf.

- [56] IAGA, "International Geomagnetic Reference Field," 2019.
- [57] IMCCE, "Mirade The Virtual Observatory Solar System Object Ephemeris Generator," 2018.
- [58] J. M. Picone, A. E. Hedin, D. P. Drob, and A. C. Aikin, "NRLMSISE-00 empirical model of the atmosphere: Statistical comparisons and scientific issues," *Journal of Geophysical Research: Space Physics*, vol. 107, no. A12, p. 1468, 2002.
- [59] N. K. Pavlis, S. A. Holmes, S. C. Kenyon, and J. K. Factor, "The development and evaluation of the Earth Gravitational Model 2008 (EGM2008)," *Journal of Geophysical Research: Solid Earth*, vol. 117, no. 4, p. 4406, 2012.
- [60] O. Montenbruck and E. Gill, Satellite Orbits. Springer Berlin Heidelberg, 2000.
- [61] Honeywell, 3-Axis Digital Compass IC HMC5883L, 2013. Available at https://cdn-shop.adafruit.com/datasheets/HMC5883L_3-Axis_ Digital_Compass_IC.pdf.
- [62] Analog Devices, Triaxial Intertial Sensor with Magnetometer ADIS16405, 2019. Available at https://www.analog.com/media/en/technical-documentation/data-sheets/ADIS16405.pdf.
- [63] J. Armstrong, C. Casey, G. Creamer, and G. Dutchover, "Pointing Control for Low Altitude Triple Cubesat Space Darts," *Small Satellite Conference*, 2009.